RUNOFF GENERATION MECHANISMS IN A STEEP FIRST-ORDER BRITISH COLUMBIAN WATERSHED

by

Daniel R W Haught
Bachelor of Science, Western Washington University, 2006

THESIS SUBMITTED IN PARTIAL FULFILLMENT OF
THE REQUIREMENTS FOR THE DEGREE OF

MASTER OF SCIENCE

In the Department of Geography
Simon Fraser University (Faculty of the Environment)

SIMON FRASER UNIVERSITY

Spring 2010

APPROVAL

Name: Daniel R W Haught

Degree: Masters of Science

Title of Thesis: Runoff generation mechanisms in a steep first-order British Columbian watershed.

Examining Committee:

Chair: **Dr. Eugene McCann**
Associate Professor
Department of Geography
Simon Fraser University

Dr. Ilja Tromp-van Meerveld
Senior Supervisor
Assistant Professor
Department of Geography
Simon Fraser University

Dr. Jeremy Venditti
Supervisor
Assistant Professor
Department of Geography
Simon Fraser University

Dr. Diana Allen
External Examiner
Professor
Department of Earth Sciences
Simon Fraser University

Date Defended/Approved: April 23, 2010

Declaration of
Partial Copyright Licence

ABSTRACT

This research was undertaken in the Malcolm Knapp Research Forest in British Columbia Canada and aimed to examine runoff generation mechanisms in a steep forested watershed. The research questions were: (1) can water infiltrate into the bedrock in the study watershed, (2) can bedrock infiltration be described with simple infiltration models that have been developed for soil infiltration, and (3) what is the spatial variation in the relations between discharge and piezometric response on the hillslope? To answer these questions hydrometric data from a 20 m by 18 m hillslope and from bedrock infiltration ponds were collected. The results from this research showed that the bedrock is permeable and that soil infiltration models can represent bedrock infiltration. The hillslope has two distinct water table zones; a hillslope zone and riparian zone. The riparian zone is located 0-8 m from the stream while the hillslope zone is 8-18 m uphill.

Keywords: Hillsope Hydrology, Bedrock Infiltration, Subsurface Stormflow, Runoff Generation Mechanisms, Infiltration Pond, British Columbia Coastal Mountains, Malcolm Knapp Research Forest

DEDICATION

This is dedicated to:

My sister, Colleen Elizabeth Whealdon-Haught. May she rest in peace. She is missed and will always be remembered.

My family, who have unconditionally loved and supported me through this process and throughout life.

My friends, who have provided support and friendship that was invaluable.

ACKNOWLEDGEMENTS

I would like to thank,

- Dr. Ilja Tromp-van Meerveld for her patience, encouragement, and help throughout this process. Along with many more things she has done.
- Dr. Jeremy Venditti for his time, patience, and input.
- Dr. Diana Allen for her time and critique of my thesis.
- Everyone in the research group who have both contributed time and energy in both the field and lab, along with thoughtful ideas, critique, and stress relieving conversation.
- Friends and family who have been there to listen (sometimes I imagine unbearably) to me when I needed to vent, for the needed evenings out, for the occasional beer (or R&D), and for thoughts and friendships.
- This work was supported by NSERC-Discovery Grant 342447-07.

TABLE OF CONTENTS

Approval ii
Abstract iii
Dedication iv
Acknowledgements v
Table of Contents vi
List of Figures viii
List of Tables xii

1: INTRODUCTION 1

2: SITE DESCRIPTION 7

3: INFILTRATION AND RECHARGE INTO FRACTURED BEDROCK 14
3.1 Introduction 14
3.2 Methods 18
3.2.1 Field experiments 18
3.2.2 Rock core experiments 20
3.2.3 Models 22
3.3 Results 24
3.3.1 Observed cumulative infiltration rates 24
3.3.2 Fitted cumulative infiltration models 26
3.3.3 Estimated hydraulic properties of the bedrock 28
3.3.4 Parameter uncertainty 29
3.3.5 Falling head core tests and water retention curves 30
3.4 Discussion 30
3.4.1 Comparison to soil infiltration 30
3.4.2 Abnormalities in infiltration patterns 32
3.4.3 Differences between the infiltration ponds/effects of scale 36
3.4.4 Hydraulic conductivity of the bedrock 37
3.4.5 Influence of bedrock infiltration on subsurface storm flow and the water balance 38
3.5 Conclusion 40
3.6 Figures 43
3.7 Tables 62

4: SPATIAL VARIATION IN WATER TABLE FLUCTUATIONS ACROSS A HILLSLOPE 66
4.1 Introduction 66
4.2 Methods and analysis 70
4.2.1 Methods 70
4.2.2 Analyses 73

4.3 Results and interpretation 75
4.3.1 Spatial variation in water table presence and response 75
4.3.2 Seasonal variation in the relation between water level and discharge 79
4.3.3 Lag analysis and optimization 80
4.3.4 Timing of water table response to rainfall 81
4.4 Discussion 83
4.4.1 Spatial variation in lag times of groundwater response 83
4.4.2 Distinction between water table dynamics in the riparian and hillslope zones 85
4.4.3 Hydrologically limited response in water table dynamics 87
4.4.4 Implications for runoff generation mechanisms at the hillslope scale 89
4.5 Conclusion 92
4.6 Figures 95
4.7 Tables 108

5: GENERAL CONCLUSION 110
5.1 Overview 110
5.2 Discussion 111
5.3 Future work 115
5.4 Conclusions 116

REFERENCE LIST 117

APPENDICES 123
Appendix 1: Bedrock and watershed characteristics 123
Appendix 2: Matlab© files 127
Appendix 3. Tracer experiment 139

LIST OF FIGURES

Figure 2.1. Location of Malcolm Knapp Research Forest (49°17.844' N and 122°33.582'). 10

Figure 2.2. Map of the research watershed and hillslope. 11

Figure 2.3. Surface elevation (top), topographic wetness index (middle), and slope (bottom) for the study hillslope. Locations identified by circles and labelled with a letter followed by a number (i.e. A1) represent locations of piezometers used in the study (see chapter 4). The elevation is relative to an arbitrary datum. Slope units are ratio (rise/run). 12

Figure 2.4. Photo of fractured bedrock along the logging road's cut-bank shown in Figure 2.2. 13

Figure 3.1. Photo of pond 1 (middle) and pond 2 (right), along with the reservoir (left). The fracture that runs under pond 2 is identified by the line with four small trees in the forefront of the reservoir and pond 1. 43

Figure 3.2. Photo of pond 3 prior to inundation. 44

Figure 3.3. Schematic of the infiltration ponds used in this research. For information on the specific widths, lengths, heights, and head levels see table 3.1. 44

Figure 3.4. Observed cumulative infiltration for ponds 1, 1(2), 2 and 3 for 800 hours. 45

Figure 3.5. Observed cumulative infiltration for ponds 1, 1(2), 2, and 3 for the first 96 hours of the experiments. 46

Figure 3.6. Observation and fitted cumulative infiltration for ponds 1, 1(2), 2, and 3. 47

Figure 3.7. Relationship between observed and modeled cumulative infiltration for the Horton, Philip, and Green and Ampt models for both ponds 1, 1(2), 2 and 3. 48

Figure 3.8. Dotty plots of the sensitivity of the Horton model for Pond 3 when using the correlation coefficient. The top graph describes the results for the initial infiltration parameter (f_o) while the middle graph shows the final infiltration or hydraulic conductivity (f_c) and the bottom graph shows the fitting parameter (k). The red star represents the maximum value. The solid blue dots represent the best 0.1% of the Monte-Carlo simulations and represent the acceptable range. These ranges can also be found in Table 3.4. 49

Figure 3.9. Dotty plots of the sensitivity of the Horton model for ponds a) 1, b) 1(2), c) 2, and d) 3 when using the MSE (except pond 3 which uses MAE because of its better evaluation). The top graph describes the initial infiltration parameter (f_o) while the middle graph describes the final infiltration or hydraulic conductivity (f_c) and the bottom graph describes the fitting parameter (k). The red star represents the minimum value. The solid blue dots represent the best 0.1% of the Monte-Carlo simulations and represent the acceptable range. These ranges can also be found in Table 3.4. 50

Figure 3.10. Dotty plots of the sensitivity of the Philip model for ponds a) 1, b) 1(2), c) 2, and d) 3 when using the MSE criteria (except pond 3 which uses MAE). The upper graph shows the results for the sorptivity parameter (S) while the bottom graph shows the hydraulic conductivity (K). The red star represents the minimum value (i.e. optimized). The solid blue dots represent the best 0.1% of the Monte-Carlo simulations and represent the acceptable range. These ranges can also be found in Table 3.4. 54

Figure 3.11. The optimized hydraulic conductivities and the respective uncertainty ranges (as determined by the Monte-Carlo analyses) for all experiments as a function of scale (area). The triangles, circles, and squares represent the Horton, Philip, and Green and Ampt model results, respectively. 58

Figure 3.12. Photo of rock core T1. This figure shows preferential flow through fractures. Blue dye was introduced a week after the start of the falling head infiltration test. The clear water droplet shows that water is moving through the rock at different rates. Black arrows show locations of blue water drops and the white arrow shows the location of a clear water drop. 59

Figure 3.13. Hydraulic conductivity as a function of depth below the surface. Values from ponds 1, 1(2), 2, and 3 are the values determined by optimization for the different models. 60

Figure 3.14. Relationship between total precipitation and storm runoff for events occurring between 10/2008 to 10/2009. Storm events were determined by periods of rainfall that lasted longer than 2 hours and were separated by breaks longer than 6 hours. Discharge totals for the related storms were calculated by subtracting the baseflow (using the slope method) prior to the event from the event response until it reached the new baseflow. Runoff was determined by finding the contributing area of the research watershed (17 ha; which can be found in appendix 2). Inset shows the runoff ratio for the same storms as a function of the total precipitation. 61

Figure 4.1. Hyeotograph and hydrograph for the study period. Discharge values above 50 l/s are uncertain due to the lack of discharge measurements above 50 l/s. The arrow denotes the area of missing rainfall data from the MKRF gauge. The arrows with vertical lines indicate periods when the rain gauge was frozen. 95

Figure 4.2. Fraction of time a measurable water table (>0.07m) was present during the period of 10/20/08 to 10/20/09 as a function of distance uphill. 96

Figure 4.3. Dendrogram of the hierarchical cluster analysis based on the average, standard deviation, and range of the water table above bedrock, and percent of time with water table presence. 97

Figure 4.4. Correlations between piezometers. The number in the top of each graph represents the Spearman rank correlation coefficient. For the location of the piezometers see Figure 2.3 in chapter 2. 98

Figure 4.5. Relation between the Spearman rank correlation coefficient for the relation between discharge and water table response and distance uphill for the whole study period (10/20/2008 to 10/20/2009). Outer bars represent the histogram of the distribution of points. Note the outlier (site A1) and the decline in correlation for points located more than 8 meters uphill (denoted by dashed line). 99

Figure 4.6. Relationship between piezometer groundwater level and discharge for fall 2008 (September-November). Location of the subfigures relates to the location of the piezometers on the hillslope (Figure 2.3, chapter 2). Piezometers on rows A and B represent the riparian zone. Piezometer depth (below the soil surface) and distance uphill are given in Table 4.1 100

Figure 4.7. Pearson r^2 values of the logarithmic relationship between groundwater and discharge ($z= a*\ln(Q)+b$) as a function of distance uphill. Black squares represent the fall season while open circles represent the summer season. 101

Figure 4.8. Seasonal variation in the relationship between groundwater level and discharge for piezometer A3 (bottom), B3 (middle), C3 (top). This figure shows that the relations are strongest for the fall and spring and become weaker as distance uphill increases. Increased scatter in winter is partially attributed to snow cover and differential melt rates. 102

Figure 4.9. Spearman rank correlation coefficient for the relationship between streamflow and water level for the different seasons as a function of upslope distance. 103

Figure 4.10. Histograms of the Spearman rank correlation coefficient between streamflow and groundwater level for the different seasons. 104

Figure 4.11. Relationship between the lag time between peak water level and peak discharge for specific storms in the fall/winter/spring of 2008/09. Positive lag times indicate that the stream responds before the water table responded 105

Figure 4.12. Relationship between the lag time between the start of piezometer response and the start of discharge response and distance uphill for specific storms in the fall/winter/spring of 2008/09 105

Figure 4.13. Lag optimized Spearman rank correlation coefficient between streamflow and groundwater response as a function of distance uphill for the fall of 2008. The size of the point represents the optimal

lag time. Black circles represent negative lag times (water table responds before the discharge). White circles represent positive lag times (water tables that respond after discharge). Ranges of lag times are -2.5 to 22 hours with optimized negative lag times between -2.5 hours to -20 minutes and positive lag between 1 and 22 hours..... 106

Figure 4.14. Water table, soil moisture, and streamflow response for storms occurring on: 11/7/2008 (top left), 12/09/2008 (top right), 3/01/2009 (bottom left), and 5/11/2009 (bottom right). The number in the top left of each graph represents the total precipitation for the storms. 107

Figure 5.1. Conceptual model of the reseach hillslope. P, M and F denote preferential, matrix and fractured flow paths, respectively. Differences in arrow size are intended to distinguish flow proportion within each compartment. 114

LIST OF TABLES

Table 3.1. Area, ponding depths, height, width, and length for all three ponds. 62

Table 3.2. Values of the mean squared error (MSE), and mean absolute error (MAE), correlation coefficient (r) for ponds 1, 1(2), 2, and 3. The models were fit by minimizing sum of squared error between the model and observed values. 62

Table 3.3. Hydraulic properties for the best-fit Horton, Philip, and Green and Ampt models. 63

Table 3.4. List of ranges for the parameters for the Horton and Philip models for the different goodness of fit criteria as found with the uncertainty analysis for pond 1 and pond 1(2). Units for f_c, f_o, and K are m/s. Units for S are (m/s)^0.5. Units for k is hour. Ranges represent the top 0.1% of the results from the 250,000 Monte-Carlo analysis. 64

Table 3.5. Hydraulic conductivities for other studies that examined bedrock conductivity. 65

Table 3.6. Potential bedrock infiltration based on the hydraulic conductivities for all four pond experiments. Results are based on average water table presence for three piezometers within the research hillslope. The piezometers were located at the middle and bottom of the hillslope. Values in parentheses are from rages given in Table 3.4. 65

Table 4.1. Characteristics of the piezometers on the research hillslope. For the location of the piezometers see Figure 2.3 in chapter 2. 108

Table 4.2. Correlations between hillslope parameters. 109

1: INTRODUCTION

When rainwater infiltrates into forest soil, both lateral and vertical flow occurs. In a catchment with relatively shallow soils (<10m), as is the case in most steep forested areas, the ratio of vertical flow to lateral flow partially determines the transit time of subsurface storm flow (Asano et al. 2002; Uchida et al. 2002; 2006). The vertical flow is termed infiltration as it enters the soil and percolation as it flows through the soil. As the vertical flow of water passes through the unsaturated zone or vadose zone it can either bypass the soil matrix through macropores (decayed roots, fractures, animal burrows) or it can travel through the matrix. The flow of water through the matrix is controlled by the hydraulic conductivity and pore pressure gradients. Vertical flow tends to cease when either a true water table or a lower permeability layer is reached. Lateral flow is the process that usually moves water out of the hillslope towards the stream. In steep slopes, it is the large difference in gravitational potential rather than the smaller difference in matric potential that drives lateral flow. Detailed analysis of flow directions in relatively deep soils by Harr (1977) showed that "between storms, the vertical component of flux at the 10-cm depth was much less than the downslope component but equalled the downslope component during storms. Conversely, vertical components of flux at 70- and 30-cm depths were much less than downslope components during storms but equalled downslope components between storms".

In soils with distinctively different hydraulic conductivities between soil horizons, the decrease in permeability at the lower boundary between soil horizons can cause lateral throughflow. Soil-bedrock interface flow (subsurface stormflow) occurs when the lower boundary is the bedrock. When the lower boundary is impermeable, the percolation of rainwater ceases and water ponds at this boundary. Additional precipitation leads to a rise in the elevation of the transient saturated zone into the shallower, more permeable soil layers, and thus increased lateral flow rates. Lateral flow along the soil-bedrock interface has been found to be the dominant runoff process in steep, shallow soils, in humid environments (Weyman 1973; Mosley 1979; Peters et al. 1995; Weiler et al. 2005).

In steep watersheds, with shallow soils, two saturated zones exist. One saturated zone is a true water table (located in deep bedrock) and the second is a transient perched water table located at the soil-bedrock interface when a substantial decrease in hydraulic conductivity exists. In the remainder of this thesis, the term water table will refer to the perched water table while the term deep groundwater table will refer to the true water table in the bedrock.

As the water table rises from the impermeable layer towards the soil surface, the hydraulic conductivity increases and throughflow is transmitted faster. More importantly, lateral macropores become saturated and lateral macropore flow occurs. The soil porosity, moisture content, and lateral hydraulic conductivity are of critical importance for throughflow. When the impermeable or lower permeability layer is relatively deep, and the soil has a high drainable porosity,

antecedent moisture content and storm size significantly influence lateral flow quantity and timing (Uchida et al. 2002; Redding and Devito 2008).

Flow along the soil-bedrock interface is controlled by the bedrock topography (McDonnell et al. 1996; Peters et al. 1995; Woods and Rowe 1996; Freer et al. 1997; 2002; Tromp-van Meerveld and McDonnell 2006). As water travels laterally along the soil-bedrock interface it becomes constrained by (micro)topography. As water levels rise above the constraining barriers, saturated areas connect and widespread subsurface flow occurs (Tromp-van Meerveld and McDonnell 2006). These barriers also act to direct the flow down the hillslope to spatially distinct concentrated areas. These are usually the hollows in the bedrock (McDonnell et al. 1996). This illustrates the importance of the bedrock (micro)topography in determining the spatial distribution of subsurface stormflow.

Preferential lateral flow is threshold dependent (Weiler and McDonnell 2007). The concept of threshold dependency is that as the water table rises, the transmissivity increases, thereby increasing lateral flow. Matrix flow and pipe flow or macropore flow increase with increased soil saturation. Macropore and pipe flow only occur when the pipe is below the water table (McDonnell 1990). These preferential flow paths control the timing of the flow of water (and solutes) during rainfall events. This influences the biogeochemistry (leaching) and the timing and volume of peak flow.

In catchments in southwest British Columbia, preferential flow has been found to be important (Hutchison and Moore 2000). Cheng (2007) conducted a laboratory experiment to examine tracer breakthrough in a large soil core from

the study site of this research and found that preferential flow significantly influenced vertical flow through the soil core. Preferential flow occurred predominantly along roots. Matrix flow also existed and it was suggested that a pressure wave mechanism, as described by Torres et al. (1998), has an impact on vertical flow during rapid changes in rainfall intensity as well. Because preferential flow occurred mainly along roots, it is suspected that lateral preferential flow paths also exist.

A common boundary condition in rainfall-runoff models is that the underlying (i.e. bedrock, till) boundary is impermeable. However, in permeable bedrock conditions, ponding may or may not occur and in permeable conditions, the resulting water infiltration in the bedrock should be considered an important factor in runoff processes and the water balance. Tromp-van Meerveld et al. (2007) found that in the Panola Mountain Research Watershed (near Atlanta, GA USA) lateral flow along the soil-bedrock interface infiltrated the bedrock due to the high permeability of the bedrock. In Fudoji, Japan, precipitation was found to infiltrate the bedrock in upslope areas and move through the hillslope, bypassing the normal mixing processes in the soil. The bedrock water acted as a significant contributor to stormflow and transient groundwater formation (Uchida et al. 2002). Anderson et al. (1997) found that bedrock in Coos Bay, Oregon was permeable and contributed to both the persistence in baseflow and development of stormflow. Bedrock throughflow reduces subsurface stormflow through the soil matrix and increases the transit time (Uchida et al. 2002). As the bedrock transmits water to deeper storage, there is generally less lateral stormflow. The

decrease in stormflow changes the partitioning of baseflow/stormflow and requires larger storms to produce subsurface stormflow. Bedrock flow generally results in higher and more persistent baseflow as well. These findings illustrate the importance of flow through bedrock on runoff and runoff generation mechanisms.

This research will look at the bedrock boundary and its influence on hillslope hydrological pathways in forested watersheds. The objective of this research wass to gain a better understanding of runoff generation mechanisms in steep, forested hillslope in the coast mountains of British Columbia. My main research questions were:

1. Can water infiltrate into the bedrock in the Malcolm Knapp Research Forest study watershed?
2. Can bedrock infiltration be described with simple infiltration models (i.e. the Horton, Philip, and Green and Ampt models) that have been developed for soil infiltration?
3. What is the spatial variation in the relations between discharge and piezometric response on the hillslope?

The hypotheses were:

1. Water can infiltrate into bedrock, even though the bedrock has a much lower hydraulic conductivity than the overlying soil.
2. Common infiltration models cannot accurately describe bedrock infiltration.
3. The relation between discharge and piezometric response is different for the riparian and hillslope areas.

Questions 1 and 2 will be addressed in chapter 3, while question 3 will be addressed in chapter 4. Chapter 2 describes the study site while chapter 5 gives

an overall conclusion and recommendations for future research. Appendix 3 describes a tracer experiment that examines the spatial and temporal variation of water fluxes within a hillslope. This work was intended to illuminate the influences of bedrock microtopography on flow paths and to identify more portions of the hillslopes water balance.

2: SITE DESCRIPTION

The research site is located at 49°17.844' N and 122°33.582' W near the middle of the University of British Columbia Malcolm Knapp Research Forest (MKRF), about 45 km east of Vancouver, BC, Canada (Figure 2.1). The research watershed and hillslope site are approximately 0.9 ha and 400 m^2, respectively (Figure 2). The watershed and hillslope sites have average slopes of approximately 20-30% and 53% (Figure 2.2 and 2.3), with predominantly southern and southeastern aspects, respectively. The watershed consists of a combination of hollows and spurs along a perennial first-order stream and is located approximately 400 m above mean sea level.

The climate is of maritime influence with an average daily temperature of 15°C during summer months and 0°C during the winter months. Annual rainfall ranges from 2000 to 3000 mm. Less than 15% of the precipitation falls as snow (Utting 1979). Total precipitation during the 10/21/2008 to 10/21/2009 study period was 1493 mm (http://www.mkrf.forestry.ubc.ca/research/weather.htm). The total amount of snow (snow depth) was 104 cm.

The research site has a thin or absent soil mantle (0-2 m). The soils within the MKRF and the research watershed are humic-ferric podzols and are sandy loam in texture. The soil profile consists of O-Ae-B horizons. The O horizon represents the first 5 cm, the A horizon is thin ranging from 1 to 3 cm, and the B horizon varies in depth until it reaches either the underlying bedrock or glacial till (Bryck

1975; one field sample). The patches of glacial till are rare within the MKRF (Utting 1979) and were not observed in the study watershed. The soils also contain large amounts of buried small to large woody debris. Two 1 m deep soil pits in the MKRF showed the soil is a Gleyic Dystric Brunisol (Tashe 1998). These soils originated from a morainal parent material (Klinka 1976). The geology of the MKRF belongs to the Coast Crystalline complex and consists mainly of Cretaceous quartz diorite and granodiorite. Bedrock outcrops are common within the watershed.

The vegetation is dominated by western hemlock (*Tsuga heterophylla*) and western red cedar (*Thuja plicata*). The undergrowth consists of salal (*Gaultheria shallon*), red huckleberry (*Vaccinium parvifolium*), and sword fern (*Polystichum munitum*). There is a recent (3 years old) clear-cut north of the study watershed. The clear-cut is separated from the research watershed by an old logging road. The road cuts show both significant fractures and tree roots at and into the soil-bedrock interface (Figure 2.4). Blasting of the road cuts may have caused some of the fracturing. The presence of roots, however, suggests that at least some of the fractures were already present before blasting began.

The three infiltration ponds that are the focus of chapter 3 are located at the northern boundary (pond 3) and middle of the research watershed (pond 1 and 2) (Figure 2.2). Ponds 1 and 2 are located close to one another. The research hillslope that is the focus of chapter 4 is located in the middle of the study watershed (Figure 2.2). The hillslope was surveyed at a one metre resolution to determine the surface topography. Topography is shown in Figure 2.3 (top) as

contours that were obtained by spatial interpretation using Kriging. Note the change in slope (step) at approximately 8-9 m from the stream in Figure 2.3 (bottom). The topographic wetness index (Beven and Kirkby 1979) was used to determine the areas of highest likelihood of saturation.

$$WI = ln\frac{\mathrm{a}}{\tan(\beta)} \qquad (2.1)$$

Where (a) is the contributing area (L^2) and (β) is the slope (°).

The topographic wetness index shows that the areas that are likely to be wet are located in the middle and bottom of the hillslope (Figure 2.3, middle).

Figure 2.1. Location of Malcolm Knapp Research Forest (49°17.844' N and 122°33.582').

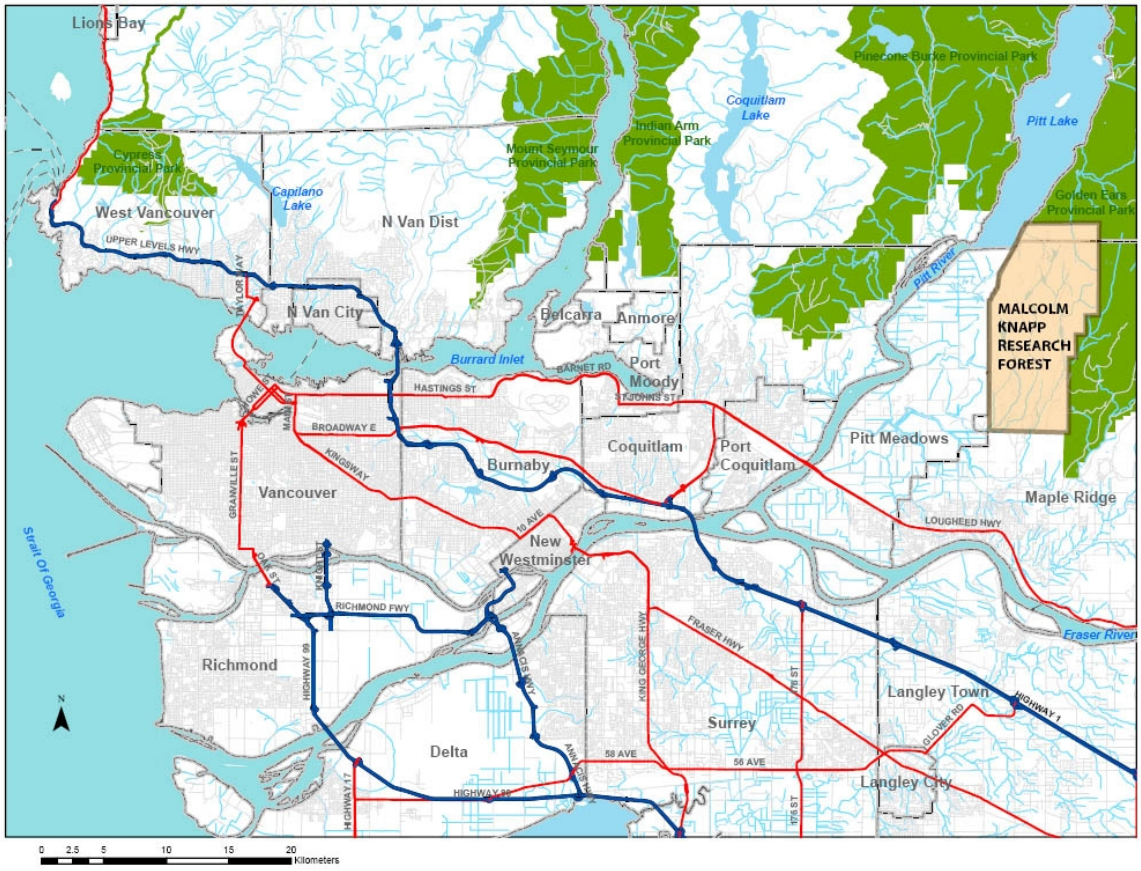

Figure 2.2. Map of the research watershed and hillslope.

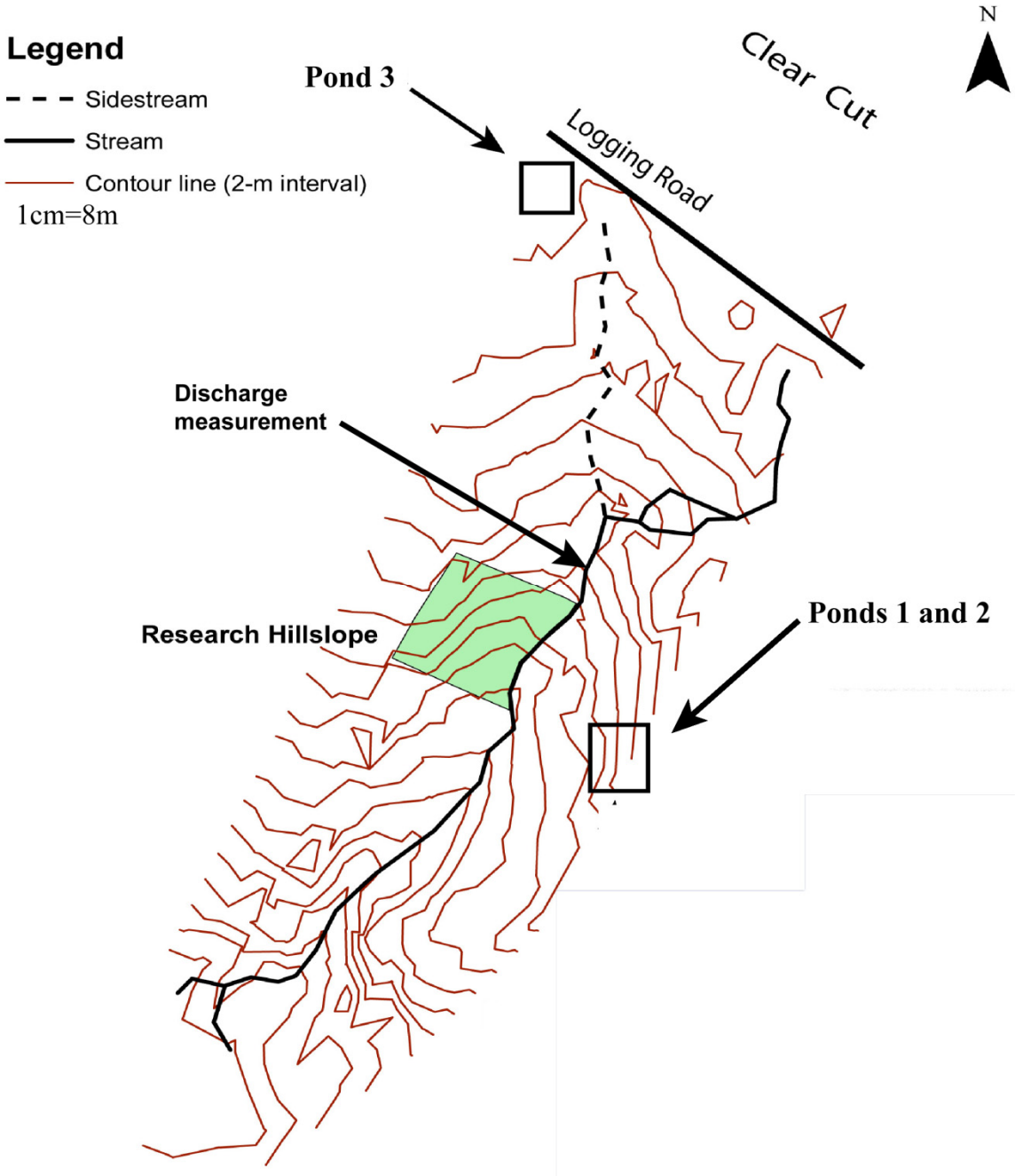

Figure 2.3. **Surface elevation (top), topographic wetness index (middle), and slope (bottom) for the study hillslope. Locations identified by circles and labelled with a letter followed by a number (i.e. A1) represent locations of piezometers used in the study (see chapter 4). The elevation is relative to an arbitrary datum. Slope units are ratio (rise/run).**

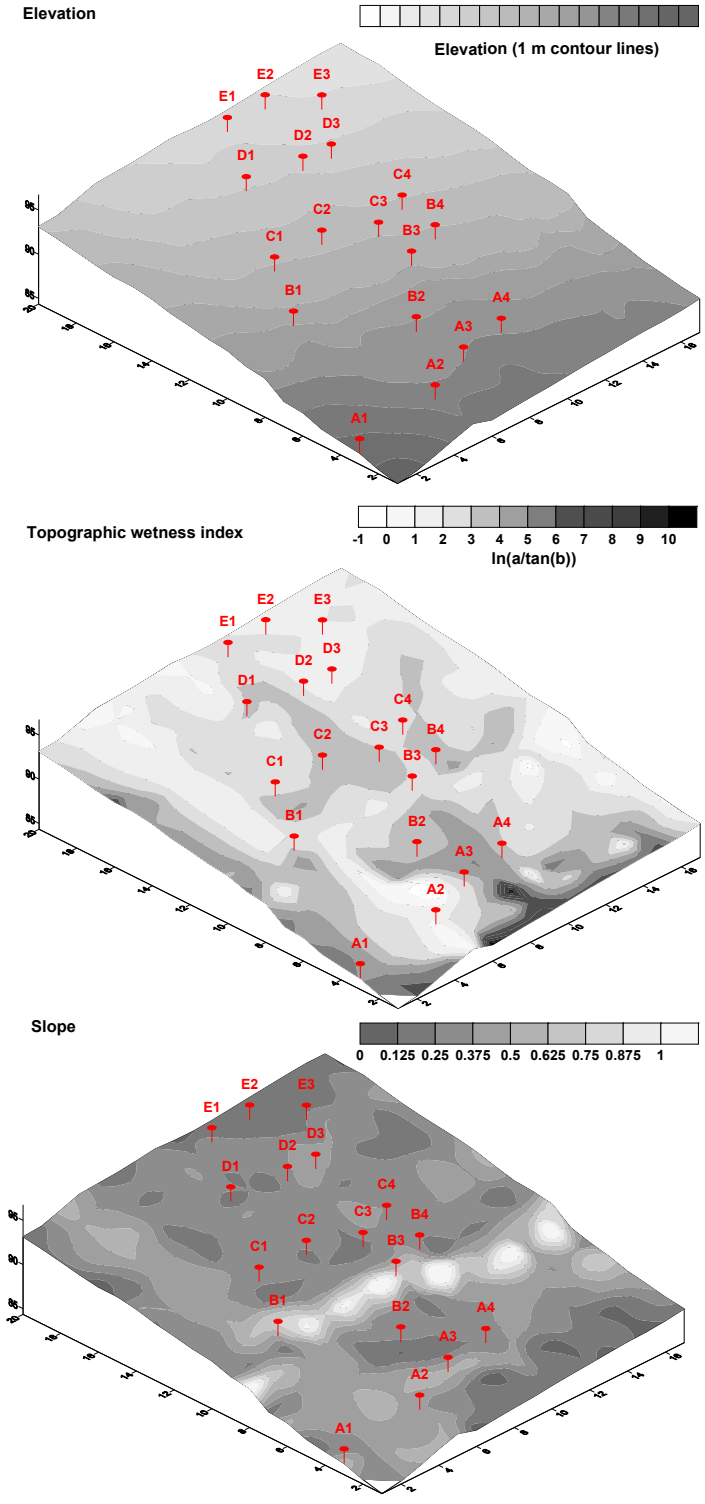

Figure 2.4. Photo of fractured bedrock along the logging road's cut-bank shown in Figure 2.2.

3: INFILTRATION AND RECHARGE INTO FRACTURED BEDROCK

3.1 Introduction

Over the last decade more research has focused on bedrock as both a control on, and a source of, subsurface flow. Recent research has indicated the importance of bedrock flow on the vertical and lateral aging of soil water (Asano et al. 2002; Uchida et al. 2006), its contribution to baseflow and stormflow (Terajima and Ishii 1993; Anderson et al. 1997; Onda et al. 2001; Uchida et al. 2003; Katsuyama et al. 2005; Tromp-van Meerveld et al. 2007), and its influence on the fate and transport of pollutants (Dano et al. 2008). Thus, to accurately model runoff it is necessary to be able to partition subsurface water into soil water and bedrock water, and to determine the rate of water transmittance through both.

Uchida et al. (2006) and Asano et al. (2002) observed that hillslope transient subsurface flow was temporally controlled by the vertical infiltration through the soil layer and into the bedrock. They found that bedrock with a high permeability can transmit and store more water, which increases the residence times, leads to vertical aging of water, and sustains baseflow. Tromp-van Meerveld et al. (2007) showed that for the trenched hillslope in the Panola Mountain Research Watershed (Atlanta, GA, USA) ponding at the soil-bedrock interface induced significant leakage into the permeable bedrock. This bedrock leakage was

significant during and directly following storms, and likely contributed to the sustained stream flow at the catchment scale during prolonged dry periods. Katsuyama et al. (2005) used both hydrometric and tracer data to examine the contribution of flow into and through permeable bedrock at the hillslope scale. The results of their study illuminated the importance of the hillslope's contribution to streamflow and its connectivity to the riparian zone via bedrock exfiltration. Dano et al. (2008) found that effluent from an individual sewage disposal system infiltrated into both weathered and fractured metamorphic bedrock. Lateral fluid fluxes along the bedrock were found to move further downhill (20+m) under wet conditions and significantly less under dry conditions (5 m). They also showed how the connectivity of uphill fractures can move water to local areas of exfiltration. These studies describe the importance of bedrock flow and how bedrock flow can move water from the hillslope to the stream, but do not describe how infiltration into permeable bedrock and fractured bedrock occurs or can be represented in simple hydrological models.

For infiltration into bedrock (matrix or fractured) to occur, percolation of rainfall must reach the soil-bedrock interface. In steep, humid watersheds, with shallow soil depths this has been frequently observed (Hutchison and Moore 2000; Montgomery et al. 1997). For the water to pond on the bedrock, there must be a decrease in hydraulic conductivity at the soil-bedrock interface. Ponding and subsequent bedrock infiltration is enhanced when the bedrock topography creates ponds and barriers that restrict lateral subsurface flow (Tromp-van Meerveld and McDonnell, 2006). Once a water table is present at the soil-

bedrock interface the hydraulic conductivity of the bedrock matrix or fractures determines the infiltration rate into the bedrock, while the contrast in hydraulic conductivity of the soil and the bedrock at the soil-bedrock interface determines the partitioning of this water into lateral subsurface and bedrock flow.

As is the case for infiltration into soil, infiltration into the bedrock matrix can be characterized by the matric potential and (un)saturated hydraulic conductivity (Philip 1992). When the bedrock is unsaturated the infiltration rate is determined by the difference in matric potential between the bedrock and the overlying soil, along with the unsaturated hydraulic conductivity of the bedrock. Under these unsaturated conditions infiltration rates can be higher than the saturated hydraulic conductivity because of high matric potentials, similar to that of soil infiltration at the surface. Salve et al. (2008) present a summary of some temporal controls on fractured bedrock infiltration under saturated conditions such as clay swelling, erosion/deposition of infill, air entrapment, effect of lithophysal cavaties (natural cavities), and the plugging by surface biofilms.

Even though recent research has examined the permeability of bedrock in the lab and in the field (Uchida et al. 2003, 2006; Tromp-van Meerveld et al. 2007), few studies have quantified the hydraulic conductivity of the bedrock at the soil-bedrock interface or determined bedrock infiltration rates in the field. Most research has either used isotopes, tensiometric/hydrometric data, or the mass balance approach to identify the portion of subsurface flow that infiltrates in the bedrock or has measured the hydraulic conductivity of the bedrock in a lab or through boreholes and/or fracture mapping.

Bedrock infiltration has been studied in the field by Salve et al. (2008), who investigated infiltration rates into a highly fractured welded ash tuff over prolonged periods (157, 216, and 422 day periods). Their results showed high initial rates of infiltration followed by a sharp decrease, similar to soil infiltration. However, following the decrease in infiltration rates, a surge in infiltration occurred after several weeks of inundation. The surge was followed by a relatively gradual decrease in infiltration rates. Observed infiltration rates were compared with the Philip (1969) infiltration model to illuminate the differences between bedrock infiltration and soil infiltration theory. Salve et al. (2008) suggest that these abnormalities occurred because of increased fracture permeability, which was possibly a function of clay swelling and particle erosion/infill within the fracture. Their findings also suggested that infiltration into fractured bedrock was spatially and temporally variable due to the tortuous character of fractures.

The objective of this study is to determine if water will infiltrate into the bedrock in the MKRF study watershed and, if so, if infiltration into bedrock can be described with simple infiltration models (i.e. the Horton, Philip, and Green and Ampt models) that have been developed for soils. To answer this question, I used constant head infiltration ponds, along with hydrometric data. In this chapter, I describe the best-fit model for both non-fractured and fractured bedrock ponds to gain insight into bedrock infiltration process at the MKRF fieldsite. Specifically, I compare the observed cumulative infiltration to the Philip, Horton, and Green and Ampt models to determine which model best represents infiltration into the bedrock. The hydraulic properties of the fractured and non-

fractured bedrock obtained from these models are compared with those of the soil to determine the importance of bedrock infiltration on subsurface stormflow at the watershed scale. Falling head infiltration tests were also conducted on two bedrock core samples to gain insight into the effects of scale on the estimated hydraulic conductivity of the bedrock.

3.2 Methods

3.2.1 Field experiments

Constant head infiltration tests were done on three bedrock outcrops to measure the infiltration rates into the bedrock and determine the saturated hydraulic conductivity of the bedrock. The sites had shallow soils (< 10 cm) and were situated above small cliff bans that empty into the study watershed and hence the stream (chapter 2, Figure 2.2). The sites were chosen to be practical in size while including both solid bedrock and fractures.

Pond 1 was a site with no visible fractures (< 0.5 mm fracture aperture). The exposed site for pond 2 was selected because it was a bedrock depression that ran along a linear transect of small trees (Figure 3.1), which suggested that a fracture zone existed. Stothoff et al. (1999) found that root growth followed fractures in a linear form, therefore suggesting that tree growth correlated well with fracture presence. The site for pond 3 (Figure 3.2) was chosen to be a larger area that would incorporate more fractures in both size and frequency. The area and ponding depths for all three ponds are given in table 3.1.

The shallow soil was left in place in an attempt not to disturb the soil-bedrock interface and, thus potentially changing the infiltration rates. The removal of all of the media has been found to increase sediment filling in the fractures (Salve et al. 2008) and alter “natural” infiltration rates. Trenches 15-30 cm wide were manually excavated to the bedrock along the perimeter of each pond site. Within the trenches the loose media was swept away from the bedrock in order to epoxy pond walls to the bedrock. The pond walls were constructed from 3 mm PVC sheeting. Epoxy (Powerfil 10 EH, Industrial Formulators and Aqua-Set Wet/Cold Curing, Coast Fiber-Tek Products, Burnaby, BC) was used to seal the impervious pond walls to the bedrock. Epoxy was placed on the outside and in some cases the inside of the walls to increase strength and prevent leaking.

Water was stored in a 121 L reservoir (with a lid) next to each pond, which maintained the constant head in the ponds with a one-way float valve. When the pond level dropped (due to infiltration into the bedrock) water moved from the reservoir to the pond maintaining the constant depth in the pond. The rate of outflow from the reservoir (and thus the infiltration rate) was recorded by observing the water level in the reservoir with two capacitance-loggers (Odyssey, Christchurch, New Zealand) (Figure 3.3). The water level recorders were set to record data every five minutes. Corrugated plastic sheeting and plastic wrap covered the infiltration ponds to prevent evaporation from leaving and precipitation from entering the ponds.

Infiltration into Pond 1 was examined from October 17, 2008 to November 19, 2008 (33 days). The infiltration experiment at Pond 1 was run a second time

between August 18, 2009 and September 17, 2009 (30 days). Pond 2 was filled on December 5, 2008 and infiltration was monitored until December 14, 2008 (9 days). Pond 3 was run from November 11to November 17, 2009 (6 days). The bedrock under all ponds was wet due to testing for leaks in the days prior to the start of the experiments.

3.2.2 Rock core experiments

Five rock samples from the watershed were collected for lab experiments to examine their hydraulic properties and characteristics. Samples originated from areas near fracture rock faces and were taken from the road surface (Figure 2.4, chapter 2) and could be affected by weathering. Weathering could affect hydraulic conductivity. Two large quartz diorite rock samples (T1 and T9) were used in falling head infiltration tests. Sample T1 was heavily fractured while sample T9 was only slightly fractured. The two samples used for the falling head infiltration test were placed in PVC cylinders that had radius of 14.5 cm. The cylinders with the rock samples were then filled with wax exposing only the top and bottom of the rock sample. The width and height of the rock samples were 17 by 26 cm for T1, respectively, and 12 by 16 cm for T9. Initial heads and starting time were recorded. The volume of exfiltrated water was recorded and converted to a change in water level in the core cyclinder and saturated hydraulic conductivity was calculated from the falling head equation:

$$K_{sat} = -\left(\frac{La}{At}\right) * \left(\frac{h_0}{h_t}\right) \qquad (3.2.1)$$

where L is the height of the core (cm), a is the cross section area of the cylinder (cm), A is the cross section area of the core (cm), t is time (hr), h_0 is the initial head (cm), and h_t is the head at time t (cm).

Three samples (two quartx diorite and one basalt) were used to determine the water retention curve. A basalt sample was taken from within the middle of the watershed (from the soil-bedrock interface) and was used because basalt intrusions were mentioned to exist in the MKRF and the sample was found in the watershed (Utting 1979) (though it could have been transported glacially).The small samples used for the water retention curve were ~400 cm^3. Samples for the water retention curve were saturated and weighed, measured for volume, and oven dried at 105° C for one week. They were then re-saturated and weighed at matric potentials ranging from 0 to -75 cm.

3.2.2.1 Soil hydraulic conductivity at the soil-bedrock interface

To determine the hydraulic conductivity of the soil at the soil-bedrock interface, falling head slug tests were performed on all piezometers on the hillslope (see chapter 2 for locations). The Horslev (1951) equation that was used is:

$$K = \frac{r^2 \ln(L/R)}{2LT_0} \tag{3.2.2}$$

where L (mm) is the length of the piezometer intake, R (18.5 mm) is the radius of the well casing, r (18.5 mm) is the radius of the well, and T_0 is the time it takes for the water level to fall to 37 percent of the initial change. A capacitance water

level recorder, set at a recording interval of 5 seconds, was used to measure the water level.Tests were run twice at each location to compute an average hydraulic conductivity.

3.2.3 Models

Three simple soil infiltration models were used to simulate the observed bedrock cumulative infiltration: the Horton, Philip, and Green and Ampt models.

Horton

The Horton (1940) model describes the infiltration rate, i, as:

$$i = f_c + (f_0 - f_c)\exp(-kt) \tag{3.2.3}$$

where f_c (m/s) is the steady-state infiltration rate, f_0 (m/s) is the initial infiltration rate, t is time (s), and k (s) is the time decay constant. Cumulative infiltration, I, is given by:

$$I = f_c t + \frac{f_0 - f}{k}\left(1 - \exp(-kt)\right) \tag{3.2.4}$$

Under ponded conditions f_c is assumed to be approximately equal to the saturated hydraulic conductivity (Dingman 2002).

Philip

Philip (1969) described ponded infiltration, *i* (m/s), as:

$$i = 0.5St^{-1/2} + K_S \tag{3.2.5}$$

where K_S (m/s) is assumed to be the saturated hydraulic conductivity, S ($m/s^{0.5}$) is the sorptivity, and t (s) is time. Philip developed this model under assumptions of one-dimensional infiltration into homogenous, semi-infinite media. Cumulative infiltration, I, can then be calculated as:

$$I = St^{1/2} + K_S t \tag{3.2.6}$$

Green and Ampt

In the Green and Ampt (1911) model infiltrability, f(t) (m/s), is given as:

$$f(t) = K_S \cdot \left[1 + \frac{\left|\Psi_f\right| \cdot (\Phi - \theta)}{F(t)} \right] \tag{3.2.7}$$

for,

$$t_p \le t \le t_w$$

where ψ_f (cm) is the effective tension at the wetting front (absolute value), Φ (cm) is the porosity, and θ is the water content, and F(t) is the cumulative infiltration as a function of time. The equation is valid when time, t, is greater than or equal to the time of ponding, t_p, and less than or equal to time of wetting, t_w. The parameters t_p and t_w are used to account for varying ponding times during soil infiltration. For this research the ponding occurs at a constant height during the whole duration of the experiments and, therefore, the equation is applicable. This equation assumes that the wetting front moves in a piston like manner where there is no variation in location at the depth of the wetting front. With the relationship between f(t), F(t), and t:

$$f(t) = \frac{dF(t)}{dt} \tag{3.2.8}$$

equation 3.2.7 can be written to solve for time as:

$$t = \frac{F(t) - F(t_p)}{K_S} + \left[\frac{\left|\Psi_f\right| \cdot (\Phi - \theta)}{K_S}\right] \cdot \ln\left[\frac{F(t_p) + \left|\Psi_f\right| \cdot (\Phi - \theta)}{F(t) + \left|\Psi_f\right| \cdot (\Phi - \theta)}\right] + t_p \qquad (3.2.9)$$

Since equation 3.2.10 cannot be solved explicitly as a function of time it requires arbitrarily choosing values of cumulative infiltration, F(t), and solving for time (Dingman, 2002). In the case of this research equation 3.2.10 has been rewritten to solve for F(t). The equation is:

$$F(t) = \left(\frac{t}{K_S}\right) + \left[\frac{(\Psi_f \cdot \Delta\theta)}{K_S}\right] \cdot \ln\left\{1 + \left[\frac{t}{(\Psi_f \cdot \Delta\theta)}\right]\right\} \qquad (3.2.10)$$

where $\Delta\theta$ is equivalent to $(\Phi-\theta)$.

3.3 Results

3.3.1 Observed cumulative infiltration rates

Pond 1

Cumulative infiltration into the bedrock increased rapidly during the first 96 hours (Figures 3.4; 3.5). Over the remaining ~674 hours cumulative infiltration increased slowly. Variation in the observations over the last 674 hours can only be explained by instrument error. The slow increasing trend upward, suggests continued infiltration. Cumulative infiltration was compared with local ambient daily mean temperatures to see if evaporation/condensation within the reservoir could account for the cyclic variation in the last 674 hours. Results of the comparison showed no correlation with mean daily temperature over the period

(r^2 = 0.07, p= 0.001). A slightly stronger correlation (r^2 = 0.09, p= 0.11) could be explained with a ~4 day lag between temperature and water level in the reservoir, suggesting that the variation could be due to changes in the temperature of the water in the reservoir.

The experiment in pond 1 was repeated in August, 2009 and is referred to as "pond 1 (2)". The second experiment in pond 1 displayed similar infiltration patterns over the first 96 hours (Figure 3.5). A difference between the two experiments occurred in the first 12 hours, where cumulative infiltration for pond 1 (2) increased more quickly. After about 12 hours cumulative infiltration of pond 1(2) was 5 mm, at this point it no longer increases (i.e. it plateaus) until 60 hours. After 60 hours pond 1(2) and pond 1 had similar cumulative infiltration responses until hour 240. At hour 240 infiltration in pond 1(2) increased until hour 450 while pond 1 remains at almost a steady state. Infiltration rates increase even further between hour 450 and hour 500. After hour 500, pond 1(2) reached a steady state until the end of the experiment at hour 715. Pond 1(2) also shows the same cyclic variation error.

Pond 2

Like Pond 1, cumulative infiltration in pond 2 increased rapidly initially (Figures 3.4, 3.5). During the first 12 hours cumulative infiltration was 1.5 mm. Over the next 208 hours cumulative infiltration increased, but at a slower rate. After 216 hours a leak in the pond occurred and the experiment had to be terminated. From the beginning of the experiment to ~208 hours after the start of the experiment, cumulative infiltration appeared to be similar to that of pond 1

(Figure 3.4), except that infiltration rates during the first 24 hours were faster than for pond 1 (Figure 3.5).

Pond 3

Cumulative infiltration for pond 3 was significantly different from pond 1 and 2. Cumulative infiltration was more than 315 mm for the first 140 hours (Figure 3.4). The infiltration rate was steady over the first 40 hours. Between hours 40 to 50 infiltration rate decreased, then increased between hours 50 and 80. This pattern repeated during hours 80-135 and 135-141. After 142 hours the reservoir ran out of water and the experiment was terminated. The three increased infiltration rates that occurred at hours 0-40, 50-80, 80-135, and 135-141 were $1.1\ 10^{-6}$, $9.8\ 10^{-7}$, $5.1\ 10^{-8}$, and $1.7\ 10^{-6}$ mm/s, respectively.

3.3.2 Fitted cumulative infiltration models

The Horton, Philip and Green and Ampt models were fitted to the observed cumulative infiltration data. All three models were fitted by finding the minimum sum of squared error using solver in Microsoft Excel. The mean squared error (MSE), correlation coefficient (r), and the mean absolute error (MAE) were used to describe the best-fit models (Table 2).

All three models appeared to slightly underestimate and overestimate the observed cumulative infiltration at different times (Figure 3.6, 3.7). The Horton model described the data for pond 1 best (highest r and lowest MAE/MSE). The correlation coefficient was 0.96; the MSE and MAE values were 0.35 (mm^2) and 0.48 (mm), respectively, for the Horton model. The Horton model visually

described the initial infiltration and the prolonged, yet minor, upward trend in cumulative infiltration best (Figure 3.7). For pond 1, both the Green and Ampt and Philip model underestimated infiltration initially and then overestimated the late-time infiltration.

Similar to pond 1, pond 1(2) was described best by the Horton model (r = 0.96, MSE=5.6 mm^2, MAE=1.7 mm) (table 3.2, Figure 3.7). Both the Horton and Philip models underestimated the cumulative infiltration in the first 25 hours (Figure 3.7). The Philip model (r = 0.96, MSE=5.8 mm^2, MAE=1.8 mm) was similar to the Horton model but underestimated the first 25 hours to a larger degree. The Green and Ampt model performed similarly to the Philip model. For the first 30 hours the Green and Ampt model underestimated the cumulative infiltration to a lesser degree than the Horton model.

The Horton model also described the observed results for pond 2 best (r = 0.99, MSE=0.07 mm^2, MAE=0.21 mm). The Horton model best represented the first 12 hours of infiltration. The Philip model initially underestimated the observations, and then followed the Horton model (Figure 3.7). The Green and Ampt model for pond 2 underestimated cumulative infiltration for the majority of the time of observation.

The Horton model fitted the observations for pond 3 best as well (Figure 3.6, 3.7). Both the Horton and Philip models were unable to accurately represent the observations when infiltration rates increased. The Horton model represented the first 40 hours well (Figure 3.6). After hour 40 both models underestimated and overestimated the observations at different times. The Philip model had similar

patterns to those of the Horton model but did not represent the first 40 hours as well as the Horton model (Figure 3.6). The Green and Ampt model underestimated the initial infiltration and overestimated the final infiltration rates.

3.3.3 Estimated hydraulic properties of the bedrock

Fitting the infiltration models to the observed cumulative infiltration allowed for the use of the inverse method to estimate the hydraulic properties of the bedrock. Table 3.3 shows the optimized values for the hydraulic conductivity (K_{sat}), sorptivity (S), initial (f_o) and final (f_c) infiltration rates, time decay constant (k), change in moisture content ($\Delta\Theta$), and the effective wetting front suction (ψ_f). For the Horton model it is assumed that $f_c \approx K_{sat}$ under ponded conditions.

All models showed that the saturated hydraulic conductivity for pond 1 was 10^{-10} m/s. The Horton and Green and Ampt models showed that pond 1(2) had a hydraulic conductivity of 10^{-8} m/s, two orders of magnitude larger than the results for the first experiment in this pond. The Philip model found that the hydraulic conductivity of pond 1(2) was 10^{-9} m/s. The Horton and Green and Ampt models showed that pond 2 had a hydraulic conductivity of 10^{-8} m/s, while the Philip model it was on the order of 10^{-9} m/s. All best-fitted models showed that pond 2 with the fracture had a hydraulic conductivity that was one to two orders of magnitude larger than that of pond 1. The Horton model showed that pond 3 had a hydraulic conductivity of 10^{-8} m/s, while the Philip and Green and Ampt models gave 10^{-7} m/s. The fitted hydraulic conductivity for pond 3 was thus one to two orders of magnitude larger than the smaller ponds (ponds 1 and 2).

3.3.4 Parameter uncertainty

To determine the uncertainty of the parameters used in the Philip and Horton models 250,000 Monte-Carlo simulations were done. A Monte-Carlo simulation is a method used to define the model parameters by running random parameter values through a given model. Appendix 2 shows the Matlab™ code for these simulations. Ranges were determined by the parameter values of the 250 (0.1%) best-fits (blue dots in Figures 3.8-3.10). The correlation coefficient was found to be a poor evaluator of the parameter values for both models and all ponds because the correlation was good for all parameter values (Figure 3.8; used as an example). The MSE and MAE were found to be better measures to identify the range and sensitivity of the parameters (Figure 3.9 and 3.10), but still gave large ranges. Table 3.4 and Figure 3.11 show the ranges of the parameters. The acceptable (i.e. 0.1% best-fit) hydraulic conductivity values as determined by the Horton model varied over eight orders of magnitude for pond 1, and nine orders of magnitude for pond 1(2) and pond 2, and eleven orders of magnitude for pond 3. The Philip model gave smaller ranges for all ponds of one order of magnitude, except for pond 1. This suggests that the Philip model may give more accurate ranges, but the inability to fit the model to observations well implies that the model gives small ranges for the wrong hydraulic conductivities. The insensitivity of the models to hydraulic conductivity parameters suggests that the optimized values may not accurately reflect the actual bedrock conductivity. The overlapping conductivity ranges suggest that the hydraulic conductivity is not significantly different between ponds, even though the optimized values were an order of magnitude different (Figure 3.11).

3.3.5 Falling head core tests and water retention curves

The falling head core tests gave saturated hydraulic conductivities of 10^{-7} and 10^{-8} m/s for cores T1 and T9, respectively. Preferential flow paths were observed when blue dye was introduced in the reservoir of T9 after a week. Blue water droplets along with clear water droplets were observed at the bottom of the core on day 7 of the falling head test (Figure 3.12). This shows that water passes through the rock at varying rates.

The basalt rock sample had water contents between 9 and 12% and trends in a negative direction as matric potential decreases (appendix 1, Figure A3; bottom). The water content of the quartz diorite samples ranged between 2 and 3% and released less water than that of basalt. Along with the soil sample taken from the watershed (appendix 1, Figure A3; top), these results show the differences in the moisture storage between soil and bedrock found within the MKRF.

3.4 Discussion

3.4.1 Comparison to soil infiltration

Infiltration into soil is commonly described by an initial high rate of infiltration followed by a decline towards a steady state rate (Hornberger 1998). The reduction in infiltration with time is associated with weakening of the matric potential gradient and sometimes the deterioration of soil structure or creation of a soil crust (Salve et al. 2008).

This research has shown that infiltration into bedrock at the storm time scale (hours to days) is similar to that of infiltration into soils. For pond 1, where no major fractures were visible, infiltration patterns were similar to those described by the common soil models: an initially large increase in cumulative infiltration (10^{-9} to 10^{-10} m/s, one order of magnitude higher than steady-state rates) followed by a slow, gradual increase when steady state infiltration rates are reached. Pond 1(2) is an exception in that it not only did the experiment yield larger hydraulic conductivities than pond 1 (even though it was the same pond), but it also showed abnormalities in trends similar to those described by Salve et al. (2008). Pond 1(2) had increases in infiltration rates that occurred after steady state infiltration was reached, similar to those described by Salve et al. (2008). This sudden increase could be caused by a very small leak in the pond at 240 hours. Even though a leak was not observed, it would explain the difference in infiltration patterns and saturated hydraulic conductivity values from those of experiment 1. However, a minor leak would not explain the low infiltration rates between 500-712 hours. A comparison of the first 240 hours shows that pond 1(2) responded more quickly, but had similar ranges for the hydraulic conductivities as given for pond 1 by the Monte-Carlo analysis (10^{-18}-10^{-9} m/s). Infiltration values (both initial and steady state) for the first 240 hours, however, were an order of magnitude larger (fitted; f_0: 1.4 10^{-6} to 4.0 10^{-7}; and f_c: 1.0 10^{-8} to 4.5 10^{-9} m/s for pond 1(2) and pond 1, respectively). Pond 2, with the fracture, also had an initial infiltration response similar to the theoretical models in that cumulative infiltration increased rapidly. This pond did not show the commonly

well defined steady infiltration rate because it did not reach the steady state infiltration rate prior to the leak. Cumulative infiltration for pond 3 increased far more quickly than that of any other pond. This was is most likely due to more frequent fractures in the larger area. Infiltration in pond 3 did show abnormalities in cumulative infiltration in the form of steps. These “steps” were different from common soil infiltration trends and more similar to the trends observed by Salve et al. (2008) for bedrock, as discussed in the next section. These steps or increases in cumulative infiltration occurred after 40, 50, and 80 hours.

Overall, the Horton model represented the observed data best. Both the Green and Ampt and Philip models overestimated and underestimated the observed data at times, especially during the start of the experiments. The sensitivity analyses gave large ranges for the hydraulic conductivities, along with the other parameters. This suggests that caution should be used when using best-fit model parameters as estimates for soil hydraulic properties.

3.4.2 Abnormalities in infiltration patterns

This research has shown that bedrock infiltration over a short period (up to several weeks) is similar to that of infiltration into soils. The simple soil infiltration models were capable of mimicking this infiltration. Abnormalities similar to those found by Salve et al. (2008) were, however, observed for pond 1(2) and pond 3. These observed increases in infiltration rates cannot be described by the simple models used in this paper. While the abnormalities in pond 1(2) may be caused by an unobserved small leak, those for pond 3 cannot be explained by a leak, as there were several increases and decreases in the infiltration rates. Salve et al.

(2008) found that infiltration rates peaked several weeks to months after initial infiltration patterns had resembled that of soil infiltration. They suggested that these abnormalities from classic soil infiltration were due to increased permeability due to the effects of clay swelling, erosion/deposition of fracture/surface minerals, enhancement or blockage of flow pathways by entrapped air, lithophysal cavities, or clogging of fractures by biological materials. This work addressed several of the explanations by Salve et al. (2008) in the research design by leaving the soil above the bedrock intact.

Clay swelling

Clay swelling can increase fracture aperture thereby increasing the hydraulic conductivity of the fracture, but it can also block fluid flow. Salve et al. (2008) assume that clay swells in direction normal to the fracture plane thereby increasing the fracture aperture and consequently, the rate of fluid flow through the fracture. In order to explain the increase in infiltration rates, they found that clay swelling requires smaller (<0.1 mm) fracture apertures to be filled with clay. Clay concentrations in the soils within the research forest are low (<5%, de Vries and Chow 1978; Bryck 1975), and the humid climate would keep the clay moist in contrast to the Yucca Mountain, NV site of Salve et al. (2008). This suggests that clay swelling did not likely cause the abnormalities observed in pond 1(2) and pond 3.

Erosion/deposition of fracture and surface minerals

The erosion of surface materials and their emplacement in fractures can clog the fractures thereby decreasing infiltration rates, or increase infiltration rates by the dislodging of infill within fracture walls. Salve et al. (2008) showed that an increase in permeability by a factor of 17 is possible during infiltration for a single planar fracture with a uniform aperture when the initial degree of clogging infill is very high (99% filled) or when the infill and/or fracture walls are easily erodible (i.e. soft rock). In this research, the soil was left in place to not disrupt the soil-bedrock interface and reduce the potential of infill from soil into the fractures. The ponding of water above fractured bedrock increases the transport potential of sediment into fractures, which shows how this process could influence permeability and, therefore, infiltration into fractured bedrock. The quartz bedrock that underlies the research site is hard (relative to the Mohs scale), so erosion (during the time span of the experiments) within the fractured bedrock does not seem to be a likely explanation for the increased infiltration rates in pond 1(2) and 3.

Enhancement or blockage of flow pathways by entrapped air

The enhancement or blockage of flow pathways by entrapped air can occur when air is trapped between infiltrating water and an impervious (to air) lower boundary, or the occlusion of air by obstructions in air filled fractures. Salve et al. (2008) noted that an impervious layer was unlikely because of well connected fractures within the bedrock. The bedrock in the research forest was observed to have fractures that extend both vertically (Figure 2.3, chapter 2) and horizontally

for several meters (personal observation). It is assumed that these fractures are connected and that air is able to escape, but in cases where a bedrock water table exists and bedrock infiltration is uniform air entrapment could occur. The occlusion of air was explained by Salve et al. (2008) to occur when fast flowing water creates a "bubble" of air in the fracture. When the bubble “pops” an increase in infiltration is possible. This second explanation is very plausible and could explain the repeated increases and decreases in infiltration rates that were observed for pond 3. Further investigation on air entrapment is needed.

Lithophysal cavities

The influence of lithophysal cavities as explained by Salve et al. (2008) requires further research. The observed abnormalities in bedrock infiltration that showed a delayed increase in infiltration rates were explained to be a function of the need for pressure thresholds to be reached before the cavities can fill (Salve et al. 2008). Increased infiltration rates were caused by increased bedrock storage from the cavities. Field observations in this research watershed do not show lithophysal cavities, which occur more so in felsic volcanic rock, which suggests that this is an unlikely explanation for the abnormalities observed in ponds 1(2) and 3.

Clogging of fractures by biological materials

Salve et al. (2008) found that a decrease in infiltration rates occurred over several weeks of ponding and that after biofilm was scrubbed away an increase in infiltration was observed. The film was only present on hard surfaces. This research reduced the potential for this mechanism to reduce infiltration rates by

using shorter ponding durations and leaving the majority of the natural soil in place. No film was observed during the experiments.

3.4.3 Differences between the infiltration ponds/effects of scale

The two main differences between the three ponds are their size and the presence/absence of visible fractures. The optimized hydraulic conductivity values for all ponds suggest that the presence of fractures changes the hydraulic conductivity one order of magnitude (comparison of pond 1 and 2). The initial infiltration rates in the first 12 hours were 9.7 10^{-9}, 2.3 10^{-7}, 1.9 10^{-7}, and 1.1 10^{-6} m/s for ponds 1, 1(2), 2, and 3, respectively. The rate of infiltration in pond 3 over this period was ~115 times faster than that of pond 1. The rock core samples used in the falling head permeameters had hydraulic conductivies10^{-7} m/s for the more fractured sample and 10^{-8} m/s for the less fractured sample. The results of saturated hydraulic conductivities as a function of pond and core scale suggest that there is little influence of scale (Figure 3.11). The differences in hydraulic conductivities between ponds 1 and 3 could be a function of scale, but since the presence of fractures also increases it is difficult to say which has more of an influence.

It is hypothesized that the fracture frequency and preferential flow paths in fractured bedrock have a larger influence on hydraulic properties, and that the average fracture characteristics would be best described by the results from the largest pond. The similarity between the core samples and pond experiments indicates that small fracture characteristics are most significant in determining

infiltration rates at this study site. This can be seen in the preferential flow paths described by the dye observations.

The unknown fracture characteristics, together with the large uncertainty in the calculated hydraulic conductivity estimates, make it difficult to say that these results are representative of the watershed as a whole. It is more likely that fracture characteristics are highly variable and therefore the hydraulic conductivity of the bedrock is variable as well. The spatial variation in bedrock properties, along with spatial variability of water table presence and ponding depth (see chapter 4) makes prediction of infiltration rates into bedrock difficult.

3.4.4 Hydraulic conductivity of the bedrock

The optimization results suggest that the hydraulic conductivities are likely around 10^{-9} m/s for ponds 1(2) and 2 when using the Horton model. The initial infiltration rates (f_0) for the Horton model are likely 10^{-8} and 10^{-9} m/s for pond 1, 1(2), and 2, suggesting that the steady state infiltration rates are one to two orders of magnitude smaller than the initial infiltration rates (pond 3 is an exception which was 10^{-6} m/s). All results suggest that the hydraulic conductivities of the bedrock likely range from 10^{-7} to 10^{-10} m/s. Previous work examining the hydraulic conductivity of fractured quartz and granite bedrock has found similar values for the hydraulic conductivity (table 3.5). Weathered hydraulic conductivity values were larger for granite than those for quartz diorite, but all values fall well within the ranges given by the Monte-Carlo uncertainty analyses of this study.

3.4.5 Influence of bedrock infiltration on subsurface storm flow and the water balance

This research has described infiltration into bedrock over a period of days to weeks to resemble saturation patterns similar to transient saturation development on hillslopes during rainfall events. Though prolonged periods of inundation or water table presence are possible, such as simulated by Salve et al. (2008), they are not common on hillslopes in humid temperate climates. In the MKRF study watershed, transient saturation at the soil-bedrock interface has been shown to create a water table at the soil-bedrock interface similar to that of the experiments (i.e. < 0.2 m deep at most sites) (see chapter 4).

Past and present research has shown that the saturated hydraulic conductivity often decreases with depth (Harr, 1977). The hydraulic conductivity measured in a 30 cm diameter by 27.5 cm deep soil core from the study site was 10^{-4} m/s (Cheng, 2007), while the hydraulic conductivity of the soil at the soil-bedrock interface was on the order of 10^{-5} m/s. The hydraulic conductivity of the bedrock ranges from 10^{-7} m/s to 10^{-10} m/s in the watershed (table 3.6). The substantial decrease in hydraulic conductivity at the soil-bedrock interface (Figure 3.13) creates a boundary that promotes a transient saturated zone and lateral subsurface flow over the bedrock. Despite the large decline in hydraulic conductivity at the soil-bedrock interface, results from this research show that water could infiltrate into and move through the bedrock as well. The observed infiltration patterns indicate that the majority of the water that enters the bedrock would do so during the initial stages (hour-days) of transient saturation. Flow through bedrock can influence the timing, amount, and spatial distribution of

subsurface storm flow. Bedrock infiltration can increase the residence time and age of the water by retaining water within the hillslope longer. The retained water can exfiltrate at a time after the soil subsurface flow response has ended, contributing to a prolonged recession and base flow.

A rough estimate of potential bedrock infiltration as a fraction of precipitation was calculated by the equation:

$$Potential\ infiltration(\%) = \frac{observation\ days\ (338\ days) * water\ table\ persistence\ (34\%) * K_S(\frac{m}{s})}{Rainfall\ (1.56m)}$$

(3.4.1)

where rainfall and transient water table persistence were calculated over the same time period (10/7/2008 to 5/7/2009). Water table persistence was calculated by dividing time of a measurable water table (>7cm, see chapter 4) by the total measurement time. Averages were used for three piezometers on the hillslope (middle and bottom; A3, B3, and C3; see chapter 2). Best-fit values were used for the hydraulic conductivity values (table 3.7). This equation assumes that infiltration into bedrock is constant (at the steady state rate), driven by gravity only (i.e. a unit hydraulic gradient), and that the bedrock is saturated. This assumption would underestimate the actual infiltration rate since most infiltration occurs early in the events. The results of this calculation show that up to 9% of total rainfall could infiltrate into the bedrock (table 3.7).

Storm magnitude and duration play an important role in water table development. Larger storms with long durations result in higher water tables that last longer. Larger, intense storms would be affected relatively less by bedrock

infiltration losses than smaller storms because the majority of the water would move through the soil above the soil-bedrock interface. Because of the larger quantities infiltrating initially, the effects on larger storms would be a delay in hydrograph response (response lag). A small or absent hydrograph response for smaller low intensity storms with wet antecedent conditions would be an indication of permeable bedrock and significant losses to the bedrock.

Figure 3.14 shows the relationship between storm total precipitation and storm runoff for 17 events between 10/21/2008 to 10/21/2009. The three lines represent runoff ratios of 10, 25, and 45%. This relationship shows that for many events the runoff ratio is around 25% of the total precipitation. This suggests that for many rainfall events 75% of the precipitation does not result in a storm response and that less than 60% of precipitation resulted in storm response for all events. While interception loss, evapotranspiration and soil moisture storage can account for some of the loss, most of these events took place in fall and winter when evapotranspiration is low and the shallow soils have high moisture contents and therefore low storage capacities. Interception losses are ~15% (Chin, 2009). Bedrock infiltration losses could explain part of the difference between precipitation and storm runoff response.

3.5 Conclusion

To determine the infiltration rates into the bedrock and the saturated hydraulic conductivity of the bedrock, three 0.38 to 2.26 m^2 constant head infiltration tests were done on bedrock outcrops. Falling head permeameter tests were also done on two large bedrock cores. The Horton, Philip, and Green and Ampt models

were used to fit the observed cumulative infiltration rates. To determine the uncertainty of the parameters used in the models, Monte-Carlo simulations were done. This study has shown that:

1. The three soil infiltration models could describe the observed infiltration data well. These simple models can thus be used to describe bedrock losses in (simple) hydrologic models. The infiltration models were generally insensitive to changes in the model parameters, which resulted in large uncertainty ranges for the hydraulic conductivity parameters. The Horton model described cumulative infiltration best, especially during the initial infiltration stage, but had a large parameter uncertainty.
2. While the soil infiltration models could describe the infiltration rates, unexpected increases in infiltration rates were also observed during the experiments, especially for the largest pond (pond 3). This is in agreement with the results of Salve et al. (2008) who found increases and decreases in the infiltration rates after 2-3 weeks for a 3 x 4 m infiltration plot with 1m^2 subplots and concluded that infiltration into bedrock is different from soil infiltration. This research suggests that the abnormalities found in pond 1(2) and pond 3 may be caused by air entrapped in bedrock fractures that once released causes a rapid increase in infiltration rates.
3. The hydraulic conductivity of the bedrock cores were similar to those of the infiltration ponds. Core to pond scales were found to have little influence on the hydraulic conductivity suggesting that small fracture presence and preferential flow paths determine the hydraulic conductivity of the bedrock at this study site.
4. Blue dye flowed through a 17.5 cm long rock core within 7 days, thus describing preferential flow paths through fractured bedrock cores.
5. The results of this study show that water moves through the soil to the soil-bedrock interface. At the soil-bedrock interface water moves both laterally and vertically over and into the bedrock. It is feasible that for this study watershed up to 9% of rainfall can infiltrate into the bedrock with

faster bedrock infiltration occurring during the initial stages of the development of the transient saturated zone.

Thus, even though the hydraulic conductivity of the bedrock at the study site is several orders of magnitude smaller than the hydraulic conductivity of the soil, recharge into bedrock can be a significant component of the water balance. This has important implications for the residence time, water table dynamics, and the geochemical signature of stream water.

3.6 Figures

Figure 3.1. Photo of pond 1 (middle) and pond 2 (right), along with the reservoir (left). The fracture that runs under pond 2 is identified by the line with four small trees in the forefront of the reservoir and pond 1.

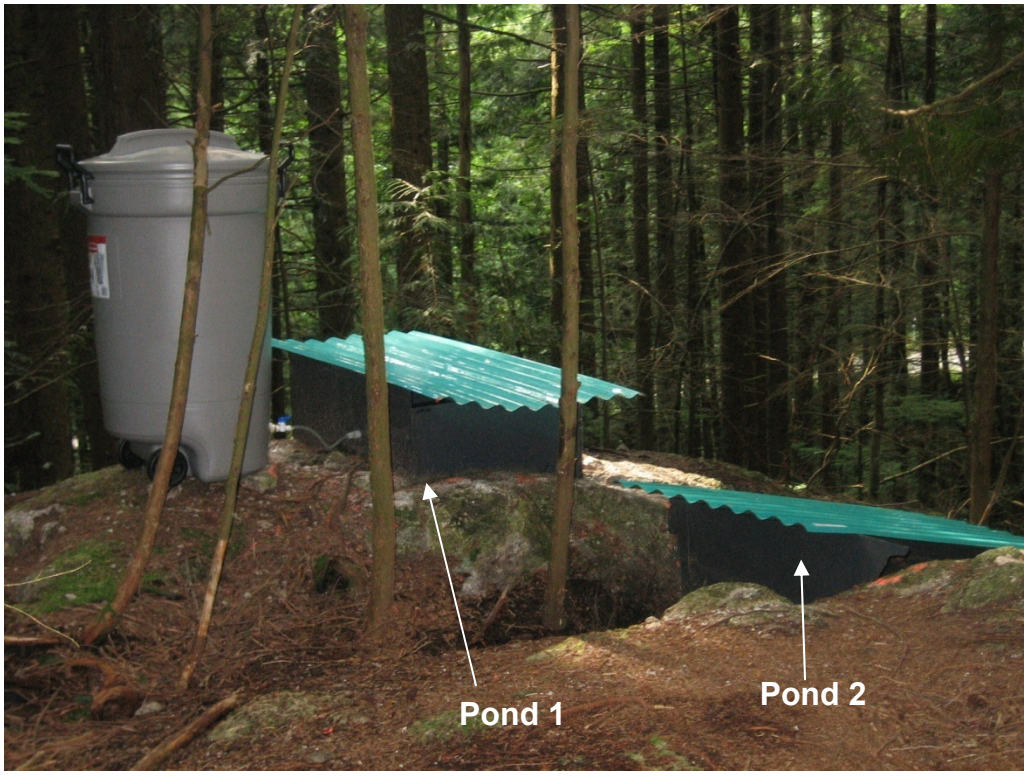

Figure 3.2. Photo of pond 3 prior to inundation.

Figure 3.3. Schematic of the infiltration ponds used in this research. For information on the specific widths, lengths, heights, and head levels see table 3.1.

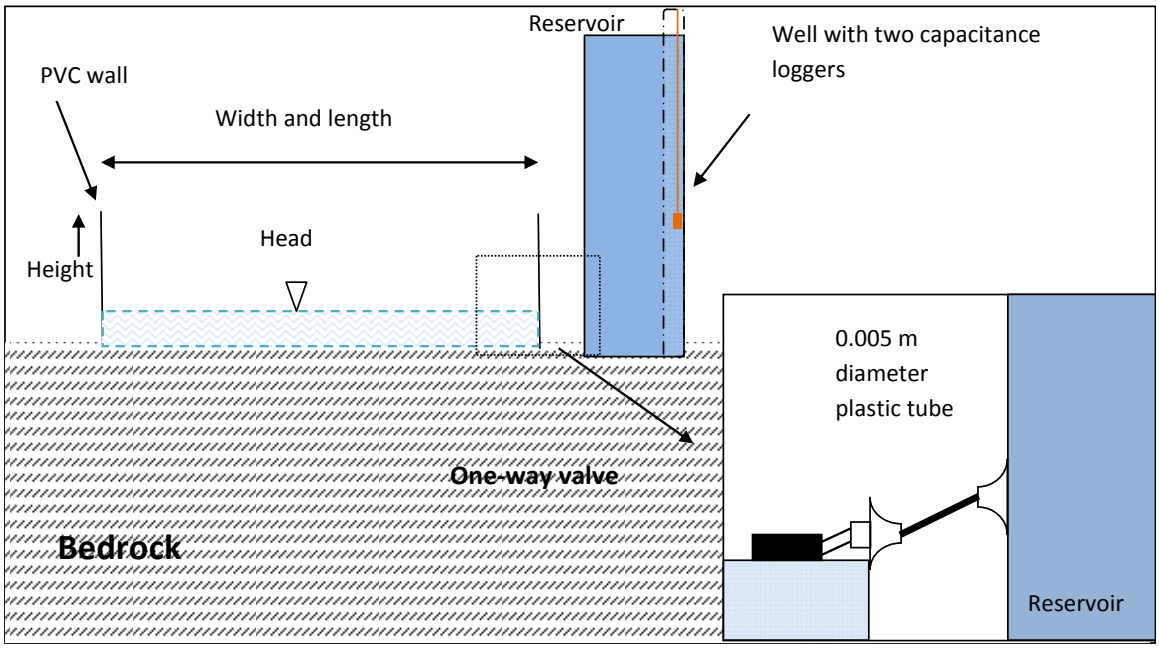

Figure 3.4. Observed cumulative infiltration for ponds 1, 1(2), 2 and 3 for 800 hours.

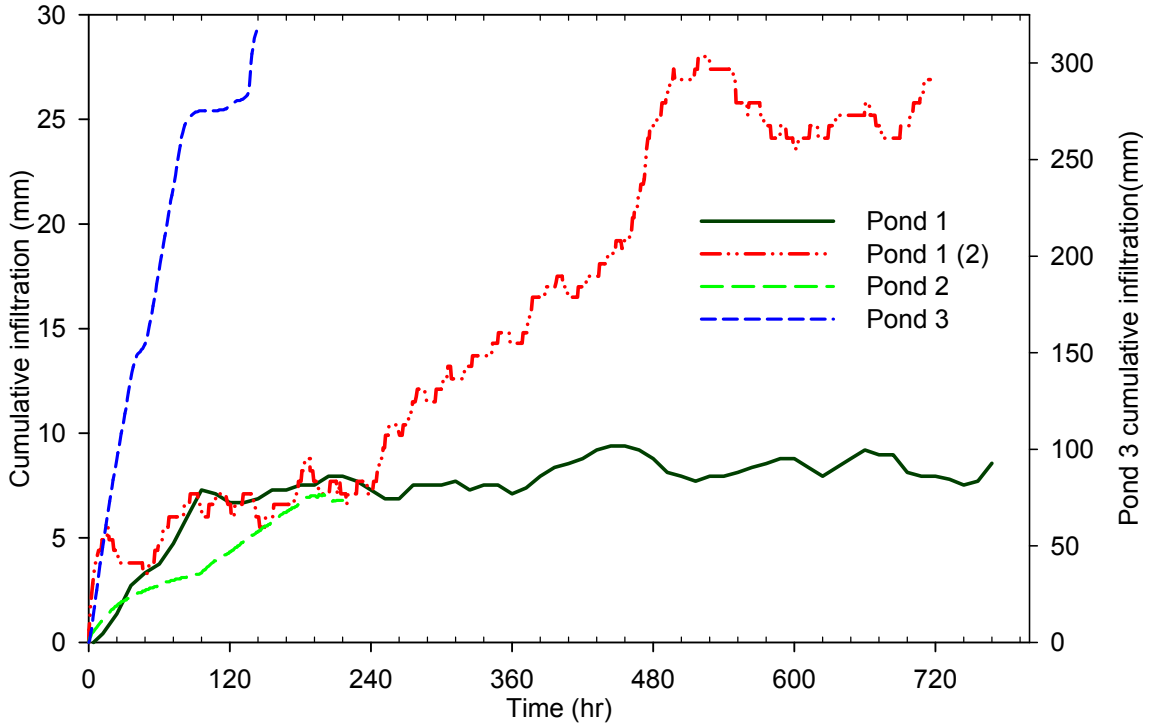

Figure 3.5. Observed cumulative infiltration for ponds 1, 1(2), 2, and 3 for the first 96 hours of the experiments.

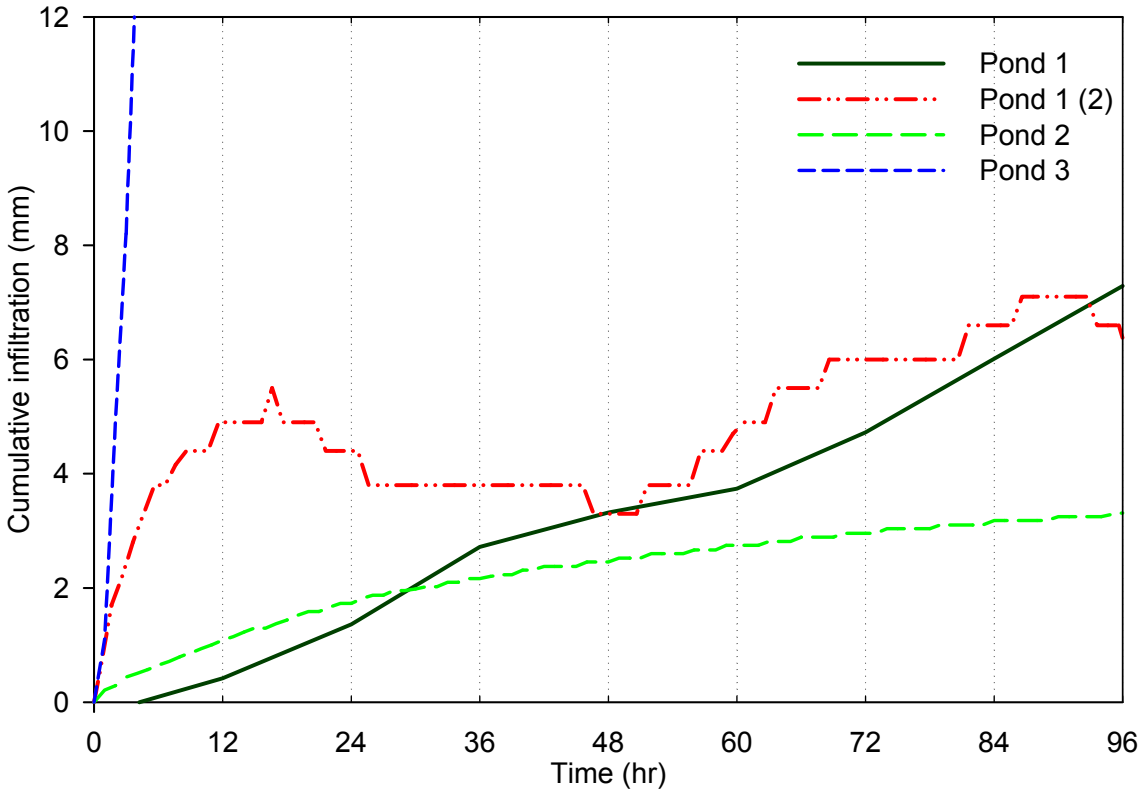

Figure 3.6. Observation and fitted cumulative infiltration for ponds 1, 1(2), 2, and 3.

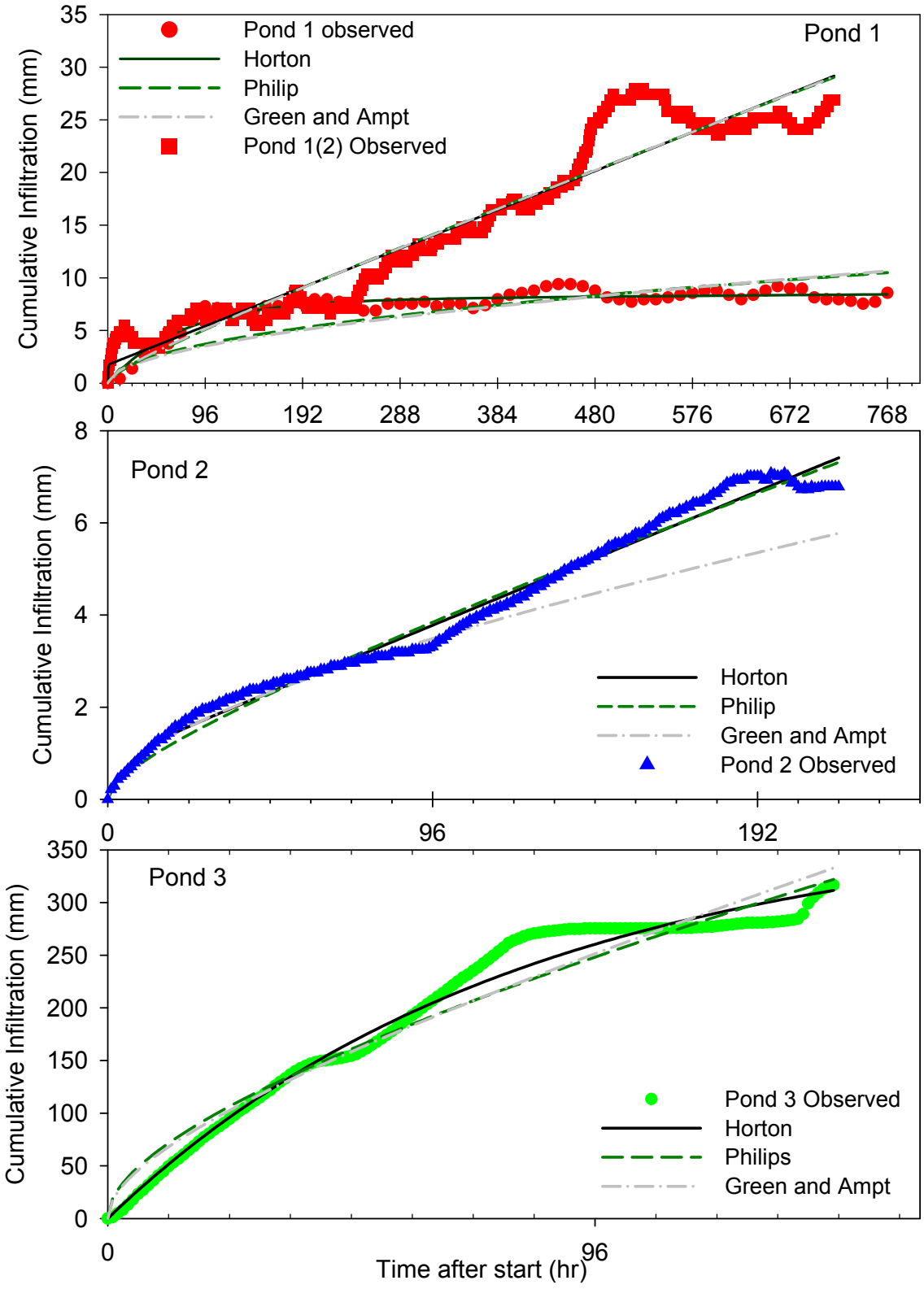

Figure 3.7. Relationship between observed and modeled cumulative infiltration for the Horton, Philip, and Green and Ampt models for both ponds 1, 1(2), 2 and 3.

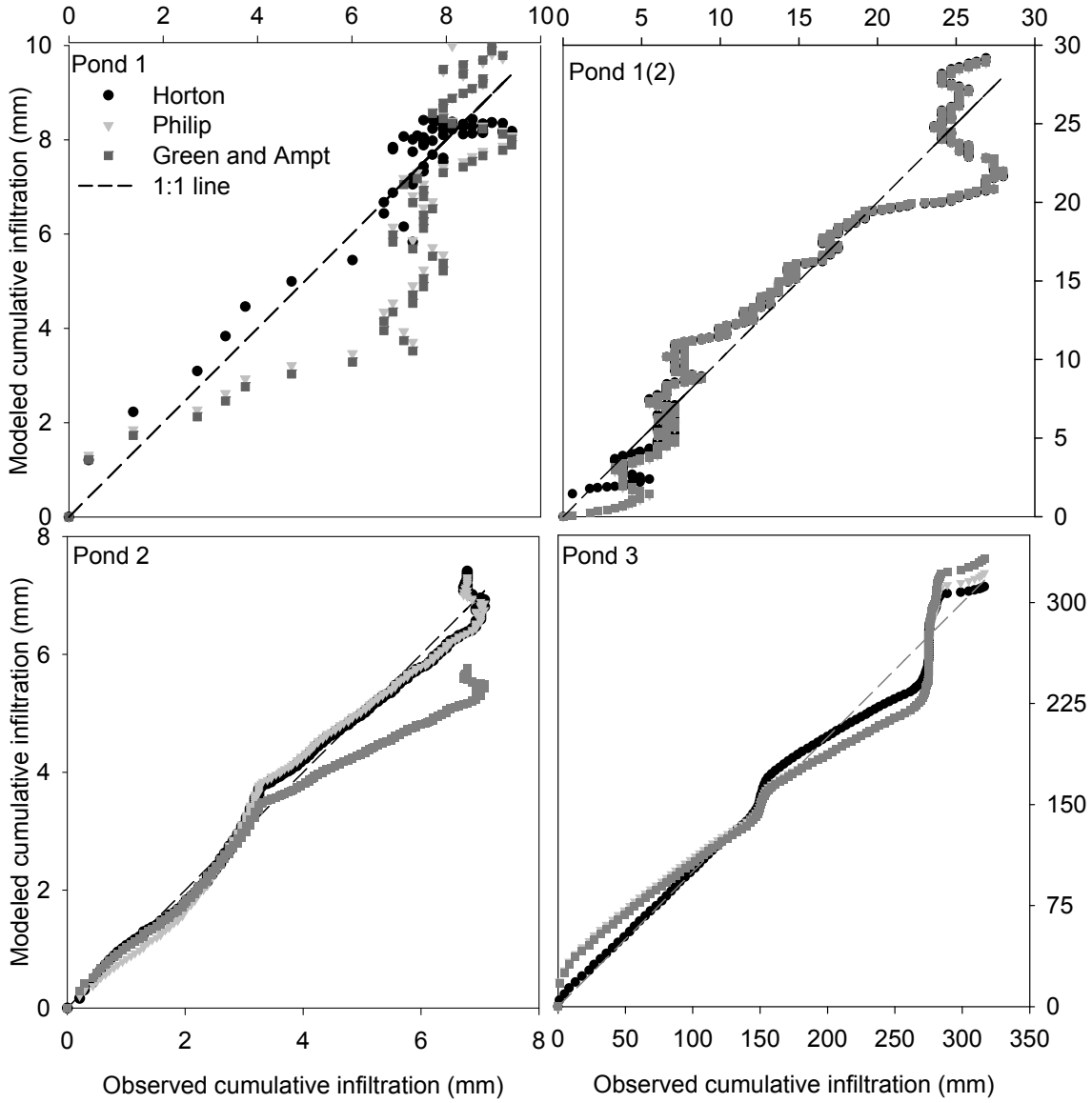

Figure 3.8. Dotty plots of the sensitivity of the Horton model for Pond 3 when using the correlation coefficient. The top graph describes the results for the initial infiltration parameter (f_o) while the middle graph shows the final infiltration or hydraulic conductivity (f_c) and the bottom graph shows the fitting parameter (k). The red star represents the maximum value. The solid blue dots represent the best 0.1% of the Monte-Carlo simulations and represent the acceptable range. These ranges can also be found in Table 3.4.

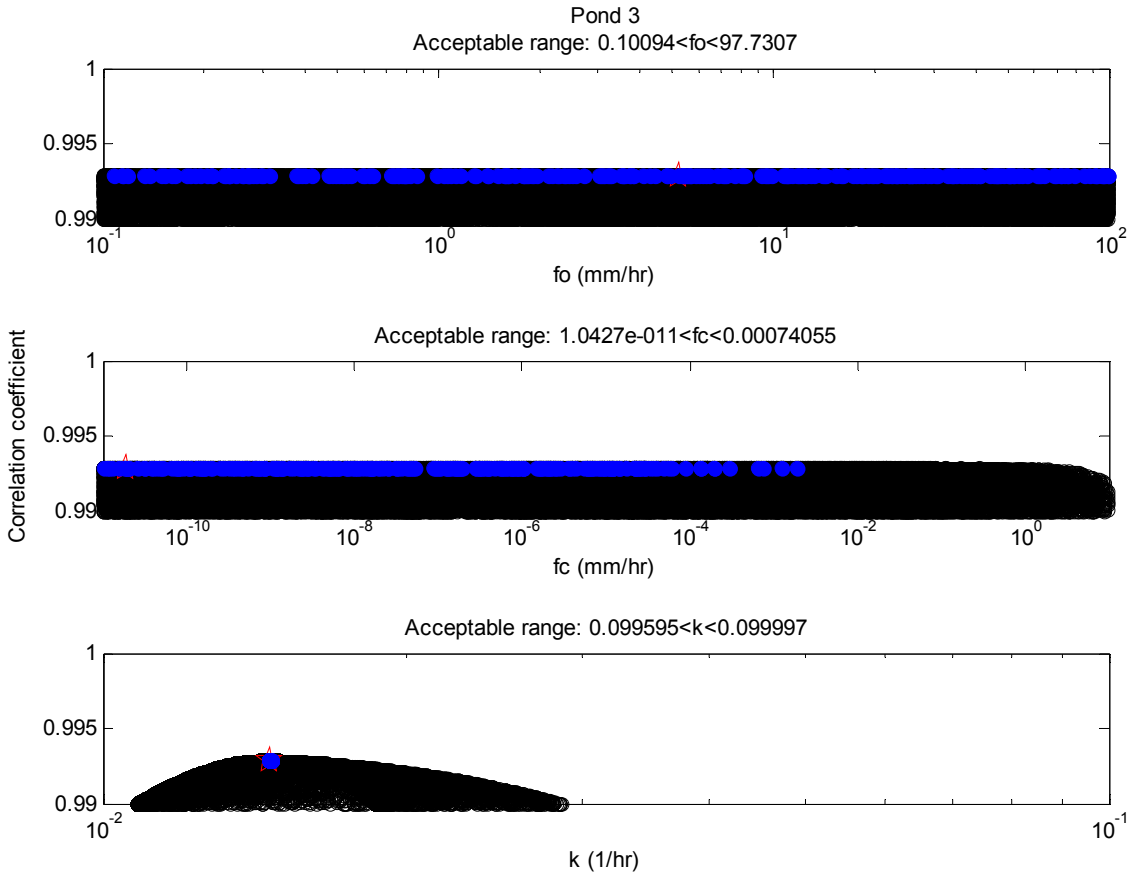

Figure 3.9. Dotty plots of the sensitivity of the Horton model for ponds a) 1, b) 1(2), c) 2, and d) 3 when using the MSE (except pond 3 which uses MAE because of its better evaluation). The top graph describes the initial infiltration parameter (f_o) while the middle graph describes the final infiltration or hydraulic conductivity (f_c) and the bottom graph describes the fitting parameter (k). The red star represents the minimum value. The solid blue dots represent the best 0.1% of the Monte-Carlo simulations and represent the acceptable range. These ranges can also be found in Table 3.4.

a)

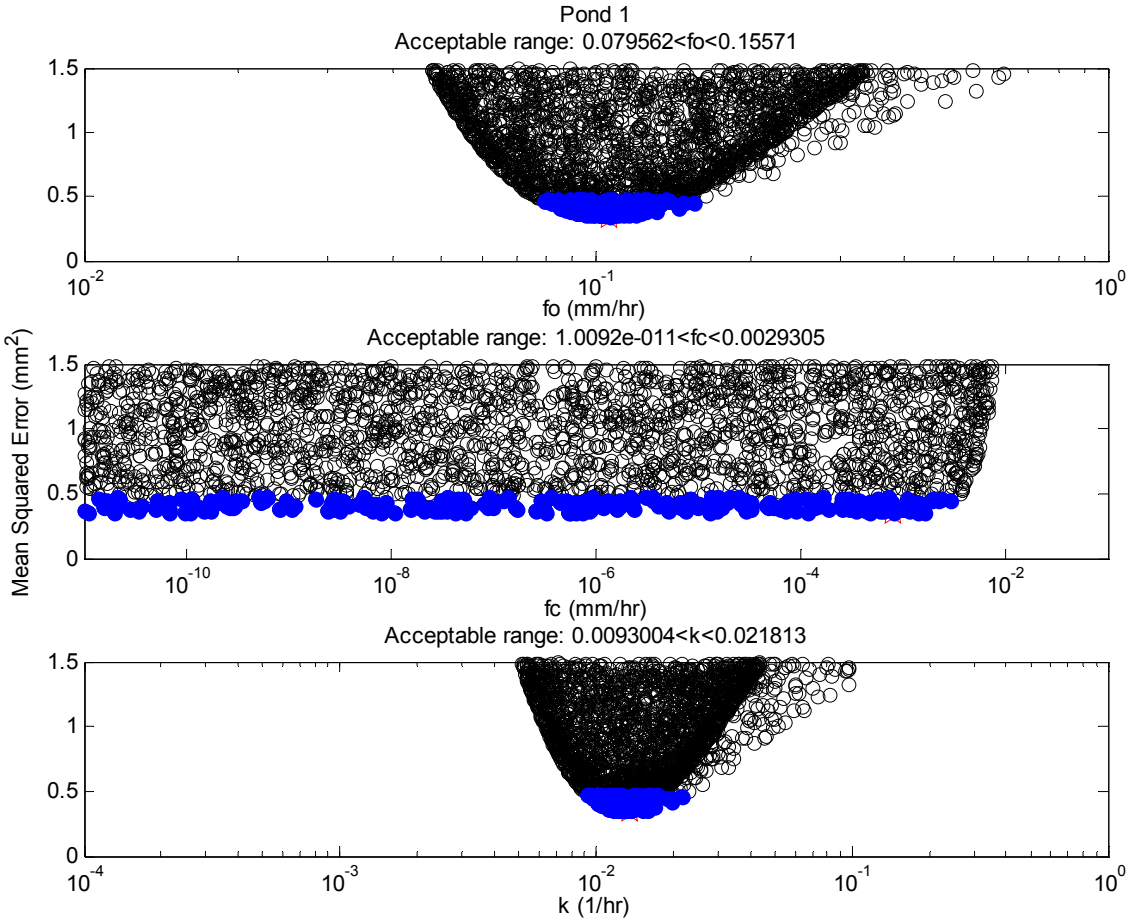

b)

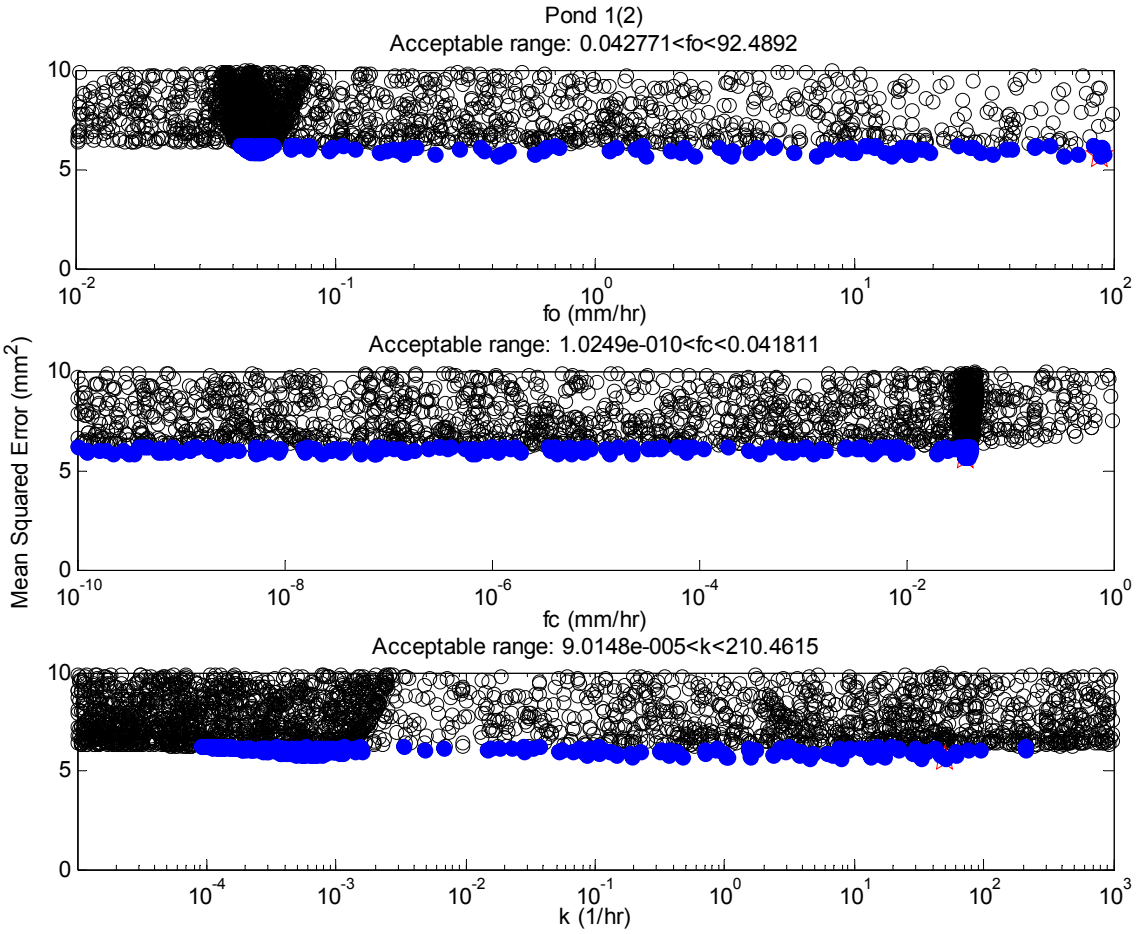
Pond 1(2)
Acceptable range: 0.042771<fo<92.4892
fo (mm/hr)
Acceptable range: 1.0249e-010<fc<0.041811
fc (mm/hr)
Acceptable range: 9.0148e-005<k<210.4615
k (1/hr)
Mean Squared Error (mm2)

c)

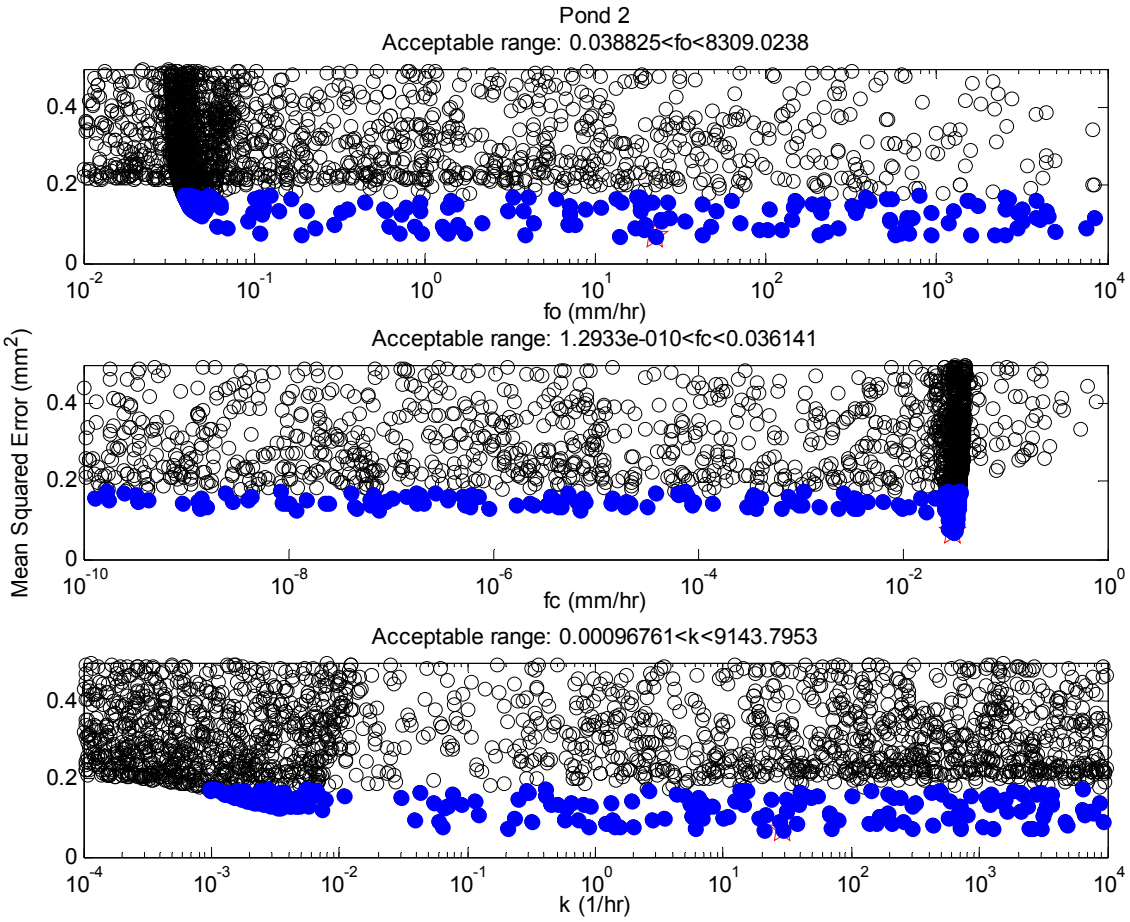
Pond 2
Acceptable range: 0.038825<fo<8309.0238
fo (mm/hr)
Acceptable range: 1.2933e-010<fc<0.036141
fc (mm/hr)
Acceptable range: 0.00096761<k<9143.7953
k (1/hr)
Mean Squared Error (mm2)

d)

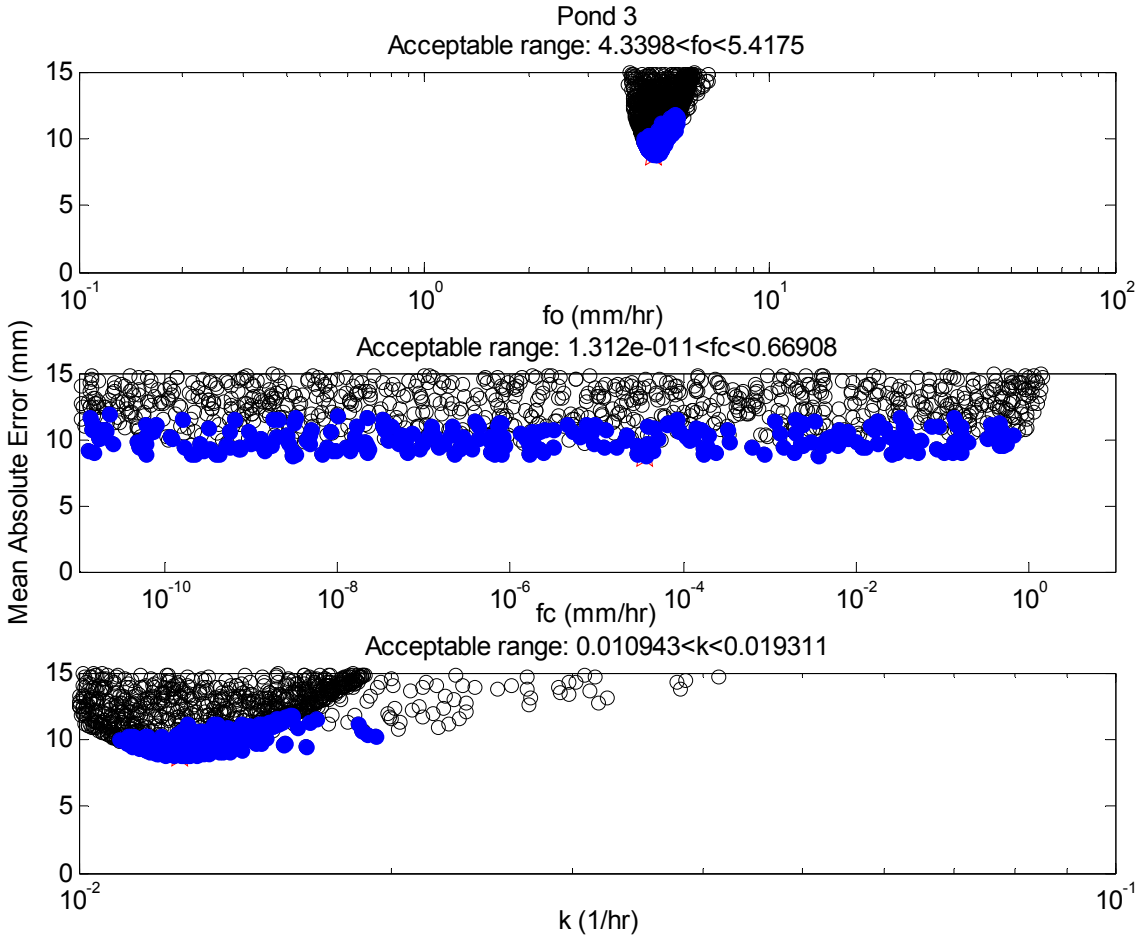
Pond 3
Acceptable range: 4.3398<fo<5.4175
fo (mm/hr)
Acceptable range: 1.312e-011<fc<0.66908
Mean Absolute Error (mm)
fc (mm/hr)
Acceptable range: 0.010943<k<0.019311
k (1/hr)

Figure 3.10. Dotty plots of the sensitivity of the Philip model for ponds a) 1, b) 1(2), c) 2, and d) 3 when using the MSE criteria (except pond 3 which uses MAE). The upper graph shows the results for the sorptivity parameter (S) while the bottom graph shows the hydraulic conductivity (K). The red star represents the minimum value (i.e. optimized). The solid blue dots represent the best 0.1% of the Monte-Carlo simulations and represent the acceptable range. These ranges can also be found in Table 3.4.

a)

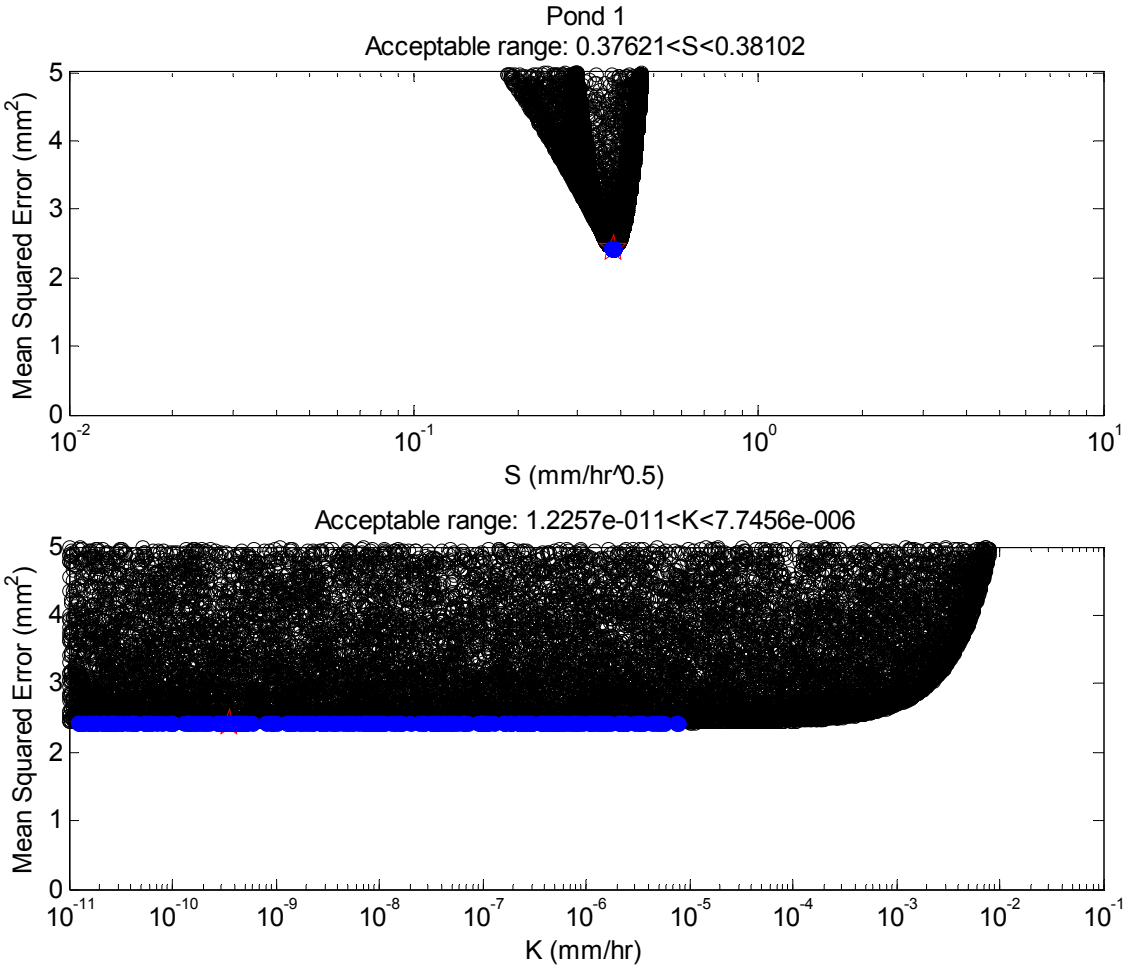

b)

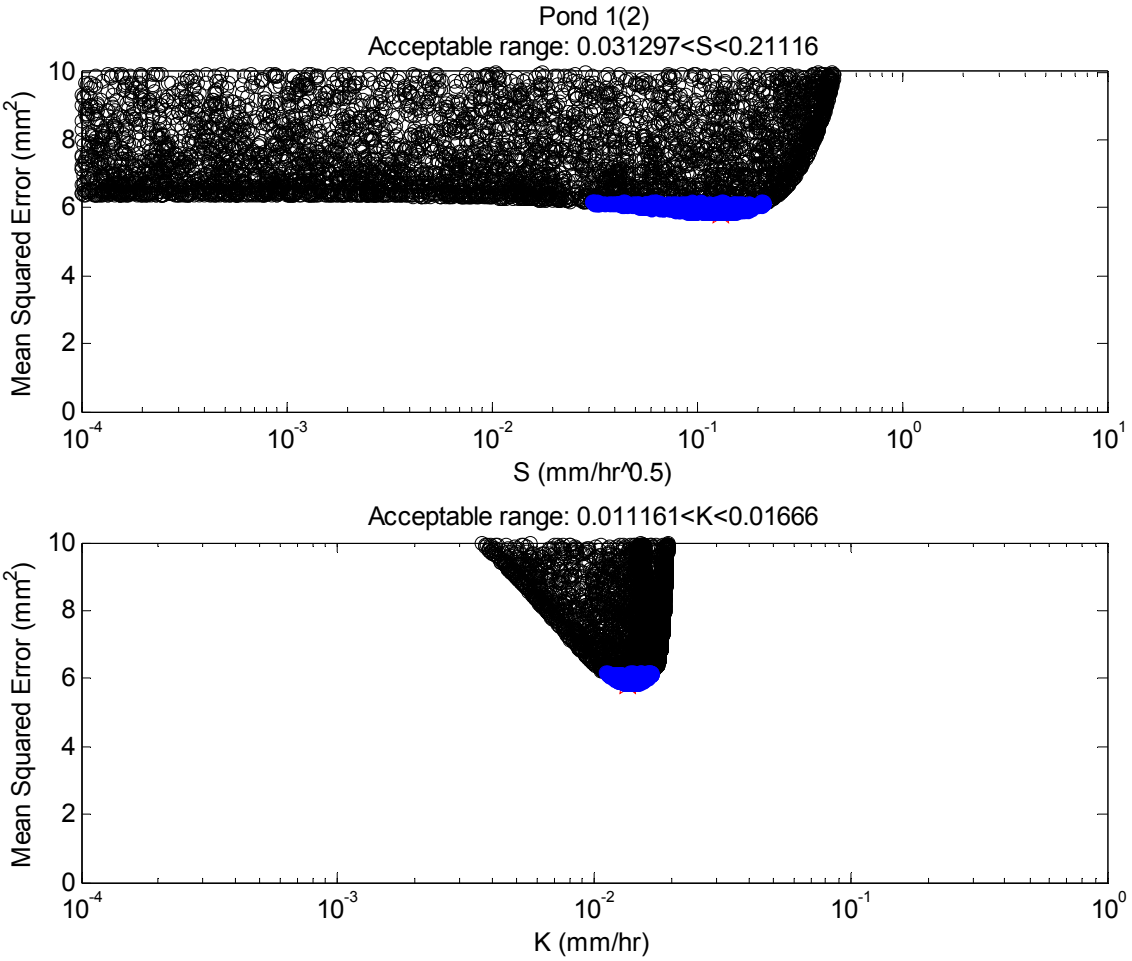
Pond 1(2)
Acceptable range: 0.031297<S<0.21116
Mean Squared Error (mm^2)
S (mm/hr^0.5)
Acceptable range: 0.011161<K<0.01666
Mean Squared Error (mm^2)
K (mm/hr)

c)

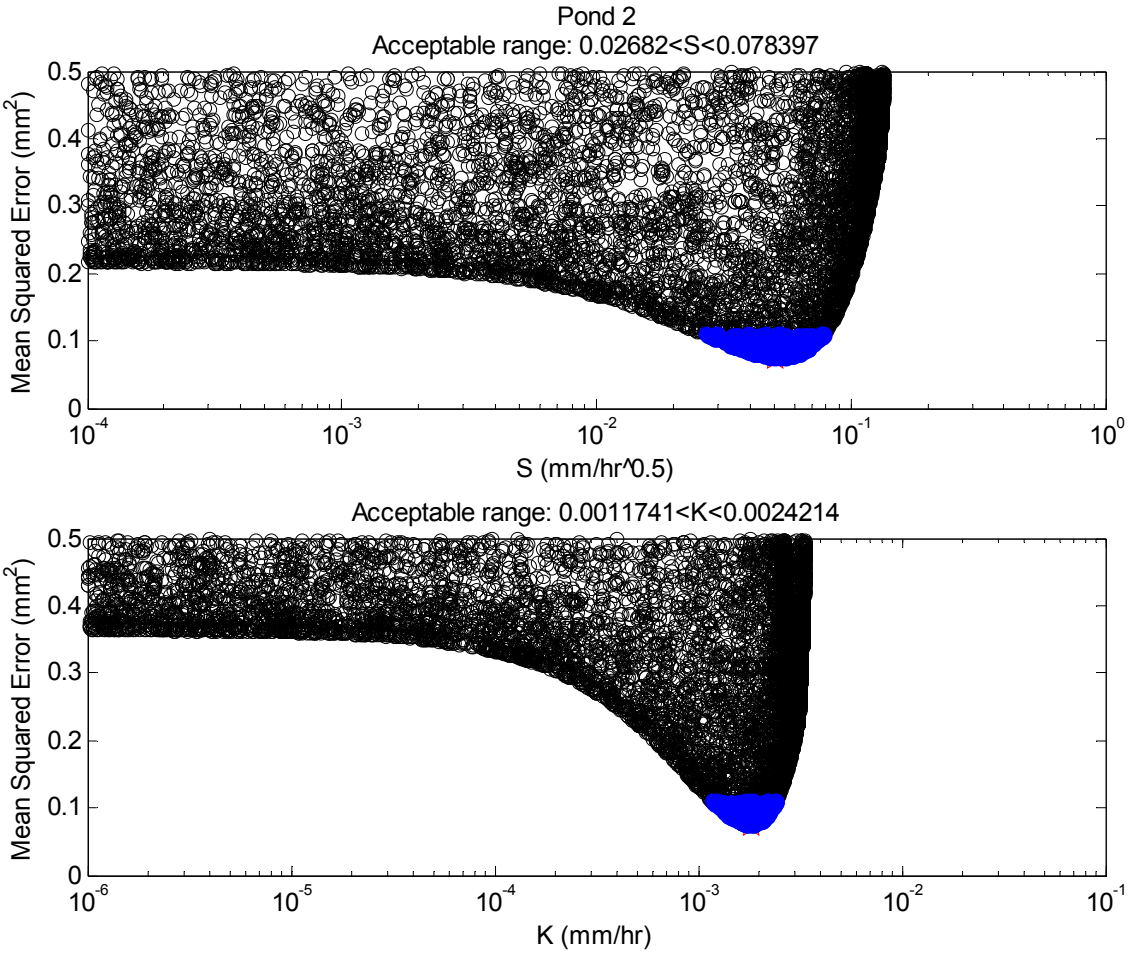
Pond 2
Acceptable range: 0.02682<S<0.078397
Mean Squared Error (mm^2)
0.5
0.4
0.3
0.2
0.1
0
10^-4
10^-3
10^-2
10^-1
10^0
S (mm/hr^0.5)
Acceptable range: 0.0011741<K<0.0024214
Mean Squared Error (mm^2)
0.5
0.4
0.3
0.2
0.1
0
10^-6
10^-5
10^-4
10^-3
10^-2
10^-1
K (mm/hr)

d)

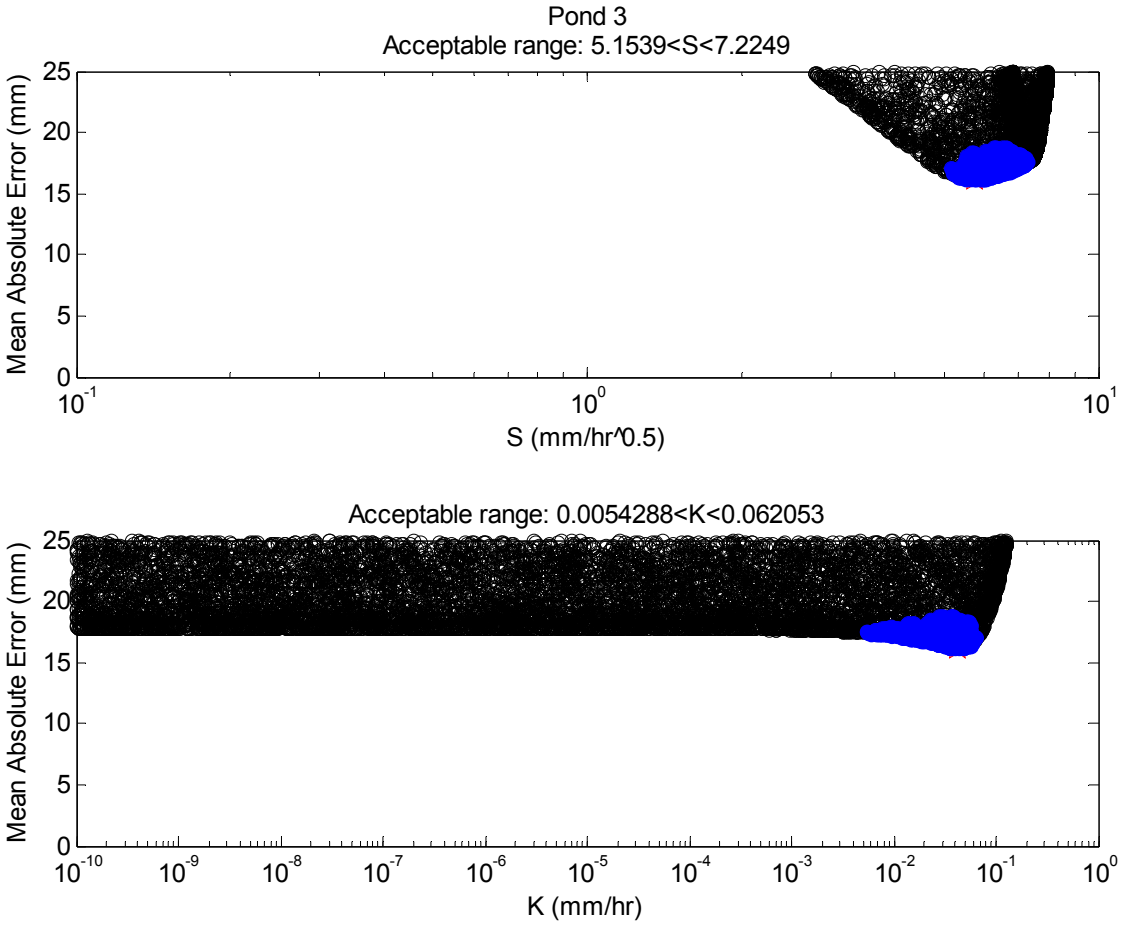
Pond 3
Acceptable range: 5.1539<S<7.2249
Mean Absolute Error (mm)
S (mm/hr^0.5)
Acceptable range: 0.0054288<K<0.062053
Mean Absolute Error (mm)
K (mm/hr)

Figure 3.11. The optimized hydraulic conductivities and the respective uncertainty ranges (as determined by the Monte-Carlo analyses) for all experiments as a function of scale (area). The triangles, circles, and squares represent the Horton, Philip, and Green and Ampt model results, respectively.

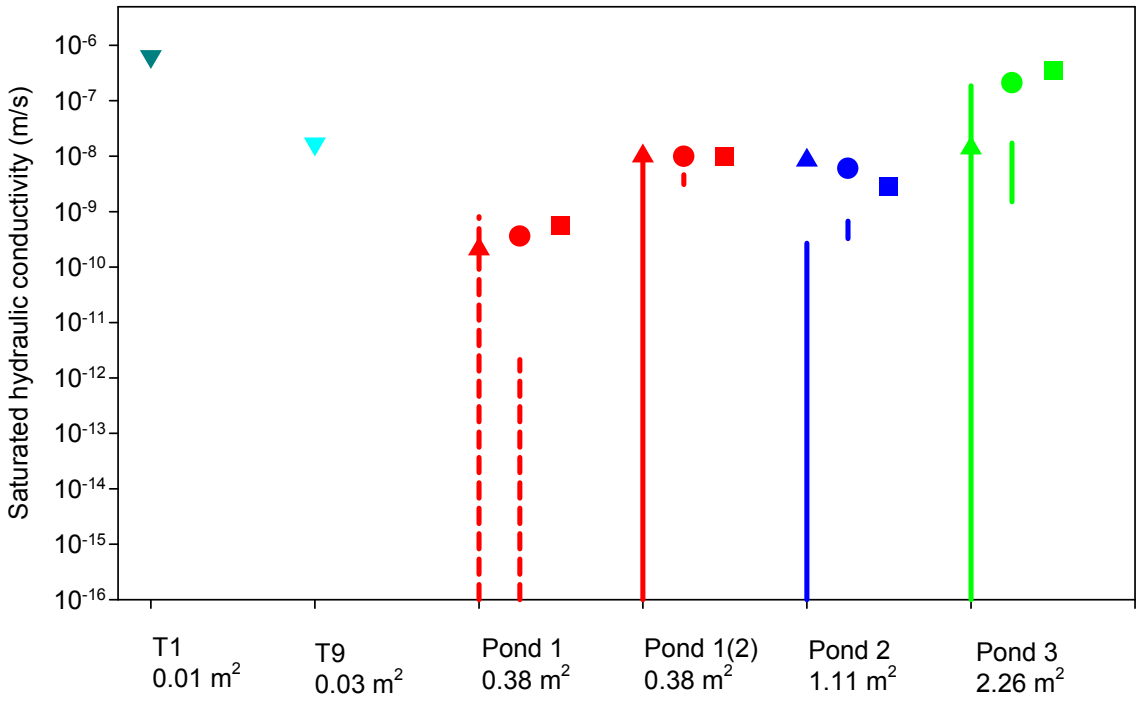

Figure 3.12. Photo of rock core T1. This figure shows preferential flow through fractures. Blue dye was introduced a week after the start of the falling head infiltration test. The clear water droplet shows that water is moving through the rock at different rates. Black arrows show locations of blue water drops and the white arrow shows the location of a clear water drop.

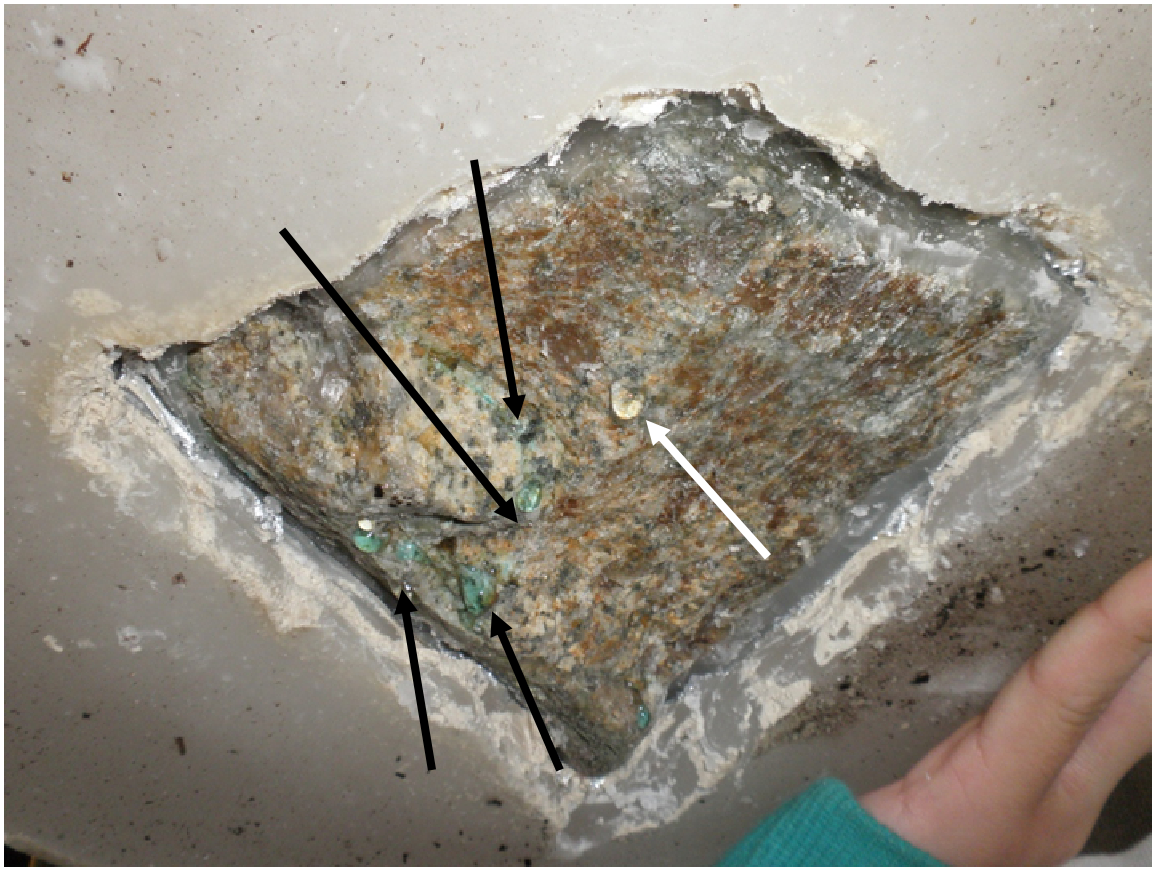

Figure 3.13. Hydraulic conductivity as a function of depth below the surface. Values from ponds 1, 1(2), 2, and 3 are the values determined by optimization for the different models.

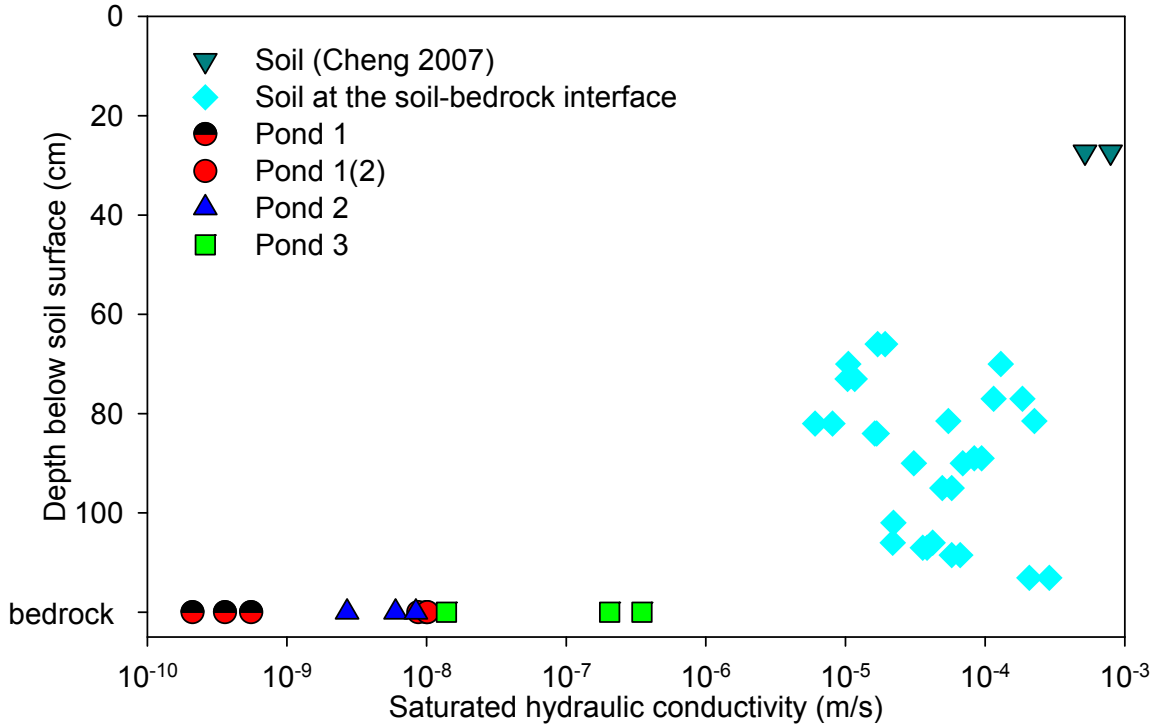

Figure 3.14. Relationship between total precipitation and storm runoff for events occurring between 10/2008 to 10/2009. Storm events were determined by periods of rainfall that lasted longer than 2 hours and were separated by breaks longer than 6 hours. Discharge totals for the related storms were calculated by subtracting the baseflow (using the slope method) prior to the event from the event response until it reached the new baseflow. Runoff was determined by finding the contributing area of the research watershed (17 ha; which can be found in appendix 2). Inset shows the runoff ratio for the same storms as a function of the total precipitation.

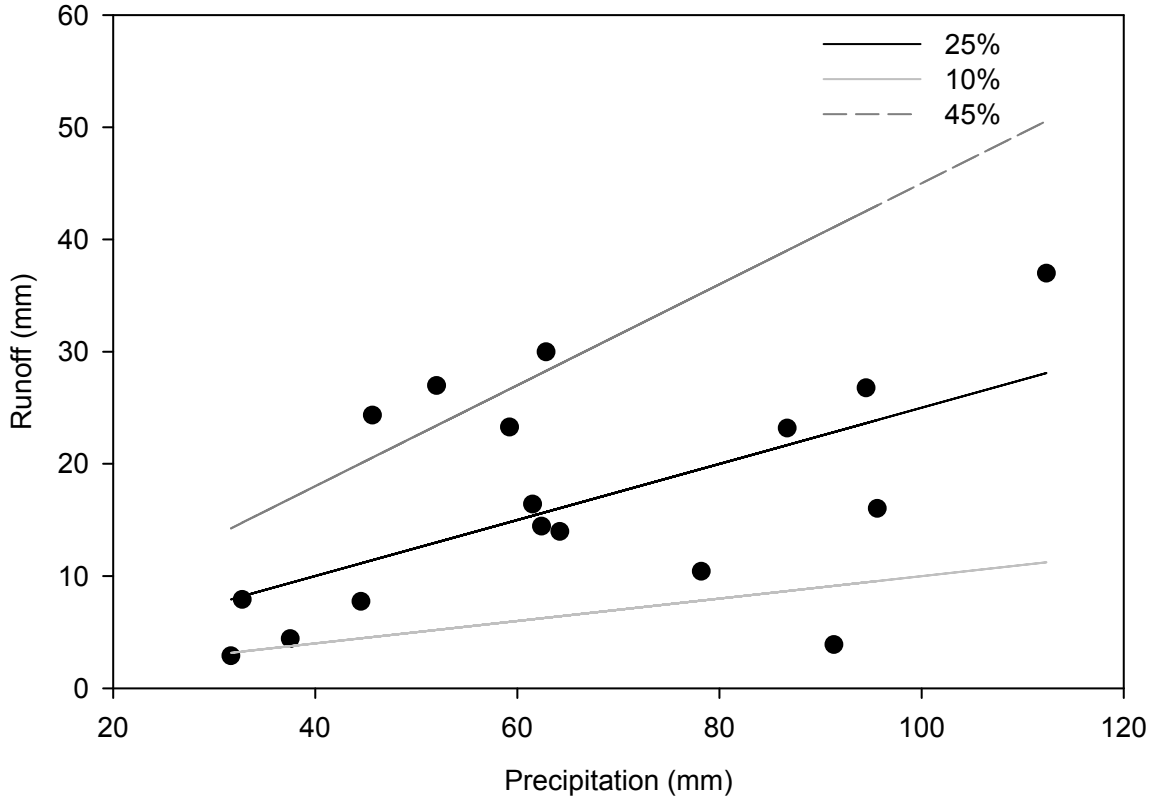

3.7 Tables

Table 3.1. Area, ponding depths, height, width, and length for all three ponds.

Pond	*Area*	*Head (average)*	*Height*	*Width (average)*	*Length (average)*
Pond 1	0.38 m^2	11.75 ± 4.6 cm	33 cm	51.5±2.1 cm	74.3±1.8 cm
Pond 2	1.11 m^2	~20 cm	33 cm	158.5±51.6 cm	182.5±3.5 cm
Pond 3	2.26 m^2	15 ± 5.0 cm	33 cm	127±11.3 cm	178±2.8 cm

Table 3.2. Values of the mean squared error (MSE), and mean absolute error (MAE), correlation coefficient (r) for ponds 1, 1(2), 2, and 3. The models were fit by minimizing sum of squared error between the model and observed values.

	Pond 1			*Pond 1(2)*			*Pond 2*			*Pond 3*		
	MSE	**MAE**	**r**	**MSE**	**MAE**	**r**	**MSE**	**MAE**	**r**	**MSE**	**MAE**	**r**
Horton	0.4	0.5	0.96	5.6	1.7	0.96	0.1	0.2	0.99	134	9	0.99
Philip	2.4	1.3	0.81	5.8	1.8	0.96	0.1	0.2	0.99	402	16	0.98
Green-Ampt	7.1	1.3	0.77	5.8	1.7	0.98	3.3	1.6	0.99	441	17	0.98

Table 3.3. Hydraulic properties for the best-fit Horton, Philip, and Green and Ampt models.

	Horton			*Philip*		*Green-Ampt*		
	f_o (m/s)	f_c (m/s)	k (hr)	S ($m/s^{1/2}$)	K_s (m/s)	ψ_f (cm)	$\Delta\Theta$	K_s (m/s)
Pond 1	$3\ 10^{-8}$	$2\ 10^{-10}$	$1.4\ 10^{-2}$	$1.1\ 10^{-7}$	$4\ 10^{-10}$	-300	$1.0\ 10^{-1}$	$6\ 10^{-10}$
Pond 1(2)	$1\ 10^{-6}$	$1\ 10^{-8}$	2.3	$5.5\ 10^{-8}$	$1\ 10^{-8}$	-9.6	0.08	$1\ 10^{-8}$
Pond 2	$5\ 10^{-8}$	$8\ 10^{-9}$	$1.7\ 10^{-1}$	$5.0\ 10^{-8}$	$6\ 10^{-9}$	-700	$5.9\ 10^{-3}$	$3\ 10^{-9}$
Pond 3	$1\ 10^{-6}$	$1\ 10^{-8}$	2.3	$5.0\ 10^{-6}$	$2\ 10^{-7}$	$-1\ 10^{3}$	0.1	$4\ 10^{-7}$

Table 3.4. List of ranges for the parameters for the Horton and Philip models for the different goodness of fit criteria as found with the uncertainty analysis for pond 1 and pond 1(2). Units for f_c, f_o, and K are m/s. Units for S are (m/s)^0.5. Units for k is hour. Ranges represent the top 0.1% of the results from the 250,000 Monte-Carlo analysis.

		Horton			Philip	
Pond	Parameter	f_o	f_c	k	S	K
Pond 1	MSE	$2.2\ 10^{-8}$ – $4.3\ 10^{-8}$	$2.8\ 10^{-18}$ - $8.1\ 10^{-10}$	$2.6\ 10^{-9}$ - $6.1\ 10^{-9}$	$1.1\ 10^{-7}$ - $1.1\ 10^{-7}$	$3.4\ 10^{-16}$ - $2.2\ 10^{-12}$
	MAE	$2.2\ 10^{-8}$ - $4.3\ 10^{-8}$	$2.8\ 10^{-18}$ - $8.1\ 10^{-10}$	$2.6\ 10^{-9}$ - $6.1\ 10^{-9}$	$1.1\ 10^{-7}$ - $1.1\ 10^{-7}$	$3.4\ 10^{-18}$ - $2.2\ 10^{-12}$
	r	$2.9\ 10^{-9}$ - $2.8\ 10^{-7}$	$2.8\ 10^{-18}$ - $7.1\ 10^{-16}$	$2.6\ 10^{-7}$ - $2.8\ 10^{-7}$	$2.8\ 10^{-9}$ - $5.0\ 10^{-9}$	$1.5\ 10^{-8}$ - $2.8\ 10^{-8}$
Pond 1(2)	MSE	$1.2\ 10^{-8}$ - $2.6\ 10^{-5}$	$2.8\ 10^{-17}$ - $1.2\ 10^{-8}$	$2.5\ 10^{-11}$ - $5.8\ 10^{-5}$	$8.7\ 10^{-9}$ - $5.9\ 10^{-8}$	$3.1\ 10^{-9}$ - $4.6\ 10^{-9}$
	MAE	$1.2\ 10^{-8}$ - $2.6\ 10^{-5}$	$2.8\ 10^{-17}$ - $1.2\ 10^{-8}$	$2.5\ 10^{-11}$ - $5.8\ 10^{-5}$	$8.7\ 10^{-9}$ - $5.9\ 10^{-8}$	$3.1\ 10^{-9}$ - $4.6\ 10^{-9}$
	r	$2.5\ 10^{-6}$ - $2.8\ 10^{-5}$	$2.8\ 10^{-17}$ - $1.2\ 10^{-16}$	$8.0\ 10^{-7}$ - $6.1\ 10^{-6}$	$1.8\ 10^{-6}$ - $2.8\ 10^{-6}$	$2.8\ 10^{-11}$ - $4.3\ 10^{-11}$
Pond 2	MSE	$1.1\ 10^{-8}$ - $2.3\ 10^{-3}$	$3.6\ 10^{-17}$ - $1.0\ 10^{-8}$	$2.7\ 10^{-10}$ - $2.5\ 10^{-3}$	$7.5\ 10^{-9}$ - $2.2\ 10^{-8}$	$3.3\ 10^{-10}$ - $6.7\ 10^{-10}$
	MAE	$1.1\ 10^{-8}$ - $2.3\ 10^{-3}$	$3.6\ 10^{-17}$ - $1.0\ 10^{-8}$	$2.7\ 10^{-10}$ - $2.5\ 10^{-3}$	$7.5\ 10^{-9}$ - $2.2\ 10^{-8}$	$3.3\ 10^{-10}$ - $6.7\ 10^{-10}$
	r	$1.6\ 10^{-4}$ - $2.8\ 10^{-3}$	$2.8\ 10^{-17}$ - $5.4\ 10^{-16}$	$4.9\ 10^{-6}$ - $8.3\ 10^{-5}$	$1.8\ 10^{-7}$ - $2.8\ 10^{-7}$	$2.8\ 10^{-13}$ - $4.4\ 10^{-13}$
Pond 3	MSE	$1.2\ 10^{-6}$ - $1.5\ 10^{-6}$	$3.6\ 10^{-18}$ - $1.9\ 10^{-7}$	$3.0\ 10^{-9}$ - $5.4\ 10^{-9}$	$1.4\ 10^{-6}$ - $2.0\ 10^{-6}$	$1.5\ 10^{-9}$ - $1.7\ 10^{-8}$
	MAE	$1.2\ 10^{-6}$ - $2.1\ 10^{-6}$	$3.6\ 10^{-18}$ - $1.9\ 10^{-7}$	$3.0\ 10^{-9}$ - $5.4\ 10^{-9}$	$1.4\ 10^{-6}$ - $2.0\ 10^{-6}$	$1.5\ 10^{-9}$ - $1.7\ 10^{-8}$
	r	$2.8\ 10^{-8}$ - $2.7\ 10^{-5}$	$2.9\ 10^{-18}$ - $2.1\ 10^{-10}$	$2.8\ 10^{-8}$ - $2.8\ 10^{-8}$	$2.8\ 10^{-8}$ - $4.3\ 10^{-8}$	$1.8\ 10^{-7}$ - $2.8\ 10^{-7}$

Table 3.5. Hydraulic conductivities for other studies that examined bedrock conductivity.

Author/Year	Bedrock Type	Hydraulic Conductivity (m/s)
Vepraskas and Williams (1995)	Quartz diorite saprolite	$2.2\ 10^{-7}$- $9.2\ 10^{-7}$
Katsuyama et al. (2005)	Granite	$5.8\ 10^{-6}$
Ohte et al. (1989)	Weathered granite	$4.7\ 10^{-4}$
Katsura et al. (2004)	Granite	$9.7\ 10^{-7}$ - $1.2\ 10^{-6}$
Schulz and White (1999)	Quartz diorite	$1.9\ 10^{-9}$
This study (pond 1)	Fractured quartz diorite	$2.1\ 10^{-10}$-$1.0\ 10^{-8}$
This study (pond 2)	Fractured quartz diorite	$8.4\ 10^{-9}$
This study (pond 3)	Fractured quartz diorite	$1.4\ 10^{-8}$

Table 3.6. Potential bedrock infiltration based on the hydraulic conductivities for all four pond experiments. Results are based on average water table presence for three piezometers within the research hillslope. The piezometers were located at the middle and bottom of the hillslope. Values in parentheses are from rages given in Table 3.4.

Pond	Hydraulic conductivity (m/s)	Bedrock infiltration (% of precipitation)
Pond 1	$2\ 10^{-10}$ ($3\ 10^{-18}$ – $8\ 10^{-10}$)	0.1% (0 - 1%)
Pond 1(2)	$1\ 10^{-8}$ ($3\ 10^{-17}$ - $1\ 10^{-8}$)	6% (0 - 8%)
Pond 2	$8\ 10^{-9}$ ($4\ 10^{-17}$ – $1\ 10^{-8}$)	5% (0 - 6%)
Pond 3	$1\ 10^{-8}$ ($4\ 10^{-18}$– $2\ 10^{-7}$)	9% (0 - 121%)

4: SPATIAL VARIATION IN WATER TABLE FLUCTUATIONS ACROSS A HILLSLOPE

4.1 Introduction

British Columbia's coastal mountains consist of catchments with steep short hillslopes with shallow soils. The majority of the runoff from these catchments originates from the zero to second-order streams (Leopold et al.1964; McGlynn and Seibert 2003). The hydrology is driven by the humid coastal climate, high annual precipitation, and soils with high infiltration capacities that create a shallow groundwater reservoir. On these types of hillslopes, subsurface storm flow is generally of the primary components for runoff generation.

The ability to accurately model runoff from these headwater catchments leads to a better prediction of floods and the management of water resources. The understanding of groundwater response to events at the hillslope scale can illuminate the initiation of landslides and the fate and transport of nutrients or introduced pollutants. Shallow groundwater in these hillslopes and riparian zones determines the water quality and quantity that is important to local ecology (Lerner 2009). "Thus understanding the spatially varying runoff generating mechanisms and their magnitude across the landscape is critical in guiding model development and understanding the link between plot-scale runoff process observations and dynamics witnessed at the catchment outlet" (McGlynn et al. 2004).

McGlynn et al. (2004) examined water table dynamics across a range of watershed scales (scales of 80 ha to first-order catchments) and found that relations between water table dynamics and runoff were consistent throughout the year and over a range of antecedent soil moisture conditions. Lag times increased with increasing catchment scale, which created poorer, more scattered relations between groundwater and streamflow. They concluded from these results that correlation decreased between the riparian zones and discharge as scale increased.

When examining the contribution from smaller catchments to the largest watershed (280 ha), McGlynn and Seibert (2003) found that 35% of all runoff in the largest stream originated from subcatchments <1 ha, while 60% and 85% came from subcatchments <4 ha and <20 ha, respectively. When compartmentalizing local watersheds into hillslope and that riparian zones they found that hillslopes contributed the majority of the respective area, and riparian zone to hillslope zone ratios were skewed towards smaller ratios (0.01 to 0.12). These narrow riparian zones with large hillslope contributing area were important in buffering water and solutes from hillslopes in small catchments. McGlynn and McDonnell (2003) used hydrograph separation to quantify the portions of new and old water, along with contributions from the hillslope and riparian zones. Their results were similar to those of McGlynn and Seibert (2003) and showed that smaller events with drier antecedent conditions consisted mainly of riparian water, while larger storms under wetter conditions consisted of larger portions of hillslope water. Riparian zone buffering occurred primarily during small events,

between events, and during early portions of larger events. Buffering potential was related to the ratio of hillslope runoff to the reservoir size of the riparian zone and flow paths through the riparian zone. Riparian runoff dominated the rising limb of the hydrograph, while hillslope water dominated the falling limb. At peak runoff, the riparian zone contributed the largest portion of runoff, with the hillslope and new water contributions following in relative order. Their research described the importance of distinguishing the riparian zone from the hillslope and the need to better understand the physical nature of each zone in order to model the catchment.

Recent research (Moore and Thompson 1996; Seibert et al. 2003; McGlynn et al. 2004) has examined water table dynamics in small headwater catchments. Moore and Thompson (1996) examined water table fluctuations in piezometers in a British Columbian headwater catchment located in the University of British Columbia Malcolm Knapp Research Forest. Their research found that transient shallow groundwater responses resembled that of the single value storage-runoff relationship that is commonly used in hydrological models. Their findings implied that the groundwater table moved up and down in synchrony with respect to a uniform saturated zone. The TOPMODEL equations (Beven and Kirkby 1979) were used to test the relations between piezometers. Results showed few differences between the model and the observed relations. The differences between the model and observations were explained to be the result of preferential pathways and therefore unsteady flow. While they found a single value storage-runoff relationship was appropriate for their research site, they

acknowledged that a two component model may be more appropriate because all of their piezometers were located in a concave hillslope and did not represent the hillslope as a whole.

Seibert et al. (2003) did similar work to that of Moore and Thompson (1996) by examining the relations between piezometric and stream data and testing the steady-state hypothesis used in TOPMODEL. They concluded that a single value storage-runoff model, like TOPMODEL, would not accurately depict the processes within their Swedish catchment because of the differences in water table dynamics in the hillslope and riparian zones. Seibert et al. (2003) found strong correlations between riparian water tables and runoff and strong interwell correlations in the upper hillslope, which suggests that distinct water table zones exist. They argued that a two-box model approach would be more accurate in describing the two zones.

These previous studies were conducted on a planar 5-10% slope and on a concave hillslope with a steeper slope (~25%) by Seibert et al. (2003) and Moore and Thompson (1996), respectively. Seibert et al. (2003) and Moore and Thompson (1996) had course sampling intervals of hours to days and days to weeks, respectively, which give poor resolution of the responsive water tables. Thus, incorporating high resolution groundwater data into research that examines steep slopes will further illuminate the spatial and temporal variation in water table dynamics.

This study examines water table responses in a short, steep hillslope within a first-order watershed in order to identify the spatial and temporal dynamics of

shallow groundwater fluctuations. The objectives of this research are to: (1) examine the spatial variation in the relations between discharge and piezometric response on the hillslope, (2) examine the seasonal variation in the spatial relationship between discharge and piezometric response, and (3) test the steady state hypothesis of storage-runoff relations. It is hypothesized that the relations between discharge and piezometric response on the riparian and hillslope areas are different.

4.2 Methods and analysis

4.2.1 Methods

4.2.1.1 Piezometers

The hillslope was instrumented with 18 piezometers (Figure 2.3). Each piezometer was augured to refusal and backfilled with soil if necessary. PVC pipe, 37 mm in diameter, was used to construct the piezometers. Each piezometer was screened over the bottom 100 mm, and instrumented with an Odyssey capacitance water level probe with lengths of either 0.5, 1.0, 1.5 m. The piezometers were set at 10 minute recording intervals. Water levels within the hillslope were recorded from 10/20/2008 to 10/20/2009. Piezometers B4 and E2 did not reach bedrock and were not used in any of the analyses. Piezometer E3 was excluded from several analyses because of missing data.

4.2.1.2 Precipitation

The rainfall tipping bucket was located in a clear-cut just north of the watershed. Snowfall occurred from 12/12/2008 to 01/21/2009, but was not

recorded accurately. Data were lost for the 05/20/2009 to 06/05/2009 period leading to another data gap. Data from the University of British Columbia Malcolm Knapp Research Forest administration station (http://www.climate.weatheroffice.ec.gc.ca/climateData/canada_e.html) were used to display inaccurate or lost data because of its close proximity to the research watershed. The lack of a discharge response from approximately December 2008 to February 2009 was due to snowfall and snow accumulation in the forest. Total precipitation during the study period was 1493 mm. The total amount of snow (snow depth) was 104 cm (http://www.climate.weatheroffice.ec.gc.ca/climateData/canada_e.html).

4.2.1.3 Soil moisture

Soil moisture was measured within the hillslope with ECH_2O probes (Decagon Devices Inc.) at two depths (25 and 44 cm below the surface; see Figure A5, appendix 3 for map). Data were collected at five minute intervals for the entire study period, except for a data gap between 2/20/2009 and 4/17/2009.

4.2.1.4 Streamflow

Stream stage below the hillslope was recorded with an Odyssey water level recorder set at 10 minute recording intervals. Discharge was measured using the dilution gauging method. Since chloride can be considered to be conservative and background conductivities were low, equation 4.2.1 was used to calculate the discharge:

$$Q = \frac{M}{\int_0^\infty \left[C_d(t) - C_b \right] dt} \quad (4.1.1)$$

Where Q is discharge (l /s), M is the mass of NaCl (g) of the tracer used, C_b is the background concentration of the stream water, t is time (s), and $C_d(t)$ is the concentration measured downstream as a function of time. A YSI 6920 v2 probe was used to measure the conductivity at 5 second intervals. The recorded conductivities were converted to NaCl concentrations using a relationship between conductivity and salt concentration determined in the lab. Different relations were used for different background conductivity values. The coefficient of determination of these relations were all 0.99.

The stage-discharge relationship (appendix 1) was used to convert the stage data into discharge throughout the experiment. The natural log of the discharge was related to the stage, and linear relations between ln(discharge) and stage were computed.

The streambed changed between November and December, 2008 resulting in a different stage-discharge relationship at high discharges. To account for this, two separate stage-discharge relations were used before and after the large storm (53 mm) on 11/12/2008.

Discharge values above 50 l/s are uncertain due to the lack of discharge measurements above 50 l/s. Because of the large uncertainty, discharges larger than 50 l/s were excluded from any analyses.

Confidence intervals (CI) (Figure A2, appendix 1) (95%) were determined using:

$$CI = \bar{x} \pm t(v,z) \cdot \frac{s}{\sqrt{n}} \quad (4.1.2)$$

where x is the distribution of the sample mean, *s* is the sample standard deviation, and *t*(*v,z*) is the t statistic for *v* = *n*-1 degrees of freedom, *z* = 1.96 is the standard normal percentile equivalent, and n is the total nuber of samples. The hyetograph and hydrograph (Figure 4.1; top and bottom, respectively) show how streamflow, and soil moisture at 44 cm below the surface, respond to precipitation events, the responsiveness of the watershed to precipitation, and the quick and short response of streamflow to rain events.

4.2.2 Analyses

4.2.2.1 Spearman rank correlation coefficient

The Spearman rank correlation coefficient is a non-parametric statistical method which was used to determine the correlation between water table levels and stream discharge:

$$r_s = \frac{6\sum D^2}{N\left(N^2-1\right)} \quad (4.1.3)$$

where D is the difference between the rank of discharge and the rank of water table level at a specific time and N is the number of observations. Similar to the Pearson correlation coefficient, the Spearman rank correlation coefficient measures how well two parameters co-vary. The difference between the two is

that the non-parametric approach assumes no specific function (Seibert et al., 2003). For the seasonal analyses the seasons were identified as fall (October-November 2008), winter (December 2008-Febuary 2009), spring (March-May 2009), and summer (June-September 2009).

To test the exponential decline in hydraulic conductivity with depth below the soil surface assumption used in many hydrologic models, the Pearson correlation coefficient for a logarithmic relationship between streamflow and water level (equation 4.2.5) was calculated:

$$z = a * \ln(Q) + b \qquad (4.1.4)$$

where z is the water table elevation (m), *a* is a parameter that describes how quickly the hydraulic conductivity decreases with depth below the soil surface (m/s), Q is discharge (l/s), and *b* is the water table elevation (m) when there is no discharge.

4.2.2.2 Lag time analysis and optimization

Two different lag times were used to evaluate the stream and groundwater responses. The first was the lag-to-start, which was calculated as the time between the start of the stream response and the start of the water table response. The second lag time was the lag-to-peak, which was calculated as the time difference between peak discharge and peak water table. A positive lag time means that the groundwater response occurred after the stream response. A negative lag time means that groundwater responded before the stream response.

Lag optimization of the Spearman rank correlation between water table levels and discharge was also calculated. The result of the optimization produced the highest possible Spearman rank coefficient and the corresponding lag time within the range of -72 to 24 hours. This range of lag times was chosen to reflect the response of the water table to events while preventing the analysis from being influenced by post or prior events. The Matlab© code for this optimization can be found in appendix 2.

4.2.2.3 Water table percentage and connectivity

The percentage of time that a water table was observed, was calculated using one year of water table data (from 10/20/2008 to 10/20/2009) and determining the number of observations for which a water table greater than 0.07 m (the water level recorder's lower measurement limit) was measured. The number of observations with a measurable water level was divided by the total number of observations. The degree of connectivity of the hillslope and riparian zone can be inferred from the percentage of time that water tables were observed in both zones.

4.3 Results and interpretation

4.3.1 Spatial variation in water table presence and response

The near-stream (riparian) zone (0-8 m) showed a negative linear relation between the fraction of time that a measurable water table was present and upslope distance, and the fraction was low and variable for the locations >8 m upslope (Figure 4.2). The Spearman rank correlation coefficient and the Pearson

(linear) correlation coefficient between upslope distance and the fractions of time with measurable water tables were 0.83 for both. The scatter for the hillslope locations (>8 m upslope) suggests that water table persistence was not a function of slope position at the hillslope scale. The Spearman rank correlation coefficient of the relationship between topographic wetness index (chapter 2, Figure 2.3) and water table persistence was 0.1, which suggested that surface topography had little influence on water table dynamics.

Riparian and hillslope zones were divided into groups of piezometers containing transects A and B (riparian) and C, D, and E (hillslope). The average of the average, standard deviation, and range of water table heights for each piezometer for the period of observation were 0.06, 0.01, and 0.1 meters above bedrock, respectively, for the hillslope zone. The average of the average, standard deviation, and range of water table heights in the riparian zone were 0.11, 0.06, and 0.33 meters above bedrock, respectively. The average ($p=0.01$), range ($p=0.001$), and standard deviation ($p=0.004$) were all significantly different between the hillslope and riparian area (determined using a two-tailed t-test). The significant difference in the ranges illuminates the difference in water table response magnitudes in the two zones. The division between the riparian and hillslope zones was further investigated with a hierarchical cluster analysis using the average, range, standard deviation of the water table, and water table persistence for 7 months of data from October 2008 to May 2009. The results were described with a dendrogram (Figure 4.3), which shows a clear division between riparian and hillslope piezometers. Piezometers A1 and B1 were

exceptions. The aforementioned statistics, along with figures 4.2 and 4.3, clearly show that there are two distinct water table zones.

Interwell correlations were determined to gain a better understanding of the dynamics of the transient water table responses (Figure 4.4). Riparian zone wells (rows A and B) showed strong correlations with each other. Correlations between riparian and hillslope piezometers became worse as the distance between the piezometers increased. Correlations between piezometers on the same row were strong and there were linear relations between piezometers A3 and A4. This implies that the piezometers on the same rows respond in unison. Row C had the poorest relations, followed by row D. Some of the correlations (e.g. A3 and D2; B3 and D3) showed threshold relations. The threshold that appeared for riparian and hillslope piezometers indicates that hillslope piezometers only respond after riparian piezometers have elevated water tables. These relations imply that the water table on this hillslope moves from the riparian zone to the hillslope in a saturated wedge like fashion, as described by Weyman (1973). The transect of piezometers A3, B3, C3, and D3 showed the highest degree of connectivity through the year (Figure 4.2 and Figure 4.4).

4.3.1.1 Spearman rank analysis

For piezometers within 8 m of the stream the Spearman rank correlation coefficient for the relation between groundwater level and discharge ranged between 0.6 and 0.9 (Figure 4.5). For piezometers more than 8 meters upslope the Spearman rank coefficients decreased with upslope distance (Figure 4.5). Piezometer A1 seems to be an outlier to this relationship, which can be attributed

to hysteretic relations between streamflow and groundwater. The Pearson (linear) correlation coefficient between Spearman rank coefficient and uphill distance was -0.74, excluding piezometer A1. The Pearson (linear) correlation coefficient between Spearman rank correlation coefficients (for the relationship between groundwater and streamflow) and the wetness index was 0.28.

Piezometers closest to the stream had the strongest relations with discharge (Figure 4.6). Piezometers A2, A3, A4, B2, B3, B4, C2, C3, and C4 had a lognormal relationship with discharge in fall 2008 (Figure 4.6). Piezometers E3, D2, C1 and A1 showed small responses when discharge increased. The water table did not reach the soil surface during the time of observation at any of the piezometers. Piezometer B3 showed the largest water table responses during fall, with water table heights as high as 0.4 m above bedrock. Piezometers A1 and B1 had a very scattered relationship with discharge. The Pearson correlation coefficient for the logarithmic relationship between streamflow and discharge appeared to be a threshold function of distance uphill during the fall: it was high for piezometers located <8 m upslope and low for piezometers located > 8m upslope (Figure 4.7). It was low for all piezometers in summer (Figure 4.7).

Piezometers A2-4 and B2-4 all had a constant (maximum) water level at high discharge. Transect A, closest to the stream, showed a hydrologically limited response and constraints at water table heights of 0.26, 0.29, and 0.38 m above bedrock for piezometers A2, A3, and A4, respectively. Transect B showed constraints at 0.36, 0.40, and 0.28 m for piezometers B2, B3, and B4,

respectively. The mean constraint was 0.33±0.06 meters above bedrock (Figure 4.6).

4.3.2 Seasonal variation in the relation between water level and discharge

The data for the piezometers A3, B3, and C3 were divided into seasons to further test the existing relationship between water table and streamflow response. These results showed that the strongest relationship existed during the fall and spring, while the relations for winter were more scattered (Figure 4.8). Heavy snowfall and snow accumulation occurred during the winter season, causing poorer correlations between water level response and streamflow. Piezometer C3 had little response during the year with a small response occurring only in the winter. Summer correlations were only clear for piezometer A3.

For fall, winter, and spring seasons the Spearman rank correlation coefficient for the relationship between streamflow and groundwater response decreased as distance uphill increased (Figure 4.9), similar to the results for the entire year (Figure 4.5). A decrease in correlation between discharge and groundwater level and increased scatter in the correlation occurred for piezometers more than 8 m uphill. Piezometer A1 had very low or negative correlations for all seasons. The summer season had the largest scatter and a positive trend with uphill distance. This can be explained by piezometers in the riparian zone responding to summer events, but at a different time than streamflow, which resulted in poor correlation coefficients. Piezometers further uphill did not respond, creating a dampened effect and stronger correlations for the hillslope piezometers. The histogram of

the Spearman rank correlation coefficients for the four seasons showed that fall had the greatest frequency of high correlation coefficients between water table height and streamflow, with spring, winter, and summer following in respective order (Figure 4.10).

4.3.3 Lag analysis and optimization

Piezometer responses were analyzed for lag-to-peak (Figure 4.11) and lag-to-start (Figure 4.12) times for rainfall events between 10/17/2008 to 5/13/2009. Negative lag times mean that the piezometers responded before discharge. There was a large variation in the lag-to-peak results. Timing and uphill trends varied significantly for storms without a clear spatial pattern. Lag time-to-start (Figure 4.12) showed a clearer pattern than that of lag-to-peak (Figure 4.11). The lag-to-start analysis showed an increase in variation and increase in lag time with increased distance uphill. This suggests that the time to start of a response (Figure 4.12) is controlled more by distance uphill and the time to peak discharge (Figure 4.11) is perhaps controlled more by the dynamics of the mechanisms controlling hillslope runoff.

To further examine lag time influences on runoff the Spearman rank coefficient for the relationship between streamflow and groundwater level was optimized by varying lag times for the fall (October-November 2008). Optimized lag times ranged from negative -2 to 22 hours. A low Spearman rank coefficient was found for piezometers more than 8 m uphill. Stronger correlations occurred when piezometers responded before discharge (negative lag times; black circles in Figure 4.13). Hillslope piezometers (>8 m uphill) were found to have optimized

lag times that were positive (white circles in Figure 4.13), meaning that discharge responded before the water table. Piezometer A1 was an exception in that it had a high Spearman rank coefficient with a positive lag time. The Spearman rank correlation coefficient for the relationship between lag optimized Spearman rank coefficients and distance upslope was 0.51 (Figure 4.13).

4.3.4 Timing of water table response to rainfall

Piezometers A3, B3, C3, and D3 represent a transect through the center of the hillslope from near-stream to almost the top of the hillslope. During two storms in November and December (Figure 4.14; top left and right, respectively), the only piezometers to respond were A3, B3, and a relatively small response from C3. This suggests that the riparian zone and the lower central area of the hillslope were connected and contributed to runoff. However, transient water tables lower than 0.07m above the soil-bedrock interface may also have existed further upslope.

The November, 2008 and May, 2008 storms show that the transient water tables responded after discharge (Figure 4.14; top and bottom left, respectively). In both cases, piezometer A3 responded more quickly than piezometer B3. The response of piezometer B3 had a greater magnitude and a shorter duration than that of piezometer A3. For the storms occurring in early December, 2008 and early August, 2009 (Figure 4.14; top and bottom right, respectively), piezometers responded synchronously with discharge. The response of piezometer B3 had a greater magnitude than that of A3, but A3 had a longer duration for the December storm. For the August storms the only piezometer to respond was A3.

During these storms the falling limb of piezometer A3 responded in parallel to the falling limb of runoff, suggesting that the near stream riparian zone supported the recession of runoff and baseflow. The response of piezometer B3 coincided with the duration of peak runoff, suggesting that contributions from the whole riparian zone influenced the magnitude and duration of the runoff event. Piezometer response on both the A and B rows reflect the shape of the hydrograph, with rows A and B contributing to the hydrograph peaks and row A contributing to the recession of the hydrograph.

The largest differences between soil moisture responses at 44 and 25cm below the surface occurred for the December and August storms. The two storms had similar streamflow responses to different precipitation inputs, showing the influence of storage and antecedent moisture conditions. This is supported by the large response of soil moisture in August and a small response for the December storm. The November and May storms had similar precipitation inputs with different streamflow responses. Initial soil moisture for these storms was relatively high. The difference between these storms is the timing of response of soil moisture at 44 cm below the surface and the concomitant response of streamflow. This suggests that streamflow response is related to soil moisture at depth.

4.4 Discussion

4.4.1 Spatial variation in lag times of groundwater response

This research has shown that water table dynamics at the hillslope scale vary both spatially and temporally. Upslope water tables (perched) were only present during a short period of the year. The lag time between discharge and water table response in the upslope hillslope area was significantly different than that of the riparian area. Lag times and variation in lag time response were found to increase with distance uphill. The variation in lag times suggests that water tables do not respond in unison to rainfall, which has been shown previously by Fannin et al. (2000) who also examined water table dynamics in Coastal British Columbia.

Increased lag time and variation in lag time could be a function of soil depth (Seibert et al. 2003). In the case of this study, hillslope soil depths are relatively similar (Table 4.1), suggesting that initial soil moisture content (Figure 4.14) and spatially varying preferential flow paths may have a larger influence on lag times. The lag time variation may be caused by the spatial variation in soil moisture (Chin, 2009) or variation in bedrock contributing area (McDonnell et al. 1996). During wetter initial conditions (i.e. late fall, winter, and early spring), or after soil moisture deficits have been fulfilled, spatially varying flow paths would be more influential. During drier initial conditions soil moisture becomes more influential.

Lag time variations between hillslope and riparian zone piezometers, along with hysteretic relations between piezometers within the riparian zone imply the

rejection of the steady-state hypothesis due to the non-uniform rise and fall in water table levels.

The water table in the riparian zone had strong correlations with discharge (except A1 and B1) and high interwell correlations, e.g. piezometers A3 and B3 mimicked discharge (Figure 4.4). Strong correlations, together with the small negative lag times, suggest that riparian zone water was a first order source of runoff. The lack of a measurable lateral water table expanding more than 8 m uphill implies that the vertical expansion of the water table in the riparian zone determines the shape of the hydrographs peak and recession (Figure 4.14). Hysteretic influences on the water table were observed in piezometer A1 and B1, which were located in the riparian zone and responded differently than the other riparian piezometers. The hysteretic behaviour in the riparian zone suggests that differences in timing may be influenced by multiple flow paths and that even in the riparian zone water table dynamics can vary spatially. Positive lag times described a streamflow response before a water table response, implying that different mechanisms or timing in mechanisms may be influencing the initial response of streamflow, as discussed below.

A streamflow response before a water table response may be caused by the clear-cut north of the study watershed or direct precipitation on the stream and wetland areas in the clear-cut. The clear-cut encompasses a large portion of the contributing area on the stream (see appendix 1 for map). These influences include a smaller soil storage capacity due to soil compaction and reductions in evapotranspiration and interception losses, quicker response due to a lack of a

delayed input from the forest canopy, and channel rerouting from road and ditch construction (Moore and Wondzell 2005). All of these are applicable to the study watershed. Chin (2009) found that for the study watershed throughfall was 15% less than rainfall. She also showed that surface moisture content in the clear-cut was higher and responded more quickly than that of the forest. The larger input and quicker response would explain why streamflow responded before the piezometers on the forested study hillslope during some events.

4.4.2 Distinction between water table dynamics in the riparian and hillslope zones

Recent research has described the need to compartmentalize watersheds into hydrologic units that act as catena's (McGlynn and McDonnell 2003a, 2003b; McGlynn and Seibert 2003). This would allow for more process oriented modeling (McDonnell 2003). Common components of a watershed are hillslopes and riparian zones, and in some cases, a separation is made between convex and concave hillslopes.

Hillslope and riparian water table responses correlated well within their respective zones, but a threshold relation in water table responses existed between the zones. Hillslope correlations between a measurable water level response and streamflow decreased substantially at locations more than ~8 m upslope and were poor throughout the year, while correlations were stronger for locations in the riparian zone. The difference in correlations between water level and streamflow, along with the differences in frequency of measurable water tables above the bedrock, suggest that the hillslope at this site can be divided

into two distinct zones; a riparian zone from approximately 0-8 m uphill and a hillslope zone from 8-18 m (approx. the top of the hillslope).

When examining the significance of the boundary at 8 meters uphill, the large step and break in slope that occurs at ~8 m clearly stands out (chapter 2, Figure 2.3). Other explanations could be the elevation above the stream (i.e. less than 2.4 m below the 8 m boundary). Seibert et al. (2003) came to similar conclusions finding that two distinct zones existed from 0-35 m and 35+ m. However, their research did not identify any geomorphic feature as an explanation for the change in water table dynamics more than 35 m away from the stream. The elevation differences at 35 m in their Swedish watershed were similar to that of this research (i.e. less than ~3 m below the 35 m boundary), implying that elevation above the stream could be a constraint on water table dynamics.

This research showed that in steep watersheds the steady state model described by a single value storage-runoff relationship is inapplicable because of the spatial variation in the relations between streamflow and groundwater response. These water table dynamics describe the need for a two or three component system that differentiates the riparian, hillslope, and maybe a zone that explains piezometers A1 and B1. These findings are similar to Seibert et al. (2003) and contradict Moore and Thompson (1996) in that a single-valued storage-discharge model based on steady state conditions is inappropriate for the prediction of runoff generation. Furthermore, this research concurs with the notion of McDonnell (2003) that the hillslope should be divided into spatially

distinct catenas described by both lateral and vertical non-linear or threshold relations.

4.4.3 Hydrologically limited response in water table dynamics

Fannin et al. (2000) introduced the concept of hydrologically limited and unlimited responses. A hydrologically limited relationship exists when a dependent variable ceases to increase with the independent variable, creating a physical constraint on the controlling process. A hydrologically unlimited relationship occurs when no constraints exist and dependent and independent variables remain coupled.

The hydrologically limited relationship between groundwater and streamflow (Figure 4.6) that occurred in the riparian zone could be attributed to (1) macropore flow through hydrologically connected pipes which increased saturated hydraulic conductivities, (2) throughflow through fractured bedrock, and/or (3) loss of localized flow constraints; (i.e. bedrock microtopography loses control) (Fannin et al. 2000). Field observations have shown that the bedrock is fractured and permeable (chapter 3). Increased water table heights increase pressure head on fractured bedrock, which can increase infiltration into the bedrock. This increased infiltration could contribute to the hydrologic limit. However, bedrock conductivity was very low suggesting that it may not be the main cause of the constraint.

The small variation in the water table heights when the hydrological limitation occurs over a large portion of the riparian zone suggests that the physical

characteristics at the layer above the bedrock (i.e. soil-bedrock interface) controls runoff to the stream until discharge exceeds 25±2.5 l/s. With increasing discharge values, runoff is no longer correlated to water table dynamics. Water levels tend not to rise above 33±6cm above bedrock possibly because of very effective flow through preferential flow paths at this soil layer. Macropores approximately 4 cm in diameter have been observed at the riparian-stream interface at depths of 30-60 cm above bedrock. These macropores were located downhill of piezometers A3 and A4. One macropore was observed to flow on multiple occasions during large precipitation events. These macropore flow paths can result in quick drainage and can explain the maximum groundwater level at high discharge. Large woody debris and roots are present in the soil and vertical preferential flow along these roots occurs (Cheng 2007). Preferential flow pathways are expected to exist in all areas of the hillslope and riparian zones, and for this reason the second explanation for hydrologically limited responses is applicable. Piezometer depths in relation to soil topography suggest that the bedrock topography is relatively similar to the surface topography and therefore relatively planar. However, the spatial resolution of the bedrock topography is poor and needs to be further investigated. Therefore, the localized flow constraints as explained by Fannin et al. (2009) may still hold as well.

The hydrologically limited relations between water table levels and discharge lead to concerns about the accuracy of models that use water levels to predict discharge. As seen in the correlations between riparian water tables and stream discharge, (almost) no change in water table height occurs with substantial

changes in discharge. The prediction of high discharges in such models therefore becomes highly uncertain. These accompanying inaccuracies warrant concerns when using storage-discharge models in locations where hydrological limitations are present.

4.4.4 Implications for runoff generation mechanisms at the hillslope scale

The pathway that precipitation takes to the stream is difficult to determine. When the dominant flow pathway in the hillslope zone is at the soil-bedrock interface, transient water table dynamics have been shown to be controlled by bedrock microtopography (Tromp-van Meerveld and McDonnell 2006) and the lateral saturated hydraulic conductivity (Peters et al. 1995). Recent research has suggested that different pathways may also exist. Infiltration into permeable fractured bedrock in upslope areas and the transmittance to the riparian zones where the groundwater exfiltrates back into the soil, has been suggested as one of these alternative pathways (Katsuyama et al. 2009). The permeability of the bedrock below the upper hillslope zone would explain the absence of a water table in the soil zone in between events and exfiltration into the riparian zone could partially explain the water table's persistence.

Research on the study hillslope has shown that the saturated hydraulic conductivity decreases exponentially with depth and is several orders of magnitude larger than the saturated hydraulic conductivity of the fractured bedrock (10^{-5} m/s and 10^{-8} m/s for soil at the soil-bedrock interface and fractured bedrock, respectively) (chapter 3). Field observations have shown a high frequency of tree roots growing over the soil-bedrock interface and into fractured

bedrock, suggesting that lateral preferential flow paths exist at the soil-bedrock interface (chapter 2, Figure 2.4).

The connectivity of the hillslope zone to the riparian zone was sporadic and present only during large events. The lack of an established hillslope water table may be influenced by bedrock infiltration or bedrock microtopography, or it may be so shallow (<0.07m) that it could not be measured. Water levels in piezometers show that the connectivity of the hillslope and the riparian zones is characterized by a threshold relationship and occurs only during large events. The differences in lag times for hillslope and riparian zones (i.e. increased variance and lag time with increased distance uphill, and a negative riparian vs. positive hillslope lagtime) suggests that the water table expands from the riparian zone into the hillslope zone. The threshold relations between the water table responses in the riparian and hillslope zones, and the relation between water level persistence and upslope distance, also imply that the water table expands from the stream to uphill areas up to about 8 m uphill from the stream. This upslope water table expansion is similar to the saturated wedge concept described by Weyman (1973). As the water table expands, it rises into more macroporous soils, resulting in preferential flow and the observed hydrologically limited response. The expansion of this saturated wedge is determined by the storm size, antecedent moisture conditions, and topography.

The hydrologically limited response suggests that preferential flow occurs at higher water table levels and therefore during larger storms and high soil moisture content. As the water table in the riparian zone rises, preferential flow

paths increase in connection and in activation (both vertically and laterally), similar to that described by Negishi et al. (2007) and Sidle et al. (2001). Their research found that a spatially heterogeneous pipe flow network controlled vertical and lateral transport of precipitation from the surface to the stream. Pipe flow provided dominant drainage of subsurface storm flow above the soil-saprolite interface and depended on precipitation event size. Deeper pipes were initiated first, followed by progressively shallower pipes. Larger storm events were needed to initiate pipes that were in higher soil locations. These higher pipes contributed a large proportion of pipe flow.

The strong correlation between riparian water tables and streamflow, along with its persistence suggests that the riparian zone dynamics control runoff generation. The poor correlation between the hillslope water tables and streamflow also suggests that the soil zone of the hillslope contributes little to streamflow during most events. This is similar to the results from the Panola Hillslope in Georgia (Tromp-van Meerveld and McDonnell 2006). Jensco et al. (2009) related upslope accumulated area (UAA) to water table presence for a wide range of catchments. Their research showed that small UAA resulted in no or transient water table connection between hillslope-riparian-stream (HRS) networks and that those water tables were only connected during peak snowmelt or large rain events. The connectivity increased with UAA. The increased connectivity of hillslopes accounted for the majority of runoff during events and exemplified the importance of connectivity between the hillslope, riparian zone, and the stream for runoff generation at the hillslope scale. The lack of hillslope

water table persistence and correlation with the riparian zone, along with shallow depth of the water tables, suggest that the connectivity of the hillslope is very limited and of little significance to runoff generation for most events, except for the large events.

McGlynn and McDonnell (2003) used hydrograph separation, coupled with chemical tracers, to model and dissever three contributing sources; old, new, and hillslope water. Their results show that riparian water responded first, then new water, and the last was the hillslope. The rising limb of hydrograph was dominated by riparian water, while the falling limb was dominated by hillslope water. The identification of sources by hydrochemical signals (Negishi et al. 2007; McGlynn and McDonnell 2003b) may help explain the physical processes described in this study. Similarities in the watershed under investigation and watersheds in the previous studies exist: both have highly macroporous soils and are located in humid climates. Historically, the inference of process similarities between watersheds has been difficult and has led to pseudo-assumptions. Because of this, further work in the research watershed using hydrogeochemical characteristics of streamflow, soil water, bedrock water, and rainfall are needed to identify contributing sources.

4.5 Conclusion

Hydrometric and piezometric data were collected for one year to determine the spatial and temporal relations between storage and runoff. Interwell, groundwater-discharge relations, and lag times were examined to better understand runoff generation mechanisms and to test the steady state

hypothesis of local storage-runoff relations. It is hypothesized that as soil moistures increases, transient water tables in the hillslope develop, and water moves laterally at the soil-bedrock interface. This contributes to the riparian zone expansion from the riparian zone uphill (like a saturated wedge), with the majority of the water table being contained in the riparian zone and spatially controlled by the hillslope's break in slope at 8 m. Hillslope water may move to the stream via both preferential flow paths and through fractured bedrock, resulting in significantly different response times. Throughflow in the riparian zone moves to the stream via matrix flow and preferential flow paths, with the latter likely increasing in contribution as the water table increases in height.

This research has shown that:

1. Two distinct zones exist on the hillslope: the riparian zone (0 to ~8 m) and the hillslope zone (>8 m from the stream). The riparian zone is separated from the hillslope by a steep narrow slope at ~8 meters.
2. The short duration of a measurable water table presence in the hillslope zone suggests little or no connectivity of the hillslope and the stream during most of the year. The spatially variable presence of groundwater in the hillslope zone implies that the transient water table does not respond uniformly and may be controlled by soil moisture and infiltration patterns, along with bedrock microtopgraphy.
3. The steady state hypothesis of a single value storage-discharge relationship does not apply because of non-uniform water table fluctuations in both zones.
4. Pipe flow in the riparian zone is likely responsible for the hydrologically limited effect on storage-discharge relations.
5. Lag times and variation in lag times increase with increased distances uphill. Streamflow responds before hillslope water tables respond and

sometimes also before riparian water tables respond. This may be caused by quicker runoff production from the clear-cut north of the study watershed or precipitation directly on the stream or the wetland area in the clear-cut.

6. Seasonal variations in storage-discharge relations show that soil moisture and storage influences response timing and source areas.
7. Water table fluctuations and interwell threshold relations show that the water table expands from near-stream areas uphill, similar to the theory of the saturated wedge.

This research has shown the spatial and temporal variation that occurs in water table dynamics. This variation can have significant implications for model design, accuracy and applicability.

4.6 Figures

Figure 4.1. Hyeotograph and hydrograph for the study period. Discharge values above 50 l/s are uncertain due to the lack of discharge measurements above 50 l/s. The arrow denotes the area of missing rainfall data from the MKRF gauge. The arrows with vertical lines indicate periods when the rain gauge was frozen.

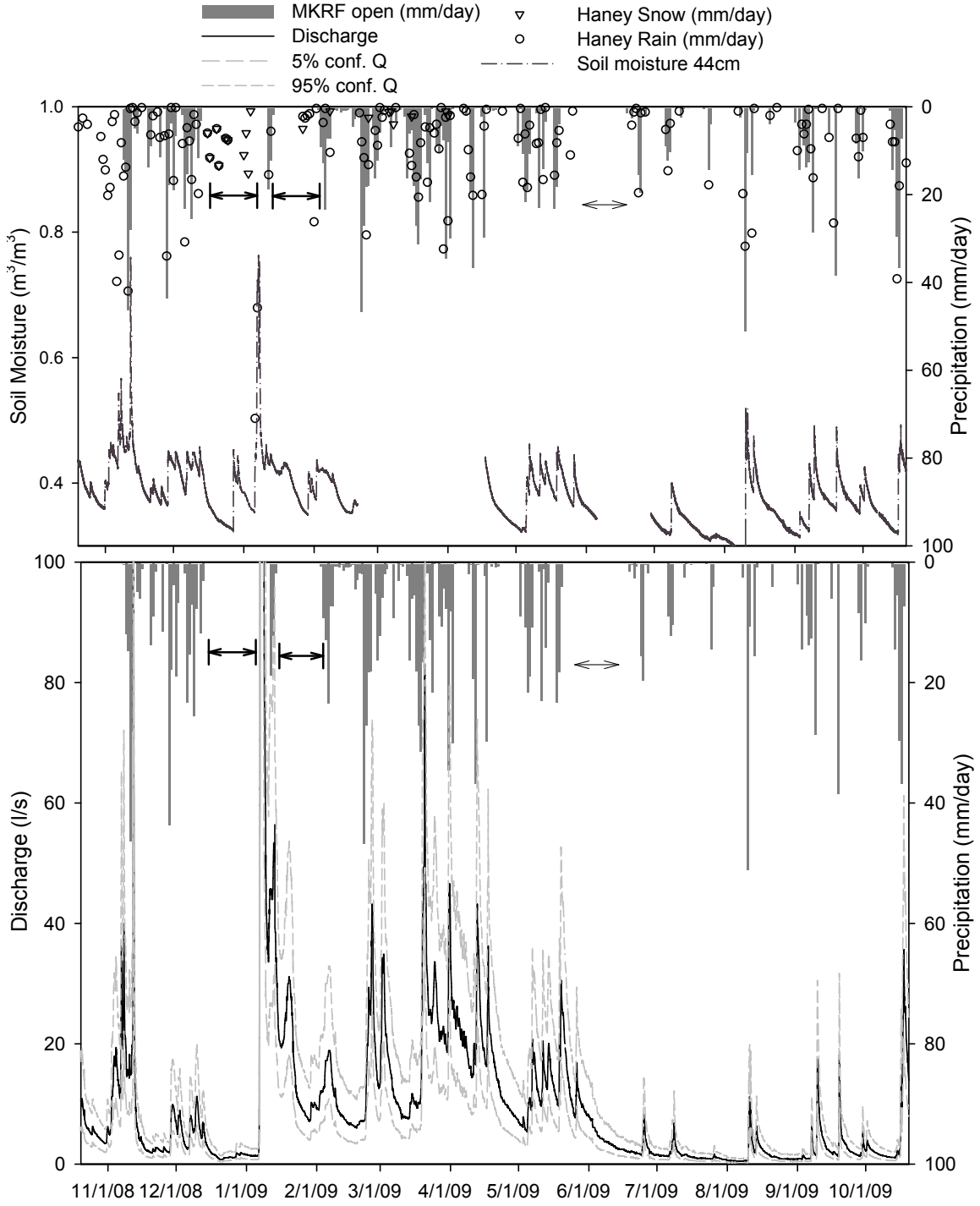

Figure 4.2. Fraction of time a measurable water table (>0.07m) was present during the period of 10/20/08 to 10/20/09 as a function of distance uphill.

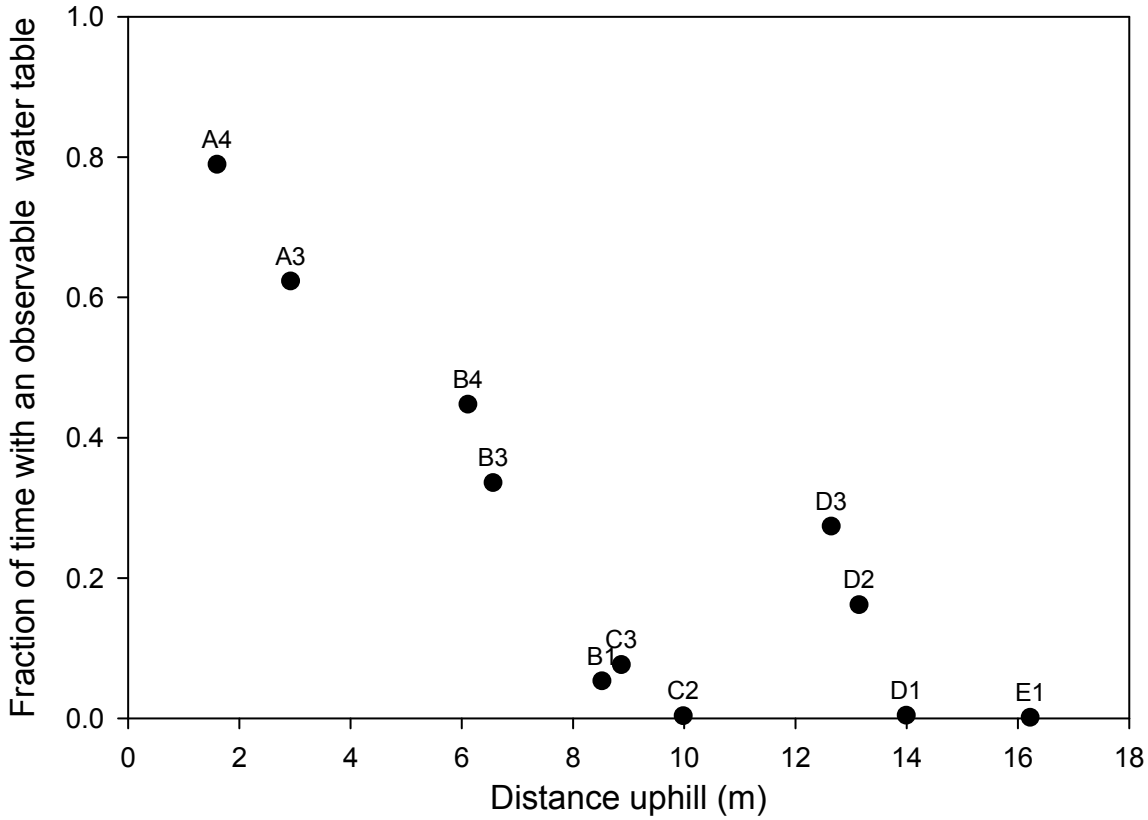

Figure 4.3. Dendrogram of the hierarchical cluster analysis based on the average, standard deviation, and range of the water table above bedrock, and percent of time with water table presence.

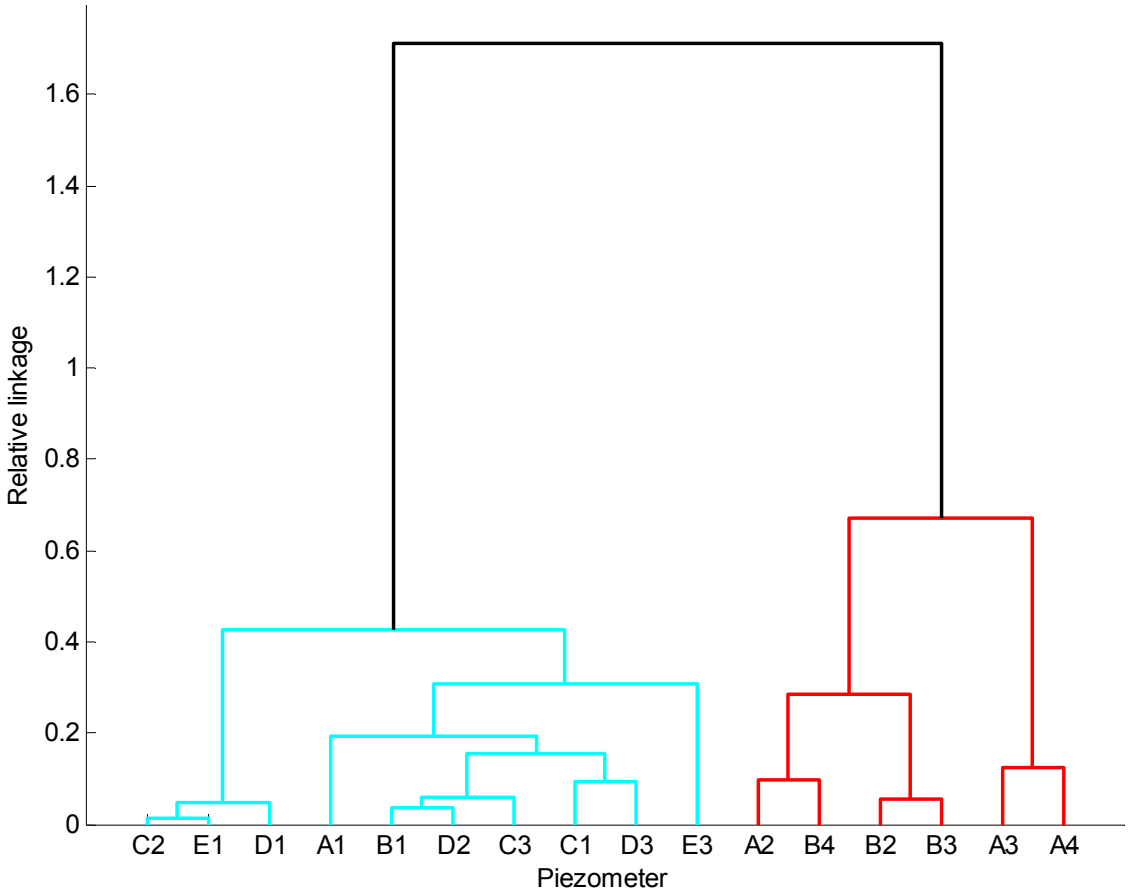

Figure 4.4. Correlations between piezometers. The number in the top of each graph represents the Spearman rank correlation coefficient. For the location of the piezometers see Figure 2.3 in chapter 2.

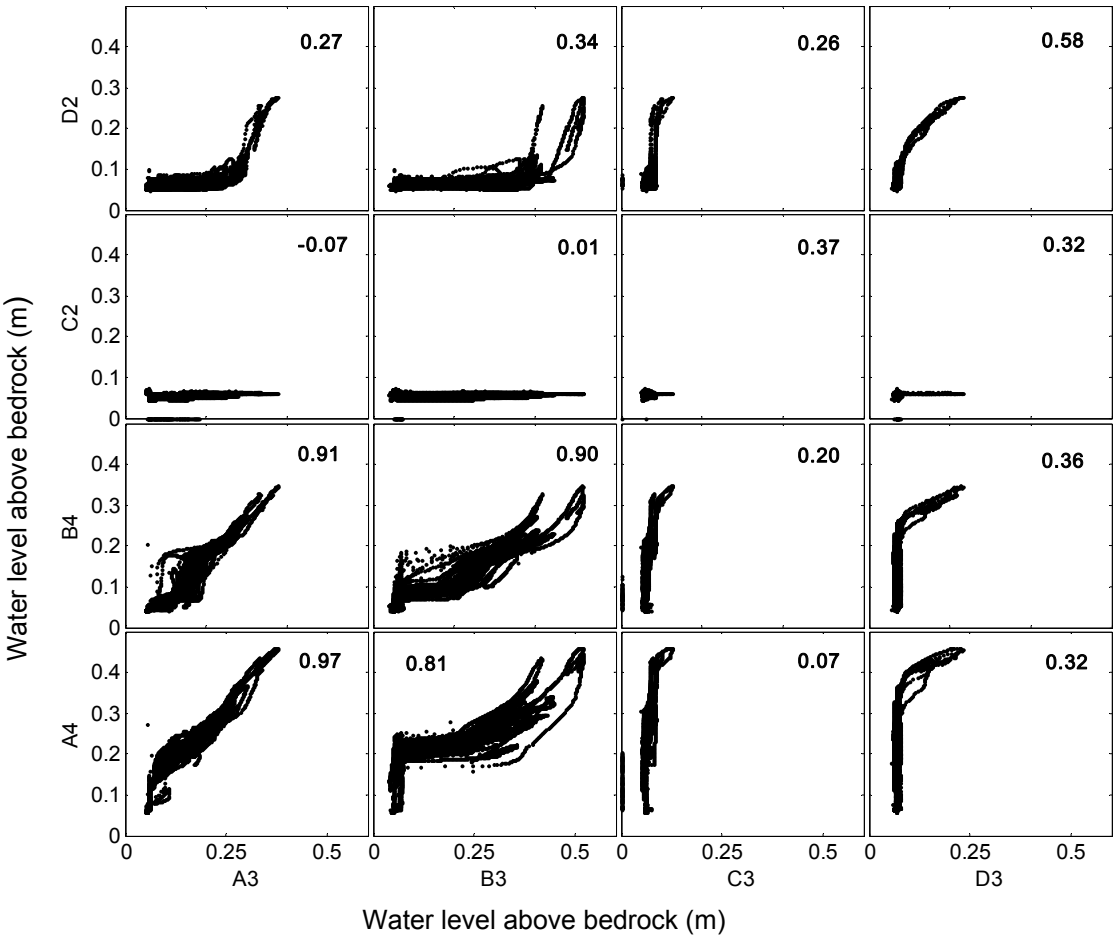

Figure 4.5. **Relation between the Spearman rank correlation coefficient for the relation between discharge and water table response and distance uphill for the whole study period (10/20/2008 to 10/20/2009). Outer bars represent the histogram of the distribution of points. Note the outlier (site A1) and the decline in correlation for points located more than 8 meters uphill (denoted by dashed line).**

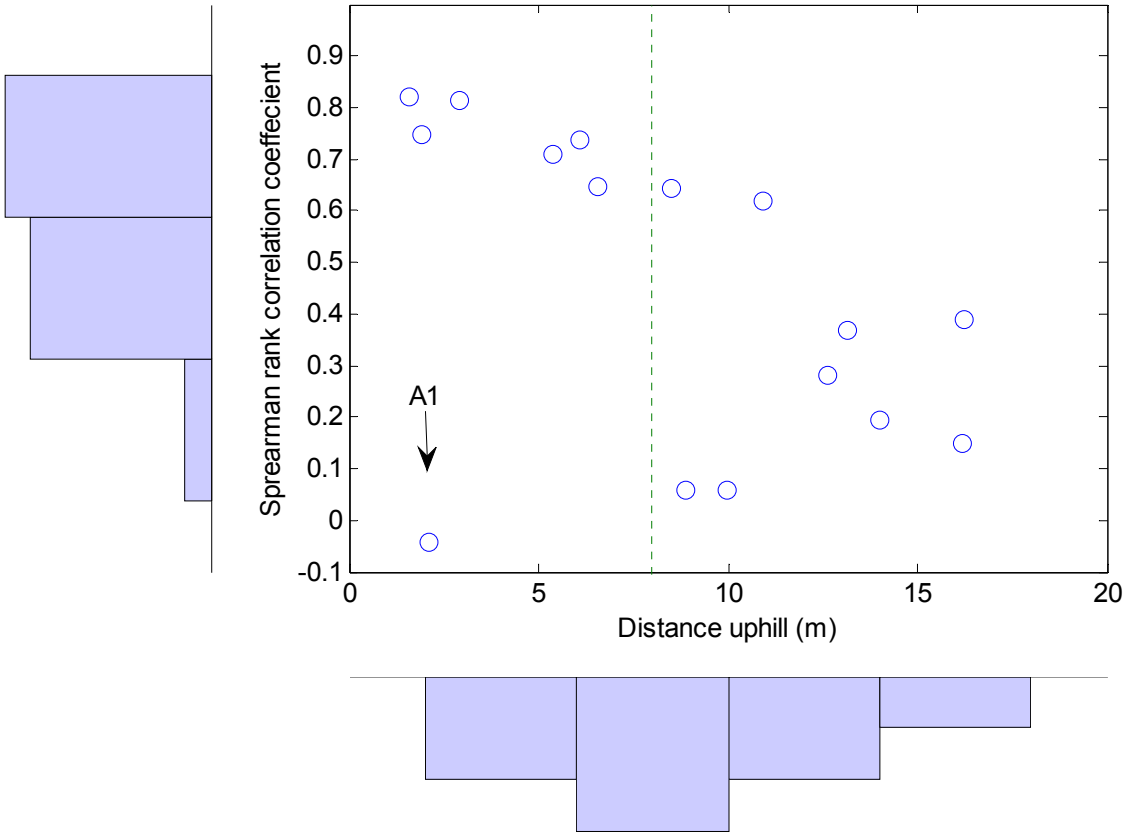

Figure 4.6. Relationship between piezometer groundwater level and discharge for fall 2008 (September-November). Location of the subfigures relates to the location of the piezometers on the hillslope (Figure 2.3, chapter 2). Piezometers on rows A and B represent the riparian zone. Piezometer depth (below the soil surface) and distance uphill are given in Table 4.1.

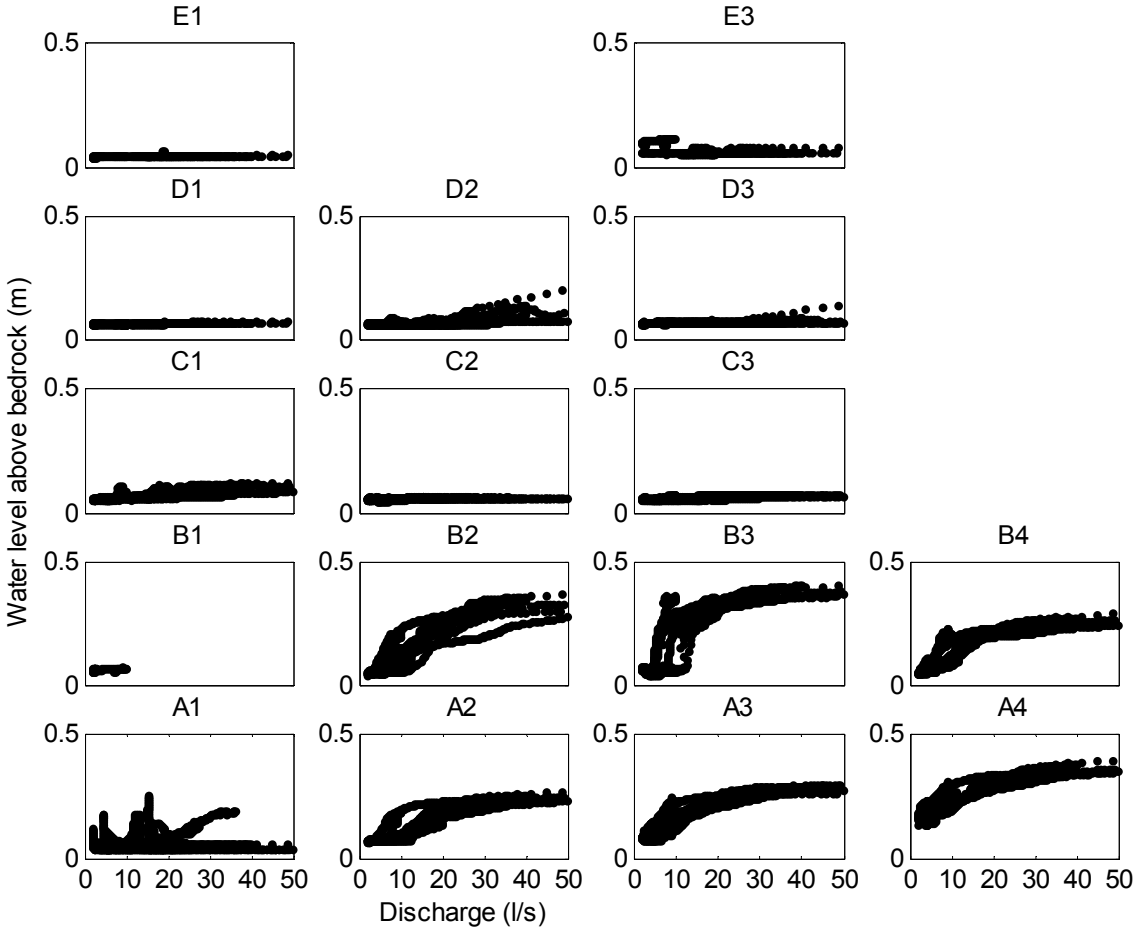

Figure 4.7. Pearson r^2 values of the logarithmic relationship between groundwater and discharge (z= a*ln(Q)+b) as a function of distance uphill. Black squares represent the fall season while open circles represent the summer season.

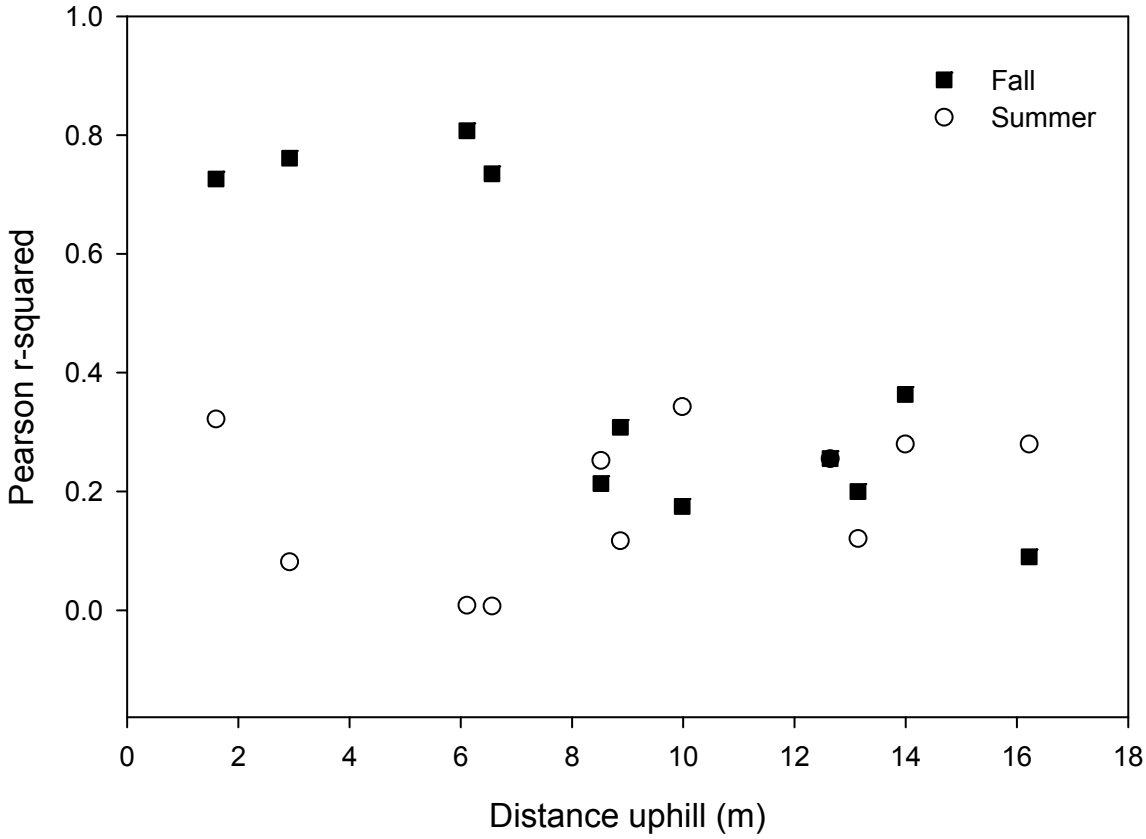

Figure 4.8. Seasonal variation in the relationship between groundwater level and discharge for piezometer A3 (bottom), B3 (middle), C3 (top). This figure shows that the relations are strongest for the fall and spring and become weaker as distance uphill increases. Increased scatter in winter is partially attributed to snow cover and differential melt rates.

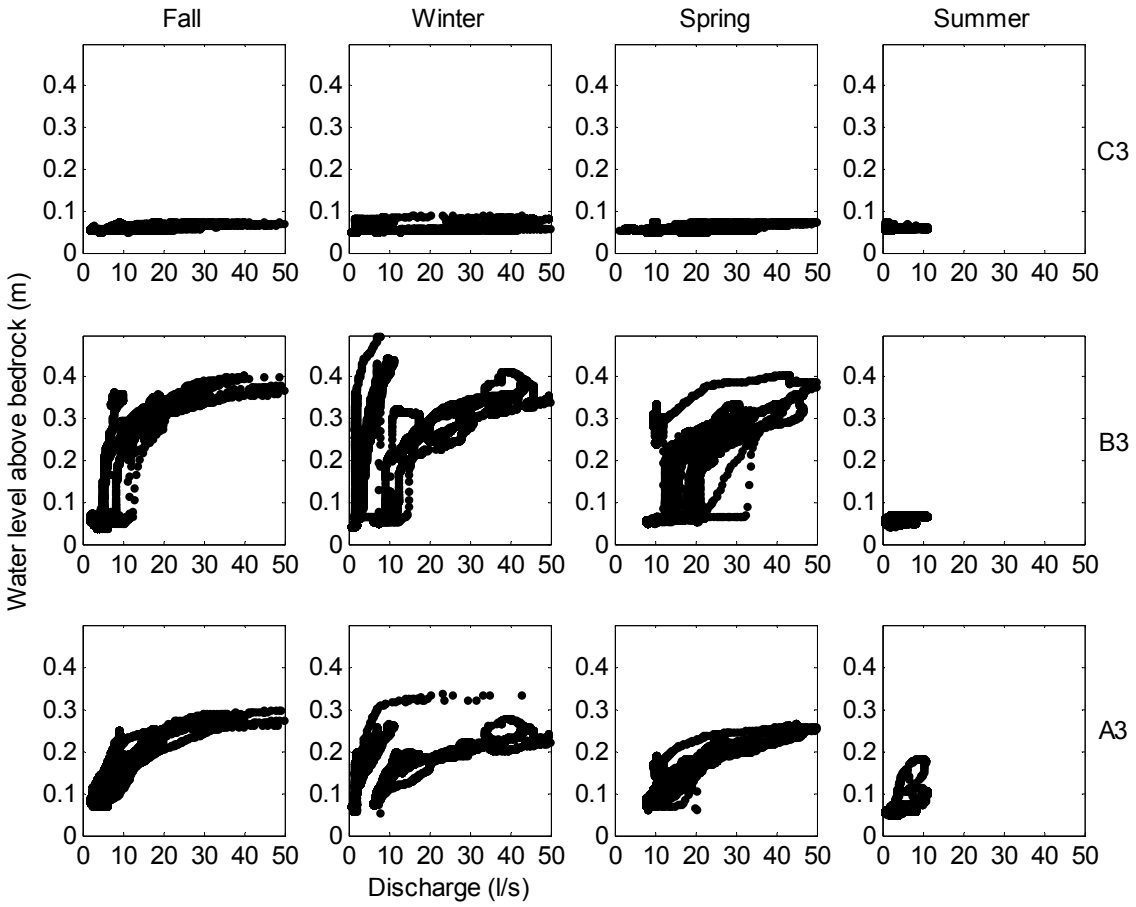

Figure 4.9. Spearman rank correlation coefficient for the relationship between streamflow and water level for the different seasons as a function of upslope distance.

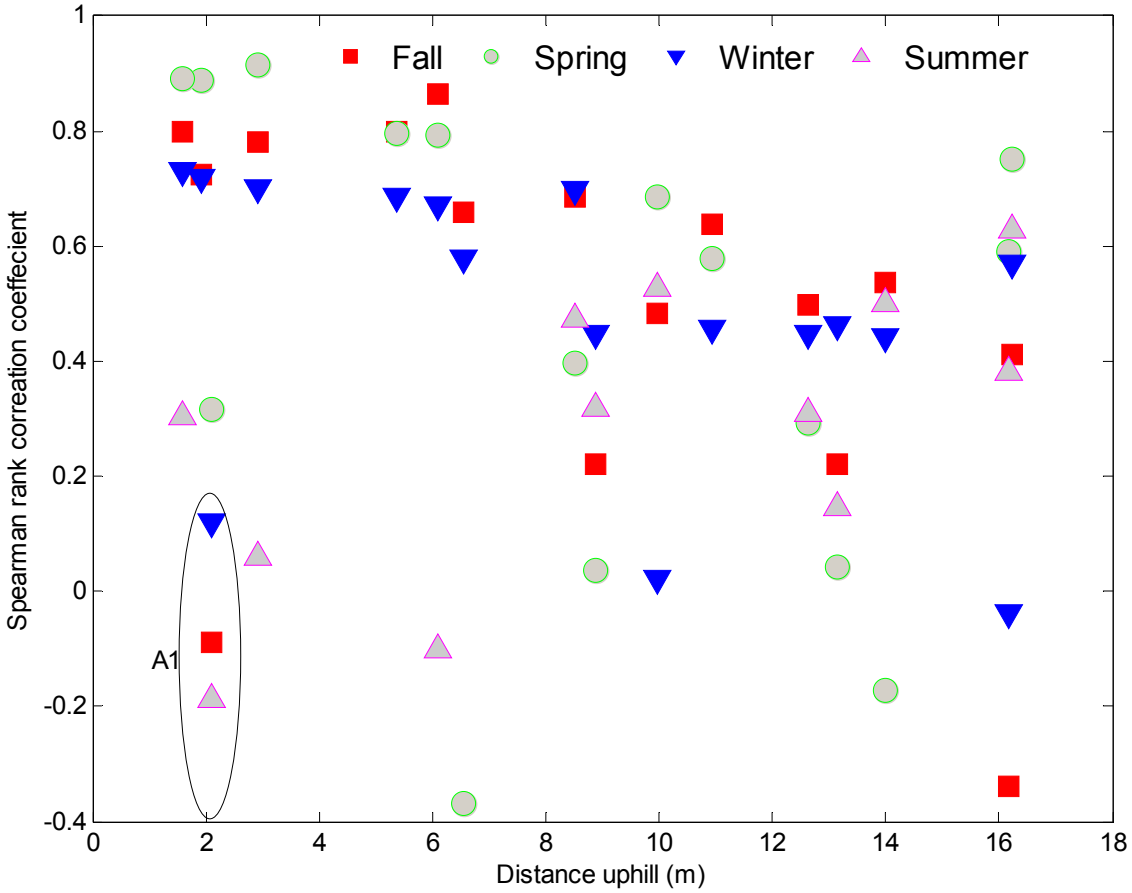

Figure 4.10. Histograms of the Spearman rank correlation coefficient between streamflow and groundwater level for the different seasons.

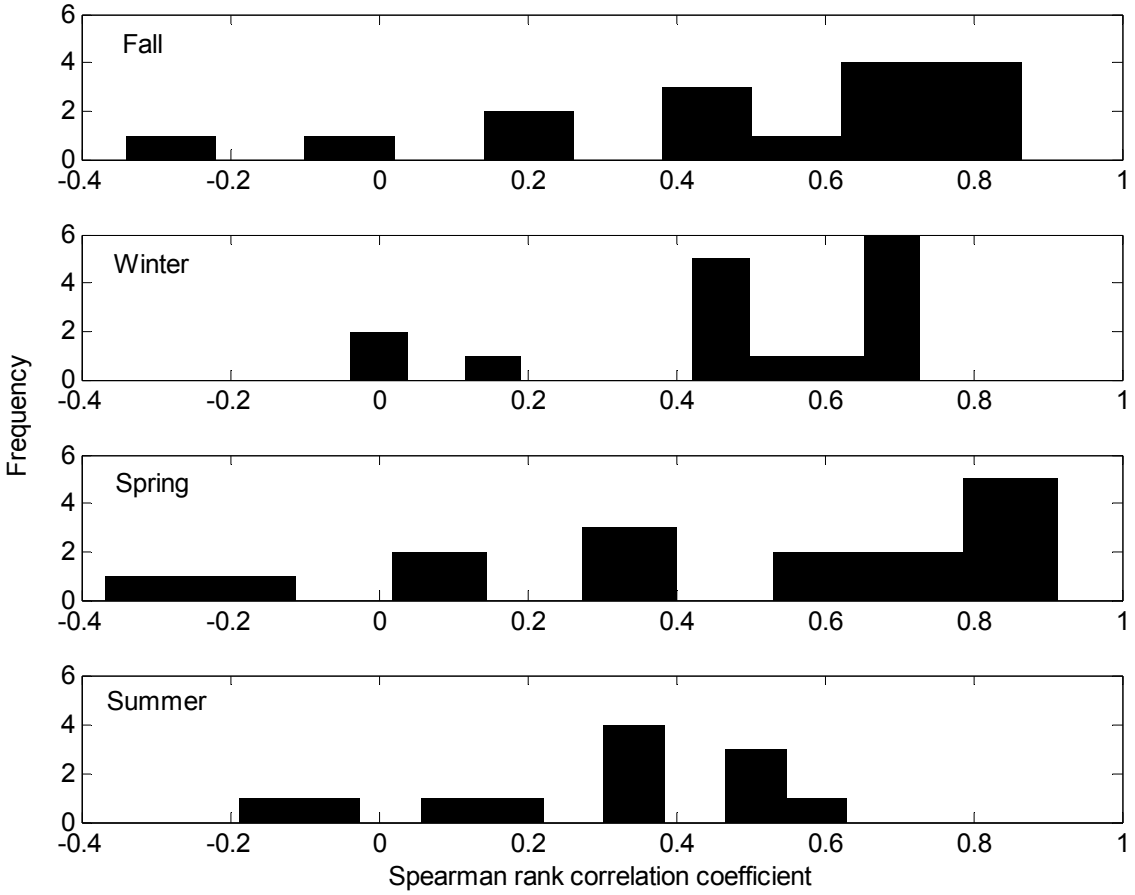

Figure 4.11. Relationship between the lag time between peak water level and peak discharge for specific storms in the fall/winter/spring of 2008/09. Positive lag times indicate that the stream responds before the water table responded.

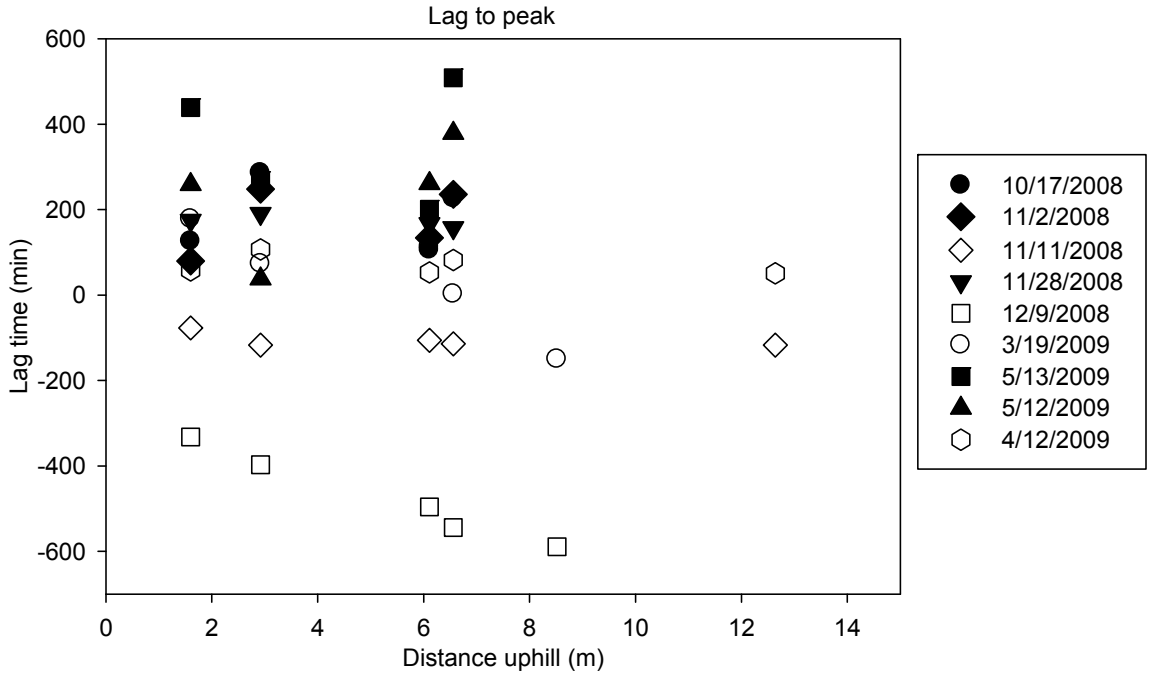

Figure 4.12. Relationship between the lag time between the start of piezometer response and the start of discharge response and distance uphill for specific storms in the fall/winter/spring of 2008/09.

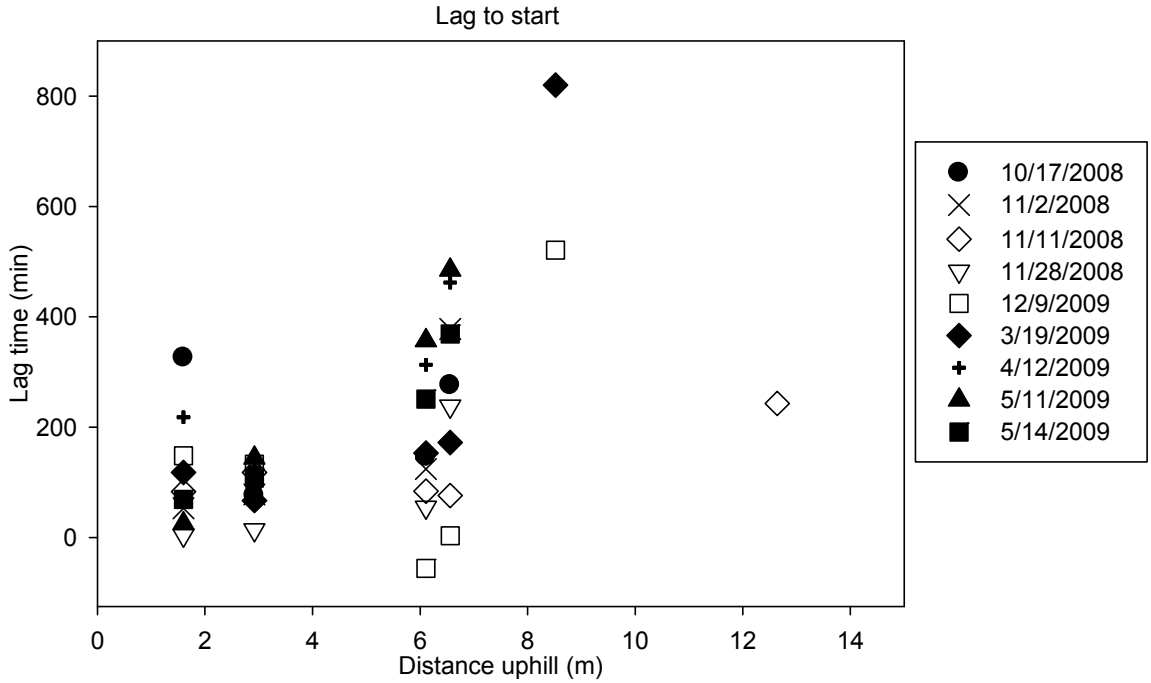

Figure 4.13. Lag optimized Spearman rank correlation coefficient between streamflow and groundwater response as a function of distance uphill for the fall of 2008. The size of the point represents the optimal lag time. Black circles represent negative lag times (water table responds before the discharge). White circles represent positive lag times (water tables that respond after discharge). Ranges of lag times are -2.5 to 22 hours with optimized negative lag times between -2.5 hours to -20 minutes and positive lag between 1 and 22 hours.

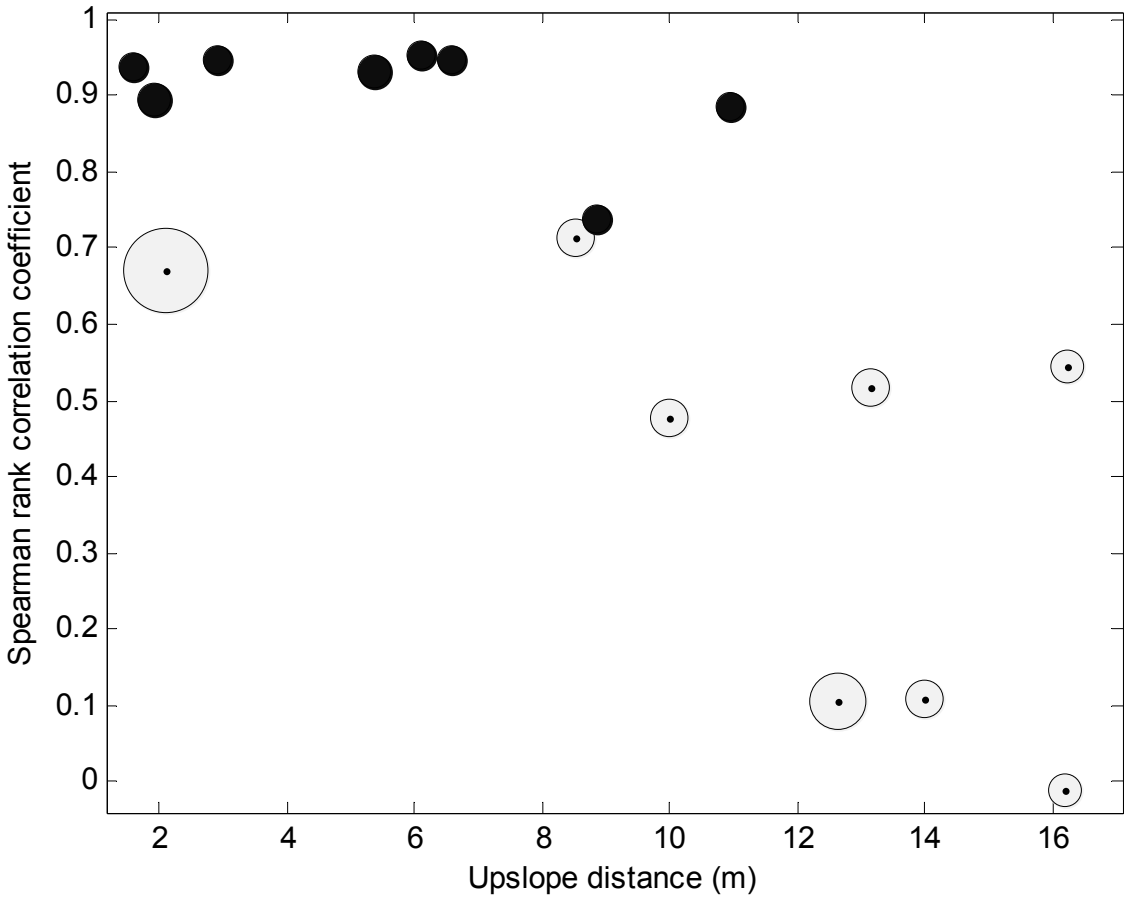

Figure 4.14. Water table, soil moisture, and streamflow response for storms occurring on: 11/7/2008 (top left), 12/09/2008 (top right), 3/01/2009 (bottom left), and 5/11/2009 (bottom right). The number in the top left of each graph represents the total precipitation for the storms.

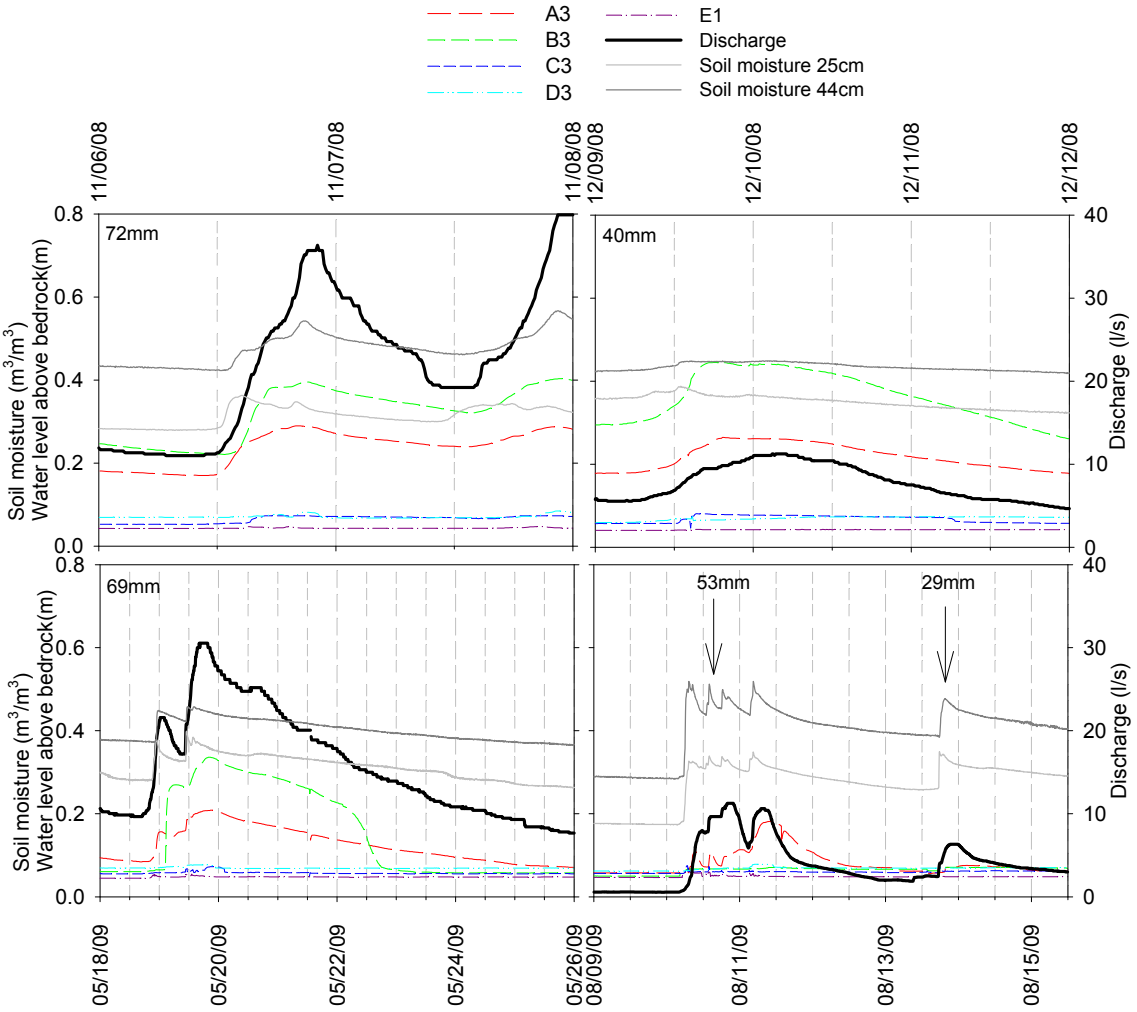

4.7 Tables

Table 4.1. Characteristics of the piezometers on the research hillslope. For the location of the piezometers see Figure 2.3 in chapter 2.

Piezometer	Depth to refusal (m)	Distance uphill (m)	Topographic wetness index value
A1	0.7	2.1	1.5
A2	0.7	1.9	0.8
A3	1.1	2.9	1.5
A4	0.7	1.6	3.5
B1	1.0	8.5	3.5
B2	1.1	5.4	4.0
B3	0.9	6.6	2.5
B4	1.0	6.1	2.0
C1	0.8	10.9	3.0
C2	0.8	10.0	2.8
C3	0.8	8.9	3.0
C4	0.8	8.9	n/a
D1	0.7	134.0	1.0
D2	0.7	13.1	3.0
D3	1.0	12.6	1.0
E1	1.1	16.2	1.8
E2	0.9	16.1	n/a
E3	1.1	16.2	1.0

Table 4.2. Correlations between hillslope parameters.

X variable	Y variable	Pearson r^2	Spearman r
Wetness index	a	0.2	
Distance uphill (m)	a	0.3	
Wetness index	b	$1.0\ 10^{-2}$	
Wetness index	Water table persistence(riparian)		0.7
Wetness index	Water table persistence(hillslope)		-0.2
Wetness index	Distance uphill (m)		-0.4
Water table persistence(whole)	Distance uphill (m)	0.7	-0.8
Spearman rank corr. Coefficient for the relation between groundwater level and streamflow	Distance uphill (m)	0.6	
Spearman rank corr. Coefficient for the relation between groundwater level and streamflow	Wetness index	0.1	
Lag optimized Spearman rank corr. Coefficient for the relation between groundwater level and streamflow	Distance uphill (m)		0.5

5: GENERAL CONCLUSION

5.1 Overview

My research was undertaken in the Malcolm Knapp Research Forest in British Columbia, Canada and aimed to examine runoff generation mechanisms in a steep forested watershed. My research questions were: (1) can water infiltrate into the bedrock in the study watershed, (2) can bedrock infiltration be described with simple infiltration models that have been developed for soil infiltration, and (3) what is the spatial variation in the relations between discharge and piezometric response on the hillslope? In order to answer these questions, I collected hydrometric data and conducted bedrock infiltration tests. I also examined the applicability of common soil infiltration models with regard to bedrock infiltration and a storage-runoff model. The results from this research have shown that water can infiltrate into the bedrock in the study watershed, and that infiltration is greater where bedrock is fractured. Simple infiltration models commonly used for soil infiltration can represent bedrock infiltration reasonably well, but have difficulties mimicking observed abnormalities which may be due to entrapped air within the fractures.

Hillslope water tables were found to vary spatially, contributing to two distinct zones: a riparian and hillslope zone. When addressing the original hypotheses:

- That water can infiltrate into bedrock, but the bedrock has a much lower hydraulic conductivity than the overlying soil.

- Common infiltration models cannot accurately describe bedrock infiltration patterns.
- Spatial differences in the relations between discharge and piezometric data are a function of the distance to the stream.

The first hypotheses holds true in that bedrock can infiltrate and leads to further hypotheses that should identify the significance of bedrock infiltration in relation to the hillslope and watershed water balance. The second hypothesis does not hold true because of the ability of simple infiltration models to represent bedrock infiltration reasonably well. The third hypothesis also hold true in that distance from the stream showed a well defined spatial distinction in the relationship between discharge and piezometric data.

5.2 Discussion

Chapter 3 showed that bedrock infiltration is possible and can represent up to 9% of precipitation within the study watershed. This shows that subsurface storm flow not only travels through the soil and over the bedrock, but also through the bedrock. These two distinct paths would have different residence times and response times. The hydraulic conductivity of the bedrock did not seem to be influenced by a change in scale (core to pond), suggesting that small fracture characteristics controlled infiltration rates. Common soil infiltration models were capable of describing initial bedrock infiltration rates reasonably well. Bedrock infiltration patterns showed some abnormalities (i.e. steps and spikes after initial infiltration) from common soil infiltration patterns and the models were incapable of mimicking these abnormalities. Preferential flow paths observed during the

rock core experiments depict the spatial variation in bedrock flow paths and bedrock hydraulic conductivity at the core scale, however, large scale fractures may dominate the response at the pond scale.

Chapter 4 showed that water tables in a steep hillslope expand from near-stream locations upslope. Hillslope water table dynamics were different in the riparian and hillslope zones. These two zones were distinguished by significant differences in persistence of a measureable water table and differences in the magnitude of response to rain events. The timing of the water table response was different in the two zones as well. This reflects the lack of measurable water table connectivity on the hillslope for most of the year and the influence of soil moisture, soil and bedrock storage, and preferential flow paths on water table dynamics. The lack of a measurable hillslope zone water table points to the potential for deeper, year-round hydraulic connection between the hillslope and the stream.

Chapter 3 showed that the spatial variation of infiltration into fractured bedrock was controlled by bedrock fracture presence. Chapter 4 showed that there were two distinct water table zones at the soil-bedrock interface that varied in response magnitude and persistence. Thus, bedrock infiltration across the watershed is partially controlled by the spatial and temporal variation that exists in water table depths above the bedrock since ponding on the bedrock induces infiltration into to the bedrock, and spatial variation in bedrock presence. This suggests that both infiltration into bedrock and water table dynamics are spatially variable and that their spatial interaction is important.

Gleeson et al. (2009) used isotopic and water level responses of groundwater to examine controls on bedrock recharge. They found that the spatial variation in soil depth and fractures created two distinct recharge mechanisms; one being rapid and localized and the other being slow and widespread. The rapid and localized infiltration occurred in areas of high frequency of fractures and well connected fracturing, whereas, slow widespread infiltration occurred when precipitation reached the bedrock surface and moved through the bedrock matrix. This research has shown how the concept of two bedrock recharge mechanisms, as described by Gleeson et al. (2009), is applicable to this research watershed in that the areas with conductive fractured bedrock and established and elevated water tables will induce relatively rapid recharge. Whereas, in areas with small, transient, or no water table presence, slow recharge through the matrix (i.e. soil to bedrock) would be relatively more important. This research further suggests that the spatial and temporal dynamics of transient saturation at the soil-bedrock interface contribute to the constraints that control the spatially variable bedrock infiltration. Bedrock infiltration has been shown to affect water table dynamics (i.e. hydrologic limitations, connectivity) as well. Though bedrock infiltration can influence subsurface storm flow, when bedrock infiltration capacities are exceeded by input rates, subsurface flow within the soil (and over the bedrock) dominates runoff generation.

A conceptual model of the hillslope would consist of three components: the hillslope, riparian, and bedrock zones (Figure 5.1). Precipitation inputs in the hillslope zone would move into both the riparian and bedrock zones with

movement into the riparian zone being the dominant process. Precipitation and riparian water would move into both the stream and bedrock, with the riparian to stream movement being the dominant process, especially when preferential flow paths are initiated. Bedrock water is suspected to move into both the stream and riparian zone via matrix and fractured bedrock flow paths, with the latter being a more significant contributor. Therefore, the stream receives water from at least three sources: the riparian and bedrock zones and direct precipitation. Flow paths within the riparian and bedrock zones have varying rates that contribute to varying residence times.

Figure 5.1. Conceptual model of the reseach hillslope. P, M and F denote preferential, matrix and fractured flow paths, respectively. Differences in arrow size are intended to distinguish flow proportion within each compartment.

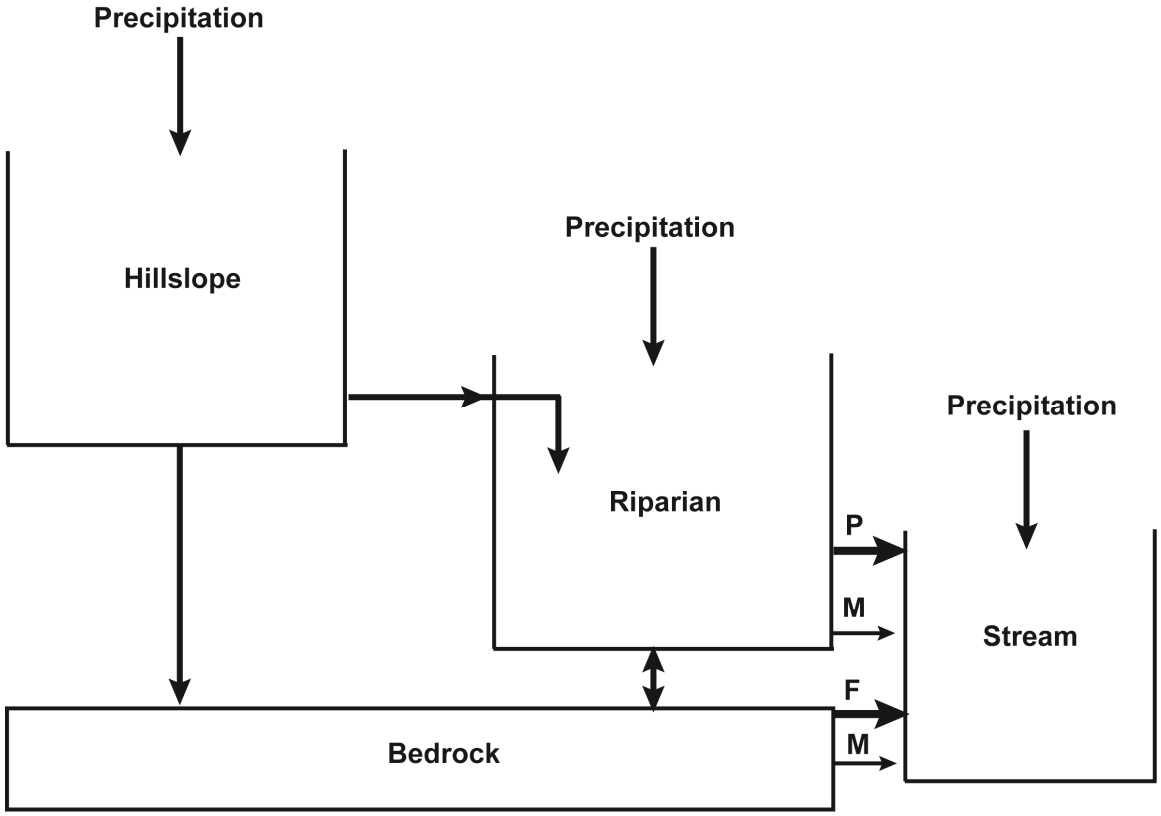

5.3 Future work

Future work that will help improve the understanding of runoff generation mechanisms in steep watersheds, with shallow soils in the coastal British Columbian mountains could include:

- Coupling of infiltration ponds and bedrock tensiometric data, along with bedrock piezometers, to better understand the mechanisms of bedrock recharge. High resolution imaging of bedrock fractures, along with tracer studies, may illuminate some of the paths of fluid transmittance. This may be done by using geophysical techniques: ground penetrating radar (GPR), multi-echo acoustic imaging, and magnetic resonance sounding.
- Modeling the data from the infiltration ponds using physical infiltration models to better understand and illuminate the mechanisms controlling bedrock infiltration. Evaluation of the mechanisms described by Gleeson et al. 2009 and Salve et al. (2008) (i.e. bedrock fracture vs. matrix fluid transmittance) using the experimental data from this work will be useful. These models could provide an initial investigation of the influences of air entrapment on bedrock infiltration and thus be used to develop more accurate bedrock infiltration models.
- Transects of high spatial/temporal resolution bedrock tensiometers/moisture sensors coupled with both bedrock and hillslope piezometers to better identify hillslope flow paths by illuminating responses to inputs and response times.
- High resolution GPR work to map bedrock microtopography and macropore paths below and in the soil (and maybe fractures in bedrock). Coupling this mapping with investigations that examine the spatial concentration of roots in order to identify macropore flow would increase our understanding of spatially varying soil moisture, water table dynamics, bedrock infiltration, and hillslope connectivity; all of which are important for understanding runoff generation mechanisms.

- Use of chemical and isotopic tracers, such as: SiO2, DOC, and δ18O, to better dissever contributions from bedrock, hillslope matrix, and new/old riparian water, respectively.

5.4 Conclusions

This research aimed at examining runoff generation mechanisms in a steep watershed and has shown that the near-stream water table responses at the soil-bedrock interface are different from those further uphill. Water table responses on the hillslope, and connectivity between the hillslope and the riparian zones, only occurs during large rainfall events. Hydrologically limited relations between water table response and runoff introduce potential difficulties for storage-runoff modelling, such as inaccuracies in the prediction of high discharge, and highlight the likely importance of flow through macropores. The bedrock in this watershed is permeable and infiltration into the bedrock is likely not a negligible portion of the watershed's water balance. Bedrock infiltration can be described reasonably well by commonly used soil infiltration models. Both bedrock infiltration and hillslope water tables are spatially variable. This research illuminates how bedrock infiltration and macropores influence the spatial and temporal variation in groundwater recharge within coastal British Columbia. It also describes how the compartmentalization of the watershed, and caution in model application and use, are necessary for models that are intended to describe runoff generation mechanisms in a steep small watershed in the British Columbian coast range.

REFERENCE LIST

Anderson S.P., Dietrich W.E., Montgomery D.R., Torres R., Conrad M.E., Logue K. 1997. Subsurface flow paths in a steep, unchanneled catchment. Water Resources Research 33(12), 2637:2653.

Asano Y., Uchida T., Ohte N. 2002. Residence times and flow paths of water in steep unchanneled catchments, Tanakami, Japan. Journal of Hydrology, 261, 173:192.

Beven K.J. and M.J. Kirkby.1979. A physically based, variable contributing area model of basin hydrology. Hydrological Sciences Bulletin, 24, 43:69.

Bryck, J.M.G. 1975. The renovation of domestic effluent through a forest soil, Ph. D. Thesis. University of British Columbia.

Cheng, Y.-C. 2007. Tracer study in a large undisturbed soil core from the Malcolm Knapp Research Forest. Unpublished Honors Thesis, Simon Fraser University, Burnaby, BC.

Chin K.S. 2009. The spatial variability in throughfall and soil moisture in a coastal British Columbian forest. Master's Thesis, Simon Fraser University., Burnaby, BC.

Dano K., Poeter E., Thyne G. 2008. Fate of individual sewage disposal system wastewater within regolith in mountainous terrain. Hydrogeology Journal, 16, 691:699.

de Vries J., and T.L. Chow. 1978. Hydrologic behavior of a forested mountain soil in coastal British Columbia. Water Resources Research, 14, 935:942.

Dingman S.L. 2002. Physical Hydrology, Second edition. Waveland Press, Long Grove, IL.

Fannin R.J., Jaakkola J., Wilkinson M.T., Hetherington E.D. 2000. Hydrologic response of soils to precipitation at Carnation Creek, British Columbia, Canada. Water Resources Research, 36, 1481:1494.

Freer J., McDonnell J., Beven K.J., Brammer D., Burns D., Hooper R.P., and Kendall C. 1997. Topographic controls on subsurface storm flow at the hillslope scale for two hydrologically distinct small catchments. Hydrological Processes 11(9), 1347:1352.

Freer J., McDonnell J., Beven K.J., Peters N.E., Burns D.A., Hooper R.P., Aulenbach B. and Kendall C. 2002. The role of bedrock topography on subsurface storm flow. Water Resources Research 38(12): 10.1029/2001WR000872.

Gleeson T., Novakowski K., Kyser T.K. 2009. Extremely rapid and localized recharge to a fractured aquifer. Journal of Hydrology, 376, 496:509.

Green W.H., and G.A. Ampt. 1911. Studies on soil physics, Part 1- The flow of air and water though soils. Journal of Agricultural Science, 4, 1:24.

Harr R. D. 1977. Water flux in soil and subsoil on a steep forested slope. Journal of Hydrology, 33, 37:58.

Hornberger G.M. 1998. Elements of Physical Hydrology. The John Hopkins University Press, Baltimore, MD.

Horton R. 1940. An approach toward a physical interpretation of infiltration-capacity. Processes of Soil Science Society of America, 5, 399:417.

Hutchinson D. G. and R. D. Moore. 2000. Throughflow variability on a forested hillslope underlain by compacted glacial till. Hydrological Processes 14, 1751:1766.

Hvorslev M.J. 1951. Time lag and soil permeability in groundwater observations. U.S. Army Corps of Engineers Waterways Exper. Stat. Bull. No. 36.

Jensco K.G., McGlynn B.L., Gooseff M.N., Wondzell S.M., Bencala K.E., Mashall L.A. 2009. Hydrologic connectivity between landscapes and streams: Transferring reach- and plot-scale understanding to the catchment scale. Water Resources Research, 45, doi: 10.1029/2008WR007225.

Katsura, S., Kosugi K., Yamamoto N., Mizuyama T. 2004. Understanding of infiltration processes to the bedrock of weathered granite (in Japanese). Trans. Jpn. For. Soc., 115, pp. 804.

Katsuyama M., Ohte N., Kabeya N. 2005. Effect of bedrock permeability on hillslope and riparian groundwater dynamics in a weathered granite catchment. Water Resources Research, 41, doi:10.1029/2004WR003275.

Katsuyama M., Kabeya N., Ohte N. 2009. Elucidation of the relationship between geographic and time sources of stream water using a tracer approach in a headwater catchment. Water Resources Research, 45, doi: 10.1029/2008WR007458.

Klinka K. 1976. Ecosystem units, their classification, interpretation and mapping in the University of British Columbia research forest. Ph. D. Thesis. University of British Columbia, Vancouver, BC.

Leopold L.B., Wolman M.G., Miller J.P. 1964. Fluvial Processes in Geomorphology. Dover, Mineola, NY.

Lerner D.N. 2009. Groundwater Matters. Hydrological Processes, 23, 3269:3270.

McDonnell, J. J. 1990. A rationale for old water discharge through macropores in a steep, humid catchment, Water Recourses. Research 26, 2821: 2832.

McDonnell J.J., 2003. Where does water go when it rains? Moving beyond the variable source area concept of rainfall-runoff response, Hydrological Processes 17, 1869–1875.

McDonnell J.J., Freer J.E., Hooper R.P., Kendall C., Burns D.A., Beven K.J., Peters N.E. 1996. New method developed for studying flow in hillslopes. EOS, Transactions of the American Geophysical Union 77(47), 465.

McGlynn B.L. and J.J. McDonnell. 2003a. Role of discrete landscape units in controlling catchment dissolved organic carbon dynamics. Water Resources Research, 39(4), doi: 10.1029/2002WR001525.

McGlynn B.L. and J.J. McDonnell. 2003b. Quantifying the relative contributions of riparian and hillslope zones to catchment runoff. Water Resources Research, 39(11) doi: 10.1029/2003WR002091.

McGlynn B. L. and J. Seibert. 2003. Distributed assessment of contributing area and riparian buffering along stream networks. Water Resources Research, 39(4), doi:10.1029/2002WR001521.

McGlynn B. L., McDonnell J. J., Seibert J., Kendall C. 2004. Scale effects on headwater catchment runoff timing, flow sources, and groundwater-streamflow relations. Water Resources Research, 40, doi:10.1029/2003WR002494.

McGuire KJ, McDonnell JJ, Weiler M, Kendall C, Welker JM, McGlynn BL. 2005. The role of topography on catchment-scale water residence time. Water Resources Research 41(5):W05002. doi:10.1029/ 2004WR003657.

Montgomery D.R., Dietrich W.E., Torres R., Anderson S.P., Heffner J.T., Loagues K. 1997. Hydrologic response of a steep unchanneled valley to natural and applied rainfall. Water Resources Research, 33, doi: 96WR02985.

Moore R. D. and J.C. Thompson. 1996. Are water table variations in a shallow forest soil consistent with the TOPMODEL concept. Water Resources Research, 32, 663: 669.

Moore R.D. and S.M. Wondzall. 2005. Physical hydrology and the effects on forest harvesting in the Pacific Northwest: a review. Journal of the American Water Resources Association. August.763:784.

Mosley M.P. 1979. Streamflow generation in a forested watershed. Water Resources Research 15, 795:806.

Negishi, J.N., Nogguchi S., Sidle R.C., Ziegler A.D., Abdul Rahim N. 2007. Stormflow generation involving pipe flow in a zero-order basin of Peninsular Malaysia. Hydrological Processes, 21, 789:806.

Onda Y., Komatsu Y., Tsujimura M., Fujihara J. 2001. The role of runoff through bedrock on storm flow generation. Hydrological Processes, 15, 1693:1706.

Ohte N., Suzuki S., Kubota J. 1989. Hydraulic properties of forest soils (I) The vertical distribution of saturated-unsaturated hydraulic conductivity (in Japanese with English summary). J. Jpn. For. Soc., 71, 137:147.

Peters D.L., Buttle J.M., Taylor C.H., LaZerte B.D. 1995. Runoff production in a forested, shallow soil, Canadian Shield basin. Water Resources Research 31(5), 1291:1304.

Philip J.R. 1969. Theory of infiltration. Advances in Hydroscience, 5, 215:296.

Philip J.R. 1992. Falling head ponded infiltration. Water Resources Research, 28, 2147:2148.

Redding T.E. and K.J. Devito. 2008. Lateral flow thresholds for aspen forested hillslopes on the Western Boreal Plain, Alberta, Canada. Hydrologic Processes 22, 4287:4300.

Salve R., Ghezzehei T.A., Jones R. 2008. Infiltration into fractured bedrock. Water Resources Research 44: W01434, doi:10.1029/2006WR005701.

Seibert J., Bishop K., Rodhe A., McDonnell J. J. 2003. Groundwater dynamics along a hillslope: A test of the steady state hypothesis. Water Resources Research. 39(1),doi:10.1029/2002WR001404.

Schulz M.S. and A.F. White. 1999. Chemical weathering in a tropical watershed, Luquillo Mountains, Puerto Rico III: quartz dissolution rates. Geochimica et Cosmochimica Acta, Vol. 63, No. 3/4, pp. 337:350.

Sidle R.C., Noguchi S., Tsuboyama T., Laursen K. 2001. A conceptual model of preferential flow systems in forested hillslopes: Evidence of self-organization. Hydrological Processes, 15(10), 1675:1692.

Stothoff S.A., Or D., Groeneveld D.P., Jones S.B. 1999. The effect of vegetation on infiltration in shallow soils underlain by fissured bedrock. Journal of Hydrology 169:190.

Tashe N.C. 1998. The impact of vine maple on the biogeochemical nutrient cycle of conifer-dominated coastal forests in southwestern British Columbia. M.Sc. Thesis. Simon Fraser University, Burnaby, BC.

Terajima T.A., Ishii H. 1993. Comparitive study of deep pecolation amount in two small catchments in granitic mountain. Japanese Journal of Hydrological Science, 23(2), 105:118.

Tromp-van Meerveld H.J., McDonnell J.J. 2006. Threshold relations in subsurface stormflow: 2. The fill and spill hypothesis. Water Resources Research 42(2): W02411. DOI: 10.1029/WR003800.

Tromp-van Meerveld H.J., Peters N.E., McDonnell J.J. 2007. Effect of bedrock permeability on subsurface stormflow and the water balance of a trenched hillslope at the Panola Mountain Research Watershed, Georgia, USA. Hydrological Processes 21, 750:769.

Torres R., Dietrich W.E., Montgomery D.R., Anderson S.P., Loague, K.1998. Unsaturated Zone Processes and The Hydrologic Response of A Steep, Unchanneled Catchment. Water Resources Research. 8, 1865:1879.

Uchida T., Asano Y., Ohte N., Mizuyama T. 2003. Seepagae area and rate of bedrock groundwater at a granitic unchanneled hillslope. Water Resources Research, 39(1), doi:10.1029/2002WR001298.

Uchida T., Kosugi K., Mizuyama T. 2002. Effects of pipe flow and bedrock groundwater on runoff generation in a steep headwater catchment in Ashiu, central Japan. Water Resources Research 38(7),1119. DOI: 10.1029/2001WR000261.

Uchida T., McDonnell J.J., Asano Y. 2006. Functional intercomparison of hillslopes and small catchments by examining water source, flowpath and mean residence time. Journal of Hydrology 327, 627:642.

Utting M.G. 1979. The generation of stormflow on a glaciated hillslope in coastal British Columbia, M.Sc. Thesis. University of British Columbia.

Vepraskas M.J. and J.P. Williams. 1995. Hydraulic conductivity of saprolite as a function of sample dimensions and measurement technique. Soil Science Society of America Journal, 59(4), 975:981.

Weiler M., McDonnell J.J., Tromp-van Meerveld I., Uchida T. 2005. Subsurface Stromflow. Encyclopedia of Hydrological Sciences.

Weiler M. and J.J. McDonnell. 2007. Conceptualizing lateral preferential flow and flow networks and simulating the effects on gauged and ungauged hillslopes. Water Resources Research, 43: doi:10.1029/2006WR004867.

Weyman D. R. 1973. Measurement of the downslope flow in a soil. Journal of Hydrology 20, 267:288.

Woods R. and L. Rowe. 1996. The changing spatial variability of subsurface flow across a hillside. Journal of Hydrology (NZ) 35(1), 51:86.

APPENDICES

Appendix 1: Bedrock and watershed characteristics

Figure A1. Stage-discharge relationship for the study watershed. Note that the two different symbols show the change in the relationship before and after the November 4, 2008 storm. For the location of the discharge measurements see Figure 2.2

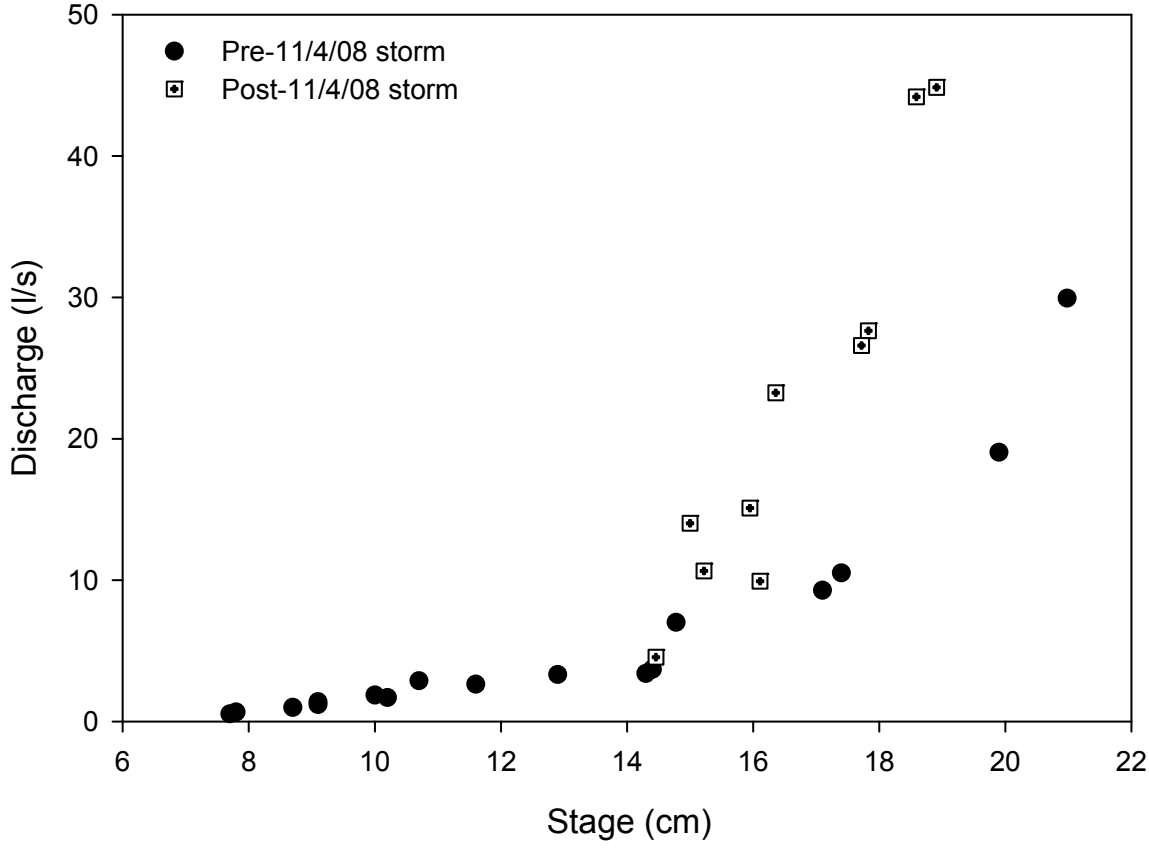

Figure A2. Stage - ln(discharge) relationship for the study watershed.

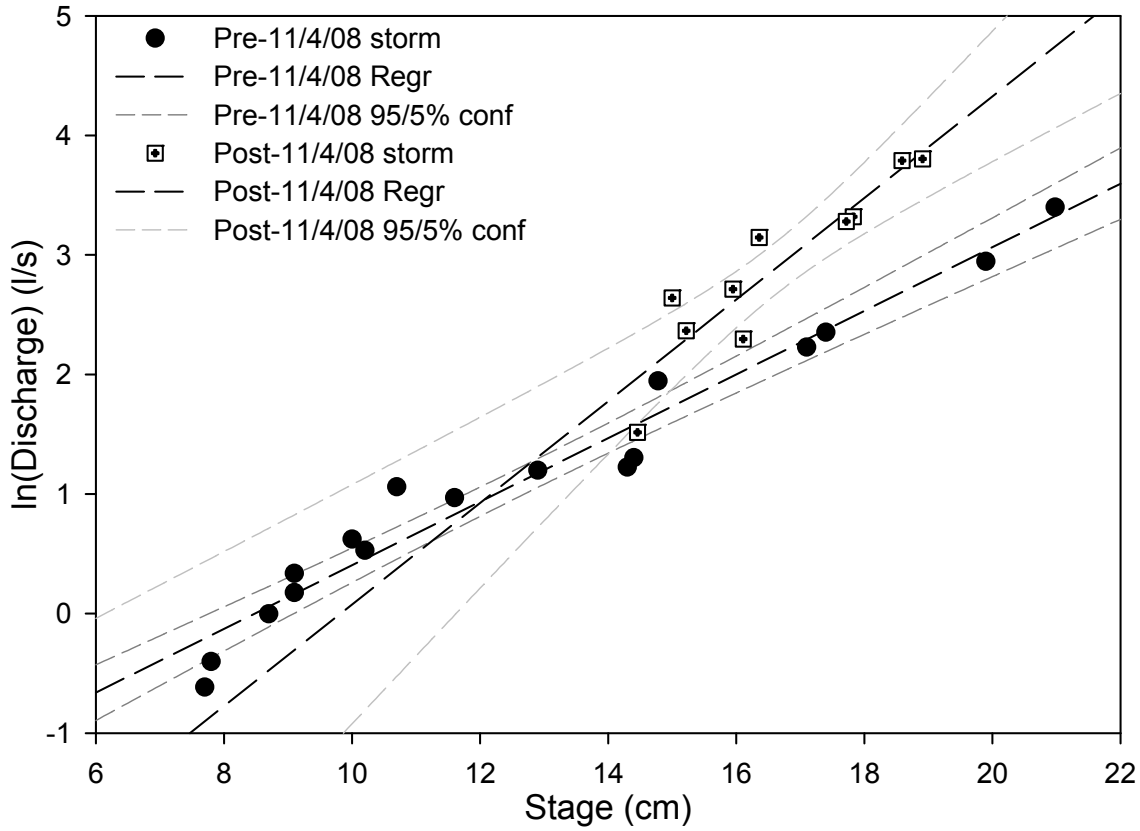

Figure A3. Water retention curves for surface soil core, granite and basalt samples taken from the research watershed.

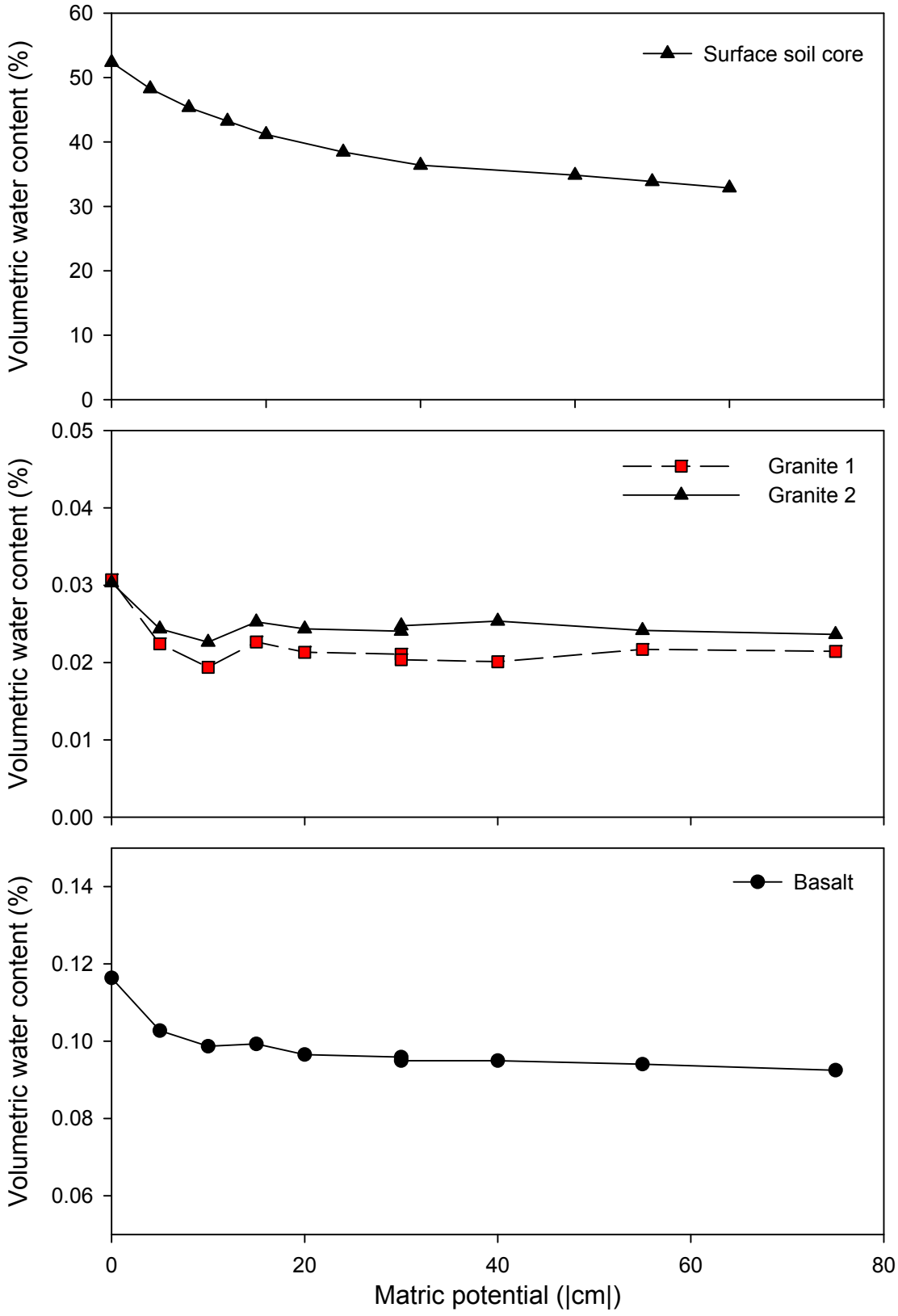

Figure A4. **Contributing area for the research watershed (~17 ha.) Note that area 2 contributes via ditches that channel water along the roads into the culvert on the northern boundary of the study watershed (in black).**

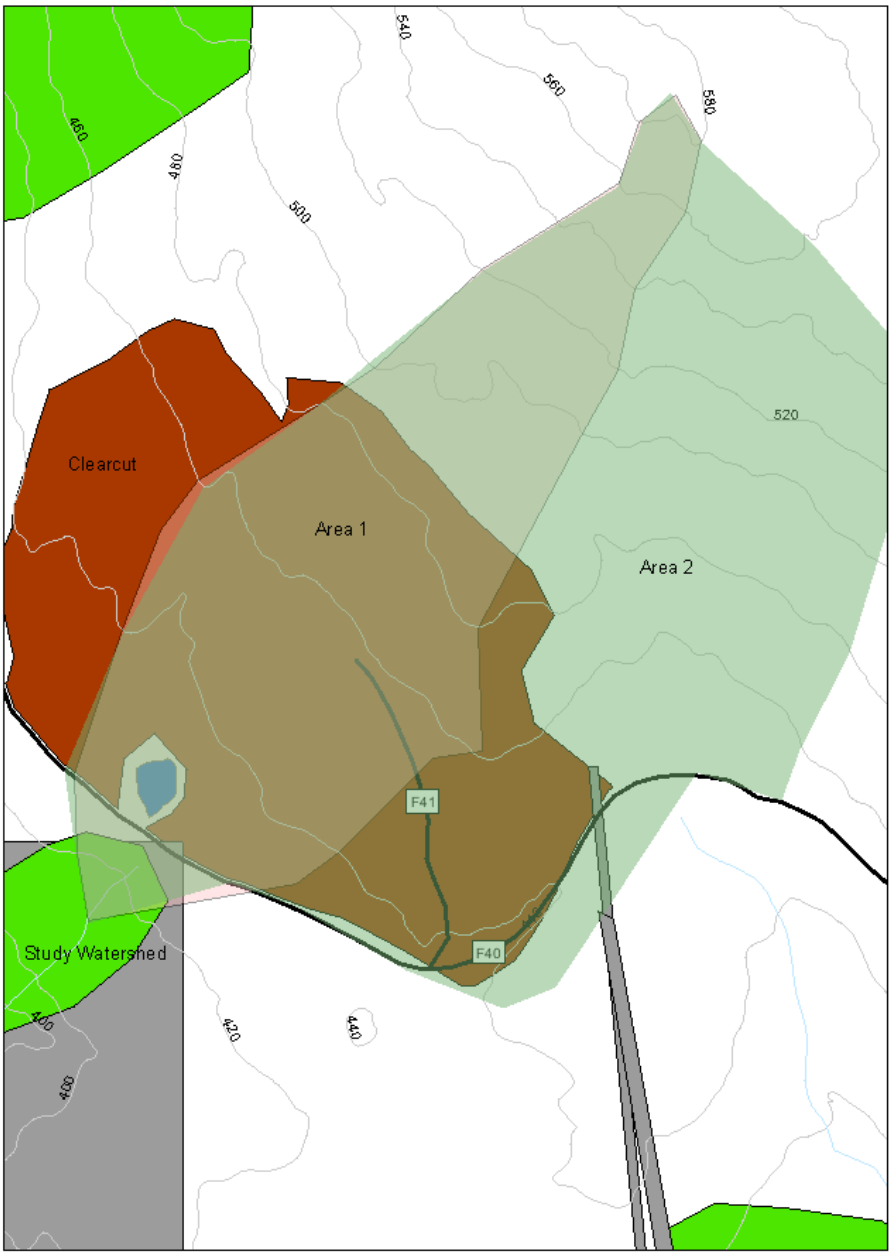

Appendix 2: Matlab© files

Horton sensitivity analysis

Determination of the sensitivity to the parameters in the Horton equation

```
pond=1;
ntimesteps=65;  %for pond 1
%ntimesteps=217; %for pond 2
tstep=12; %for pond 1
%tstep=1; %for pond 2
%time = time_P2;  %time since start (hr) for pond 2
%I=Infil_P2;    %observed cumulative infiltration (mm)for P2
time = time_P1;  %time since start (hr) for pond 1
I=Infil_P1;    %observed cumulative infiltration (mm)for P1

numit=2500;   %number of montecarlo runs for the dotty plots
best=0.001*numit+1;     %number of best runs to plot in blue and
determine min and max for type 1001 for the best 1000 resutls if 100000
runs

fomin=1e-2;    %for pond 1
fomax=1e0;        %for pond 1
fcmin=1.0e-11;   %for pond 1
fcmax=1e-1;          %for pond 1
kmin=1e-4;         %for pond 1
kmax=1e0;             %for pond 1

%fomin=1e-2;    %for pond 2
%fomax=1e4;        %for pond 2
%fcmin=1.0e-10;   %for pond 2
%fcmax=1e0;          %for pond 2
%kmin=1e-4;         %for pond 2
%kmax=1e4;             %for pond 2

fo_min=log10(fomin);
fo_max=log10(fomax);
fc_min=log10(fcmin);
fc_max=log10(fcmax);
k_min=log10(kmin);
k_max=log10(kmax);

for qq=1:numit
    fo =10^(fo_min+(fo_max-fo_min)*rand);
    fc =10^(fc_min+(fc_max-fc_min)*rand);
    k =10^(k_min+(k_max-k_min)*rand);

    t=0;
    i=0;
```

```
%calculate cumulative infiltration for different times
     for i=1:ntimesteps
        F(i)=(fc*t)+((fo-fc)/k)*(1-exp(-k*t));
        t=t+tstep;
    end

    Fo(qq)=fo;
    Fc(qq)=fc;
    K(qq)=k;
    HF=F';

    %calculate correlation coefficient
    r=corrcoef(HF,I);
    temp=r(1,2);
    R(qq)=temp;

   %calculate mean square error
    mse(qq)=mean(((HF-I).^2));

  %calculate mean absolute error
    mae(qq)=mean(abs(HF-I));


end

%create a new matrix with all the montecarlo results
results=[Fo',Fc',K',R',mse',mae'];
save horton_data20100126.out results -ASCII

%find best parameter set
[Rmax,q] = max(R)   %find parameter set with max correl coeff
[MSEmin,q2] = min(mse)   %find parameter set with min mean squared
error
[MAEmin,q3] = min(mae)   %find parameter set with min mean absolute
error

%calculate infiltration for best MSE parameter set
fo_dotty=Fo(q2)
fc_dotty=Fc(q2)
k_dotty=K(q2)
I_dotty=(fc_dotty*time)+((fo_dotty-fc_dotty)/k_dotty)*(1-exp(-
k_dotty*time));

%sort the data for the R
Rsorted= sortrows(results, 4);
Rbest=Rsorted(numit-best:numit,:);
    %and write down the best parameter sets to new variables
Fo_min_r = min(Rsorted(1:best,1));
Fo_max_r = max(Rsorted(1:best,1));
Fc_min_r = min(Rsorted(1:best,2));
Fc_max_r = max(Rsorted(1:best,2));
K_min_r = min(Rsorted(1:best,3));
K_max_r = max(Rsorted(1:best,3));

%sort the data for the MSE
MSEsorted= sortrows(results, 5);
```

```
MSEbest=MSEsorted(1:best,:);
    %and write down the best parameter sets to new variables
Fo_min_mse = min(MSEbest(:,1));
Fo_max_mse = max(MSEbest(:,1));
Fc_min_mse = min(MSEbest(:,2));
Fc_max_mse = max(MSEbest(:,2));
K_min_mse = min(MSEbest(:,3));
K_max_mse = max(MSEbest(:,3));


%sort the data for the MAW
MAEsorted= sortrows(results, 6);
MAEbest=MSEsorted(1:best,:);
%and write down the best parameter sets to new variables
Fo_min_mae = min(MAEbest(:,1));
Fo_max_mae = max(MAEbest(:,1));
Fc_min_mae = min(MAEbest(:,2));
Fc_max_mae = max(MAEbest(:,2));
K_min_mae = min(MAEbest(:,3));
K_max_mae = max(MAEbest(:,3));


%dotty plots
figure (1)
subplot(3,1,1)
    plot(Fo,R,'ok')
    hold on
    plot  (Fo(q),Rmax,'pr', 'MarkerSize',12)
    hold on
    plot (Rbest(:,1), Rbest(:,4), 'ob', 'MarkerFaceColor', 'b')
    xlim([fomin fomax])
    ylim([0.975 1])
    xlabel('fo (mm/hr)')
    title({['Pond ',int2str(pond)];['Acceptable range:
',num2str(Fo_min_r), '<fo<',num2str(Fo_max_r)]})
subplot(3,1,2)
    plot(Fc,R,'ok')
    hold on
    plot  (Fc(q),Rmax,'pr', 'MarkerSize',12)
    hold on
    plot (Rbest(:,2), Rbest(:,4), 'ob', 'MarkerFaceColor', 'b')
    xlim([fcmin fcmax])
    ylim([0.975 1])
    xlabel('fc (mm/hr)')
    ylabel('Correlation coefficient')
    title({['Acceptable range: ',num2str(Fc_min_r),
'<fc<',num2str(Fc_max_r)]})
subplot(3,1,3)
    plot(K,R,'ok')
    hold on
    plot (K(q),Rmax,'pr', 'MarkerSize',12)
    hold on
    plot (Rbest(:,3), Rbest(:,4), 'ob', 'MarkerFaceColor', 'b')
    xlim([kmin kmax])
    ylim([0.975 1])
    xlabel('k (1/hr)')
```

```
    title({['Acceptable range: ',num2str(K_min_r),
'<k<',num2str(K_max_r)]})

figure (2)
subplot(3,1,1)
    plot(Fo,mse,'ok')
    hold on
    plot (Fo(q2),MSEmin,'pr', 'MarkerSize',12)
    hold on
    plot (MSEbest(:,1), MSEbest(:,5), 'ob', 'MarkerFaceColor', 'b')
    xlim([fomin fomax])
    ylim([0 1.5])
    xlabel('fo (mm/hr)')
    title({['Pond ',int2str(pond)];['Acceptable range:
',num2str(Fo_min_mse), '<fo<',num2str(Fo_max_mse)]})
subplot(3,1,2)
    plot(Fc,mse,'ok')
    hold on
    plot (Fc(q2),MSEmin,'pr', 'MarkerSize',12)
    hold on
    plot (MSEbest(:,2), MSEbest(:,5), 'ob', 'MarkerFaceColor', 'b')
    xlim([fcmin fcmax])
    ylim([0 1.5])
    xlabel('fc (mm/hr)')
    ylabel('Mean Squared Error (mm^2)')
    title({['Acceptable range: ',num2str(Fc_min_mse),
'<fc<',num2str(Fc_max_mse)]})
subplot(3,1,3)
    plot(K,mse,'ok')
    hold on
    plot (K(q2),MSEmin,'pr', 'MarkerSize',12)
    hold on
    plot (MSEbest(:,3), MSEbest(:,5), 'ob', 'MarkerFaceColor', 'b')
    xlim([kmin kmax])
    ylim([0 1.5])
    xlabel('k (1/hr)')
    title({['Acceptable range: ',num2str(K_min_mse),
'<k<',num2str(K_max_mse)]})

figure (3)
subplot(3,1,1)
    plot(Fo,mae,'ok')
    hold on
    plot (Fo(q3),MAEmin,'pr', 'MarkerSize',12)
    hold on
    plot (MAEbest(:,1), MAEbest(:,6), 'ob', 'MarkerFaceColor', 'b')
    xlim([fomin fomax])
    ylim([0 1.5])
    xlabel('fo (mm/hr)')
    title({['Pond ',int2str(pond)];['Acceptable range:
',num2str(Fo_min_mae), '<fo<',num2str(Fo_max_mae)]})
subplot(3,1,2)
    plot(Fc,mae,'ok')
    hold on
    plot (Fc(q3),MAEmin,'pr', 'MarkerSize',12)
    hold on
    plot (MAEbest(:,2), MAEbest(:,6), 'ob', 'MarkerFaceColor', 'b')
```

```
    xlim([fcmin fcmax])
    ylim([0 1.5])
    xlabel('fc (mm/hr)')
    ylabel('Mean Absolute Error (mm)')
    title({['Acceptable range: ',num2str(Fc_min_mae),
'<fc<',num2str(Fc_max_mae)]})
subplot(3,1,3)
    plot(K,mae,'ok')
    hold on
    plot (K(q3),MAEmin,'pr', 'MarkerSize',12)
    hold on
    plot (MAEbest(:,3), MAEbest(:,6), 'ob', 'MarkerFaceColor', 'b')
    xlim([kmin kmax])
    ylim([0 1.5])
    xlabel('k (1/hr)')
    title({['Acceptable range: ',num2str(K_min_mae),
'<k<',num2str(K_max_mae)]})



figure (4)
plot(time,I_dotty,'-r',time,I,'ob'), grid on
legend('Horton (Monte-carlo optimized)','Observed')
title({['Pond ',int2str(pond)]})
xlabel('Time since start (hr)')
ylabel('Cumulative infiltration (mm)')

figure (5)
scatterhist(MSEbest(:,2), MSEbest(:,5))
title({['Pond ',int2str(pond)], 'MSE optimized'})
 xlabel('fc (mm/hr)')
 ylabel('Mean Squared Error (mm^2)')
```

Philip sensitivity analysis

Determination of the sensitivity to the parameters in the Philip equation

```
pond=1;
ntimesteps=65;  %for pond 1
tstep=12; %for pond 1
time = time_P1;  %time since start (hr)
I=Infil_P1;    %observed cumulative infiltration (mm)

%pond=2;
%ntimesteps=217; %for pond 2
%tstep=2; %for pond 2
%time = time_P2;  %time since start (hr)
%I=Infil_P2;    %observed cumulative infiltration (mm)

numit=2500;   %number of montecarlo runs for the dotty plots
best=0.001*numit+1;     %number of best runs to plot in blue and
determine min and max for type 1001 for the best 1000 resutls if 100000
runs
```

```
smin=1e-2; %for pond 1
smax=1e1;    %for pond 1
kmin=1e-11;   %for pond 1
kmax=1e-1;       %for pond 1

%smin=1e-4; %for pond 2
%smax=1e0;    %for pond 2
%kmin=1e-6;   %for pond 2
%kmax=1e-1;       %for pond 2

s_min=log10(smin);
s_max=log10(smax);
k_min=log10(kmin);
k_max=log10(kmax);

for qq=1:numit
    s =10^(s_min+(s_max-s_min)*rand);
    k =10^(k_min+(k_max-k_min)*rand);

    t=0;
    i=0;

%calculate cumulative infiltration for different times
     for i=1:ntimesteps
        F(i)=(k*t)+(s*(t^0.5));
        t=t+12;
    end

    S_o(qq)=s;
    K_o(qq)=k;
    HF=F';

    %calculate correlation coefficient
    r=corrcoef(HF,I);
    temp=r(1,2);
    R(qq)=temp;

   %calculate mean square error
    mse(qq)=mean(((HF-I).^2));

  %calculate mean absolute error
    mae(qq)=mean(abs(HF-I));


end

%create a new matrix with all the montecarlo results
results=[S_o',K_o',R' ,mse',mae'];
    save philip_data20090513.out results -ASCII

%find best parameter set
[Rmax,q] = max(R)   %find parameter set with max correl coeff
[MSEmin,q2] = min(mse)   %find parameter set with min mean squared
error
[MAEmin,q3] = min(mae)   %find parameter set with min mean absolute
error
```

```
%calculate infiltration for best MSE parameter set
So_dotty=S_o(q2)
k_dotty=K_o(q2)
I_dotty=(k_dotty*time)+(So_dotty*(sqrt(time)));

%sort the data for the R
Rsorted= sortrows(results, 3);
Rbest=Rsorted(numit-best:numit,:);
    %and write down the best parameter sets to new variables
So_min_r = min(Rsorted(1:best,1));
So_max_r = max(Rsorted(1:best,1));
K_min_r = min(Rsorted(1:best,2));
K_max_r = max(Rsorted(1:best,2));

%sort the data for the MSE
MSEsorted= sortrows(results, 4);
MSEbest=MSEsorted(1:best,:);
    %and write down the best parameter sets to new variables
So_min_mse = min(MSEbest(:,1));
So_max_mse = max(MSEbest(:,1));
K_min_mse = min(MSEbest(:,2));
K_max_mse = max(MSEbest(:,2));


%sort the data for the MAE
MAEsorted= sortrows(results, 5);
MAEbest=MSEsorted(1:best,:);
%and write down the best parameter sets to new variables
So_min_mae = min(MAEbest(:,1));
So_max_mae = max(MAEbest(:,1));
K_min_mae = min(MAEbest(:,2));
K_max_mae = max(MAEbest(:,2));


%dotty plots
figure (1)
subplot(2,1,1)
    plot(S_o,R,'ok')
    hold on
    plot  (S_o(q),Rmax,'pr', 'MarkerSize',12)
    hold on
    plot (Rbest(:,1), Rbest(:,3), 'ob', 'MarkerFaceColor', 'b')
    xlim([smin smax])
    ylim([0.9 1])
    xlabel('S (mm/hr^0.5)')
    ylabel('Correlation Coefficient')
    title({['Pond ',int2str(pond)];['Acceptable range:
',num2str(So_min_r), '<S<',num2str(So_max_r)]})
subplot(2,1,2)
    plot(K_o,R,'ok')
    hold on
    plot  (K_o(q),Rmax,'pr', 'MarkerSize',12)
    hold on
    plot (Rbest(:,2), Rbest(:,3), 'ob', 'MarkerFaceColor', 'b')
    xlim([kmin kmax])
    ylim([0.9 1])
```

```
    xlabel('K (mm/hr)')
    ylabel('Correlation Coefficient')
    title({['Acceptable range: ',num2str(K_min_r),
'<K<',num2str(K_max_r)]})

figure (2)
subplot(2,1,1)
    plot(S_o,mse,'ok')
    hold on
    plot (S_o(q2),MSEmin,'pr', 'MarkerSize',12)
    hold on
    plot (MSEbest(:,1), MSEbest(:,4), 'ob', 'MarkerFaceColor', 'b')
    xlim([smin smax])
    ylim([0 5])
    xlabel('S (mm/hr^0.5)')
    ylabel('Mean Squared Error (mm^2)')
    title({['Pond ',int2str(pond)];['Acceptable range:
',num2str(So_min_mse), '<S<',num2str(So_max_mse)]})
subplot(2,1,2)
    plot(K_o,mse,'ok')
    hold on
    plot (K_o(q2),MSEmin,'pr', 'MarkerSize',12)
    hold on
    plot (MSEbest(:,2), MSEbest(:,4), 'ob', 'MarkerFaceColor', 'b')
    xlim([kmin kmax])
    ylim([0 5])
    xlabel('K (mm/hr)')
    ylabel('Mean Squared Error (mm^2)')
    title({['Acceptable range: ',num2str(K_min_mse),
'<K<',num2str(K_max_mse)]})

figure (3)
subplot(2,1,1)
    plot(S_o,mae,'ok')
    hold on
    plot (S_o(q3),MAEmin,'pr', 'MarkerSize',12)
    hold on
    plot (MAEbest(:,1), MAEbest(:,5), 'ob', 'MarkerFaceColor', 'b')
    xlim([smin smax])
    ylim([0 3])
    xlabel('S (mm/hr^0.5)')
    ylabel('Mean Absolute Error (mm)')
    title({['Pond ',int2str(pond)];['Acceptable range:
',num2str(So_min_mae), '<S<',num2str(So_max_mae)]})
subplot(2,1,2)
    plot(K_o,mae,'ok')
    hold on
    plot (K_o(q3),MAEmin,'pr', 'MarkerSize',12)
    hold on
    plot (MAEbest(:,2), MAEbest(:,5), 'ob', 'MarkerFaceColor', 'b')
    xlim([kmin kmax])
    ylim([0 3])
    xlabel('K (mm/hr)')
    ylabel('Mean Absolute Error (mm)')
    title({['Acceptable range: ',num2str(K_min_mae),
'<K<',num2str(K_max_mae)]})
```

```
figure (4)
plot(time,I_dotty,'-r',time,I,'ob'), grid on
legend('Philip (Monte-carlo optimized)','Observed')
title({['Pond ',int2str(pond)]})
xlabel('Time since start (hr)')
ylabel('Cumulative infiltration (mm)')

figure (5)
scatterhist(MSEbest(:,2), MSEbest(:,4))
title({['Pond ',int2str(pond)], 'MSE optimized'})
 xlabel('K (mm/hr)')
 ylabel('Mean Squared Error (mm^2)')
```

Spearman Rank Correlation Coefficient Lag Analysis

Correlates discharge as a function of stage height producing a maximum Spearman rank and optimal lag time.

```
%Input Data variable in column format.

t= summer_i31911 (3314:5906); %time
a= sumQ31911 (3314:5906); %first data series - the stream discharge
b= summer_31911 (3314:5906); % second dataseries - the piezometer stage
maxlag=144;  %maximum positive time shift for cross correlation for 24
% hours at 10 min timesteps
maxneglag=432;  %432 maximum negative time shift for cross correlation
for 72
% hours at 10 min timesteps

%Fall=11/02/08 to 11/18/08 (except 31910; 11/17/08 to 11/30/08 and
32620
%11/1/08 to 11/12/08. 31909,31911,&42056: 11/3/08 1200 to 11/18/08)
%Summer= 6/24/09 to 7/12/09 (except 31909 and 31910; 6/21/09 to
6/30/09)

[m,n]=size(a);
[o,p]=size(b);

figure (1)  % creates a double-axis line plot representing
discharge(red)
% on the left axis and water table height (black) on the right axis
line(t,a,'Color','r');
ax1 = gca;
set(ax1,'XColor','r','YColor','r')
ax2 = axes('Position',get(ax1,'Position'),...
           'XAxisLocation','top',...
           'YAxisLocation','right',...
           'Color','none',...
           'XColor','k','YColor','k');
line(t,b,'Color','k','Parent',ax2);
```

```
figure (2)
scatterhist(a,b,[10 10])% scatter plot with a 10 bin histogram for both
x
% and y axes

%maxlag=432;  %maximum time shift for cross correlation
lengthR=maxlag+1;
R=zeros (lengthR,1);
lag=[0:1:maxlag]';
i=0;

%calculate correlation coefficient for positive lag
for i=0:1:maxlag
    newlengthb=o-i; %change length of b to account for shift in b
    bselect=b(1:newlengthb); %selected part of b to use in correlation
    starta=1+i;
    aselect=a(starta:m);

RHO=corr(aselect,bselect,'type','spearman','rows','complete','tail','ne
');
    temp=RHO;
    j=i+1;
    R(j)=temp; %write down the r for this lag
    lag (j)=i;
end


%calculate correlation coefficient for negative lag
lengthRR=maxneglag+1;
RR=zeros (lengthRR,1);
negativelag=[0:1:maxneglag]';
i=0;
for i=0:1:maxneglag
    newlengtha=m-i; %change length of b to account for shift in b
    aselect=a(1:newlengtha); %selected part of b to use in correlation
    startb=1+i;
    bselect=b(startb:o);
RHO=corr(aselect,bselect,'type','spearman','rows','complete','tail','ne
');
    temp=RHO;
    j=i+1;
    RR(j)=temp; %write down the r for this lag
    negativelag (j)=-i;
end

CorrelCoef=[RR;R]; %combine positive and negative lag data
Lag=[negativelag;lag]; %combine positive and negative lag data
[Rmax,q] = max(CorrelCoef) ;  %find parameter set with max correl coeff
optimumlag=Lag(q)
maxcorrel=Rmax

figure (3)
plot(lag, R, '-r*', negativelag, RR, '--r*')
hold on
plot (optimumlag, Rmax, 'bp', 'markersize',10)
xlabel ('lag (timesteps)')
```

```
ylabel ('Spearman correlation coeffecient (RHO)')
```

Bubble Plot

```
Scatter plot in x and y using arbitrary-color "." as
plot symbol - whose point-by-point size is proportional
the magnitude of z

%x values - should be distance upslope
%y values - should be correlation lengths
% z should be lag values

x=dist_uphill;
y=Spearman_seasonal_fall_RHO;
z=Spearman_seasonal_fall_lag;

color = [0.05,0.05,0.05]; %very dark gray
color2 = [0.95,0.95,0.95]; %very light gray

for i=1:length(z)
if z(i)<0 %negative z values
    zneg(i)=z(i); %negative z values (Dark gray)
    zpos(i)=NaN;
else
    zpos(i)=z(i); %positive z values (light Gray)
    zneg(i)=NaN;
    i=1+i;
end
end


BubblePlot_new (x,y,zpos,color2, 0.15)
hold on
BubblePlot_new (x,y,zneg,color,0.15)
xlabel('Upslope distance (m)')
ylabel('Spearman rank correlation coefficient')

h=bubbleplot_new(x,y,z,color,sf)
%function h=bubbleplot_new(x,y,z,color,sf)

%INPUT
%  x     - n-dimension vector
%  y     - n-dimension vector
%  z     - n-dimension vector (used to size the plot symbols)
%  color - plot symbol color (must be a 3-element vector
%          with elements in range 0 1) ..................... default:
alternating 10 colors
%  sf    - plot symbol size scale factor ................. default: 35

n = nargin;
if n<5 | isempty(sf), sf = 35; end
if n<4 | isempty(color),
   myco=[ 0     0     1.00
          0     0.50  0
```

```
          1.00  0     0
          0     0.75  0.75
          0.75  0.75  0.75
          0.75  0     0.75
          0.25  1.00  0.25
          0.75  0.75  0
          0.25  0.25  0.25
          0.50  0.50  0.50 ];
else
   col = color(:)';
   myco = [col;col;col;col;col;col;col;col;col;col];
end
%scf=sf./(max(z(:))-min(z(:)));
%zp=round( (z-min(z(:)) ) .*scf +5);
zp=round(abs(z.*sf) +9);
I = find(isnan(zp));
zp(I) = eps;
for i = 1:length(x),
   cc = i;
   if cc>10,
      cc = mod(cc,10)+1;
   end

plot(x(i),y(i),'o','MarkerSize',zp(i),'MarkerFaceColor',myco(cc,:),'Mar
kerEdgeColor','k');
   hold on;
end
hold off
axis('tight')
ax=axis ;              % L R B T
xr=.03*(ax(2)-ax(1));
yr=.03*(ax(4)-ax(3));% scale axis based on data range
axis([ax(1)-xr ax(2)+2*xr ax(3)-yr ax(4)+2*yr]);
hold off;
h = gca;
```

Appendix 3. Tracer experiment

Introduction

Subsurface flow is the dominant runoff generation mechanism in many steep, humid watersheds (Weiler et al. 2005). Recent literature (Woods and Rowe 1996; Hutchison and Moore 2000; McDonnell et al. 1996; Freer et al. 1997; Tromp-van Meerveld and McDonnell 2006; McGuire et al. 2005; Uchida et al. 2002; Freer et al. 2002, 1997; McDonnell et al. 1996) has looked at the effects of spatially variable bedrock depth and its influences on lateral flow at the soil-bedrock interface.

Uchida et al. (2002) found that a threshold existed of 30 mm of precipitation: below the threshold Darcian flow was present and above the threshold pipe flow was dominant. More recently, the concept of a threshold behavior on hillslope processes has been investigated as a bedrock control (Tromp-van Meerveld and McDonnell 2006; McDonnell 2003). Tromp-van Meerveld and McDonnell (2006) explained the threshold behavior as an effect of the fill and spill mechanism. Similar to Uchida et al. (2002), they found that a threshold existed at 55 mm of precipitation. The threshold was attributed to the need for the transient saturated zone to breach the ‘dam’ created by bedrock ridges. These finding reflect the need for connectivity of transient saturated areas within the hillslope.

In most cases this recent research has coupled either soil moisture (Freer et al. 2002), antecedent conditions (Woods and Rowe 1996), or transient saturated zone presence (Tromp-van Meerveld 2006) with trench outflow and the topographic wetness index to describe the spatial variation of subsurface storm

flow. Though this research has examined the temporal behaviour of subsurface storm flow and pipe flow, there is little work that has examined the spatial variability of water and tracer movement within the hillslope.

The intent of this study was to couple tracer data from shallow, medium, and deep soil horizons to better understand the influence of microtopography and permeable bedrock on the spatial variation of subsurface storm flow at the hillslope scale. Unfortunately, the tracer was not observed in the streamflow and the study suffered from uncooperative weather and equipment failure.

Methods

Tracer Application

To understand the spatial and temporal variation of shallow subsurface storm flow to rain events, two tracers were deployed on the 400m^2 hillslope. The first tracer, NaCl, was deployed at the surface (0.75 m^2 area) while the second, LiBr, was applied in piezometer E3 (Figure A5). The deployment of two tracers on both the surface and at the soil-bedrock interface (i.e. within the piezometer) was done to illuminate the differences in timing between the lateral flow (only) and lateral and vertical flow. Six kilograms of NaCl and two kilograms of LiBr was used. Both tracers were mixed into a solution. The surface application was done with a pesticide sprayer. The LiBr was applied by pouring the solution into the empty piezometer. Both tracer application methods included rinsing of the respective containers. Both tracers were applied on November 20, 2008 and sampling was conducted until February 9th, 2009.

From November 20, 2008 to February 10, 2009 accumulated precipitation was 412.5 mm and total snow depth was 90 cm. A large snow event occurred from January 1 to January 3, 2009 resulting in 31cm of snow. The snow melted on January 6, 2009. This event resulted in the highest stage height (27.5 cm) and thus the highest discharge measured in the study period.

Piezometers and suction lysimeters

The hillslope was instrumented with 18 piezometers and 20 suction lysimeters. Each piezometer location was augured to refusal and backfilled if necessary (B4 and E2 did not reach refusal). Thirty seven millimeter diameter PVC pipe was used to construct the piezometers. Each piezometer was perforated for the bottom 10 cm and covered in mesh. Each piezometer was instrumented with an ODYWL05/10/15 (0.5, 1.0, 1.5 m; respectively) Odyssey capacitance water level probe set at 10 minute intervals (Christchurch, NZ). Suction lysimeters were made with 37 mm diameter PVC pipe and capped with porous ceramic cups (glued together) (Ibar Soil Moisture Equipment Corp. Goleta, CA). Lysimeters 1-10 were augured to depths of 47.9±3.1 cm while lysimeters 11-20 were at depths of 26.0±4.6 cm. Soil water samples were collected twice a week from November 20, 2008 to December 16, 2009, and then once monthly for the next two months and when water was present from the piezometers as well. To obtain soil water samples 15 to 20 centibars of soil pressure was applied to each suction lysimeter. A battery operated pump was used for sampling. Samples were analyzed for EC (µS/cm) and bromide concentrations (ppm) using the Hanna HI991300 pH/EC/TDS meter (Laval,

Canada) and Northwest Instruments TempHion sensor (Seattle, USA), respectively. Stream samples were taken manually and with an ISCO water sampler set to take samples every 2 hours initially and every 6-12 hours later in the experiment. The EC was measured continuously in the stream with the YSI 6920 v2 probe (Yellow Springs, USA). Bromide was measured continuously with a Northwest Instruments TempHion probe (Seattle, WA, USA).

Precipitation gauging

See chapter 4.2.2.2.

Stream gauging

See chapter 4.2.2.4

Figure A5. Map of the study hillslope showing the locations of the instrumentation. For piezometer, locations see also Figure 2.3 in chapter 2.

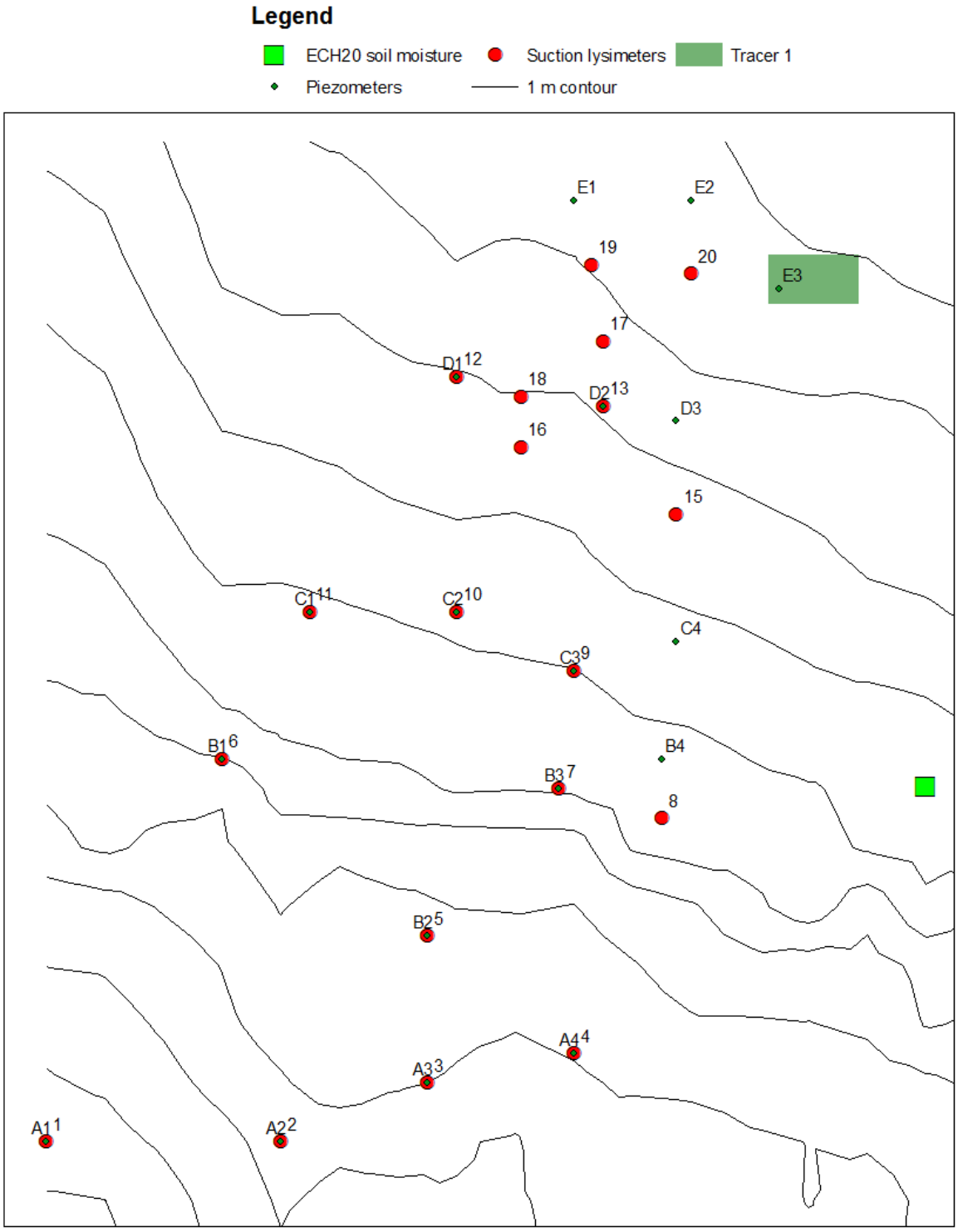

Figure A6. Hydrograph and hyetograph, along with the streamflow response during the tracer deployment. Note that the tipping bucket rain gauge was occasionally frozen from December 15, 2008 to January 30, 2009 and thus did not accurately record the precipitation during this period. Precipitation measured at the Malcolm Knapp Research Forest administration station (see Ch. 4.2.2.2) is shown for comparison as well.

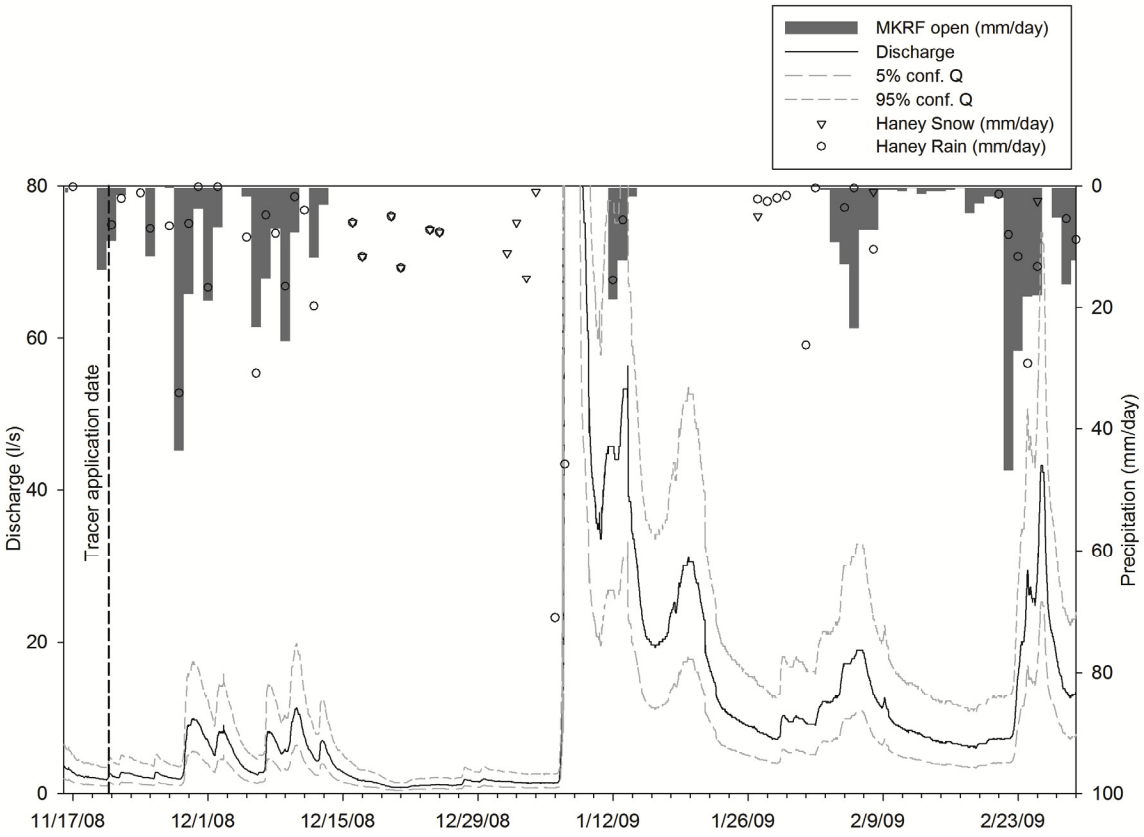

Figure A7. Time-series of the bromide concentrations in the piezometers and suction lysimeters.

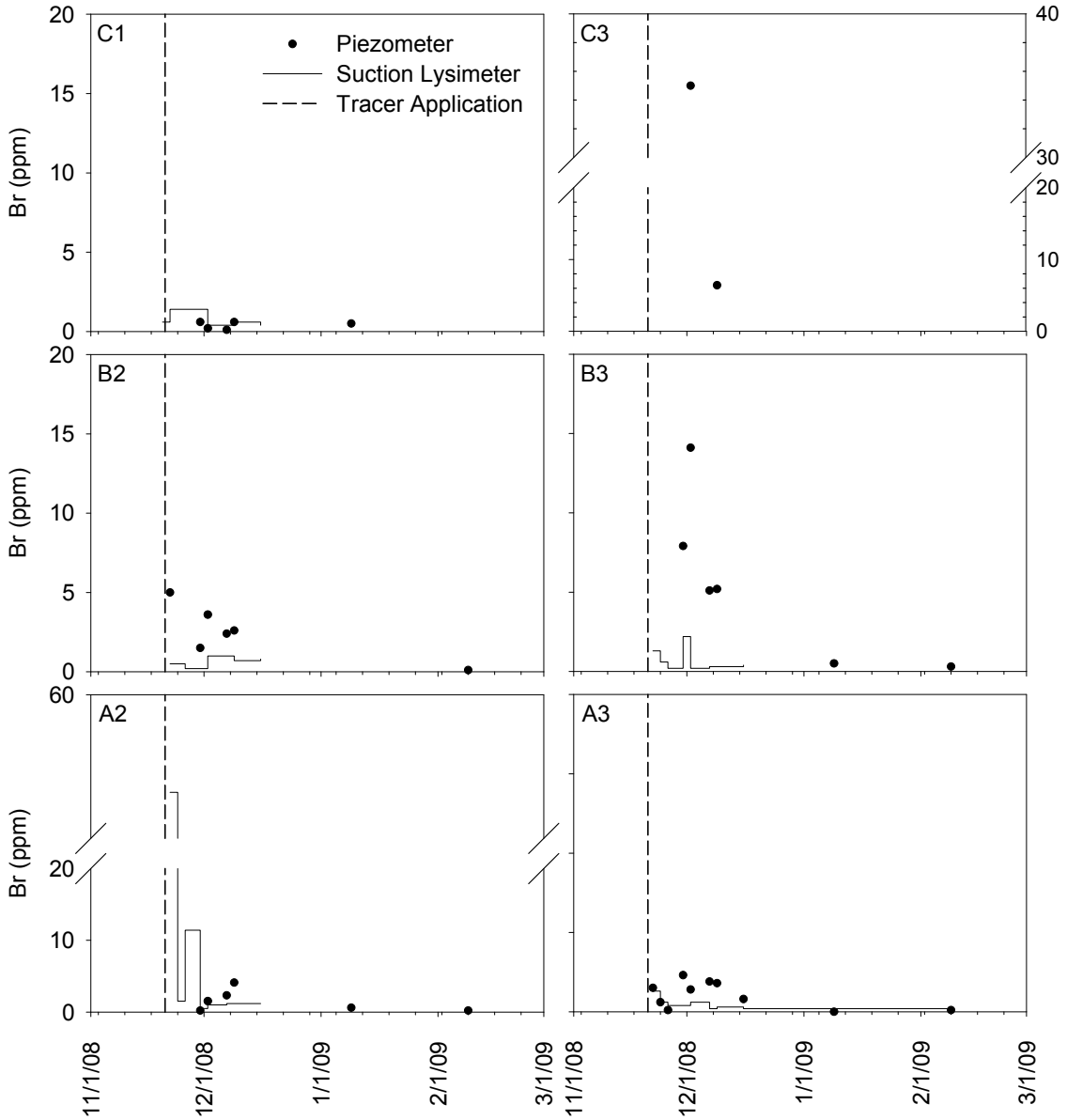

Figure A8. Time-series of EC for samples taken from piezometers and suction lysimeters.

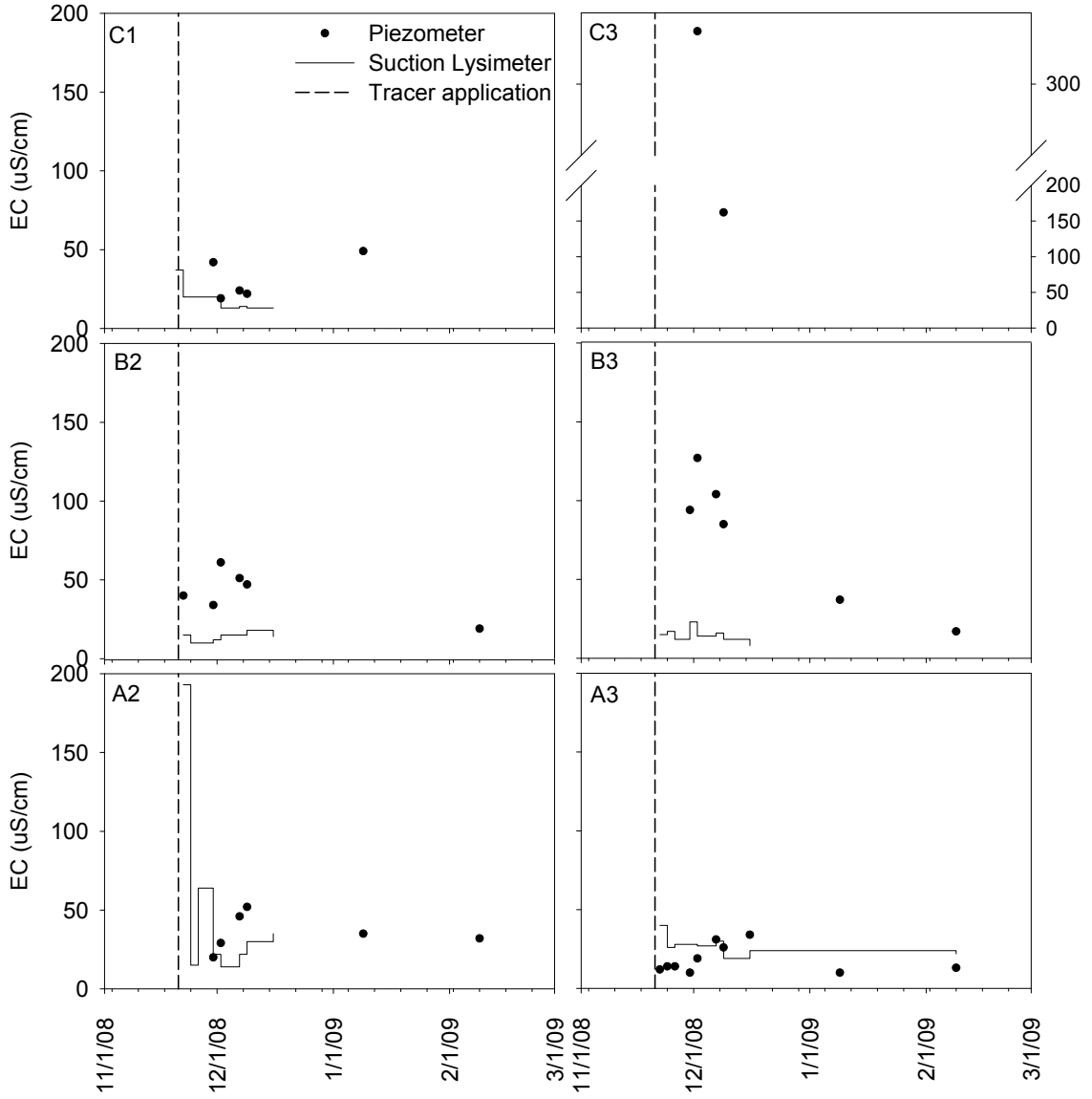

Figure A9. **Analysis for the tracer movement on the hillslope from 11/22/08 to 12/02/08. Gray squares represent EC in the piezometers (µS/cm). Open circles represent EC in the suction lysimeters the size of the symbol is proportional to the measured electrical conductivity and bromide concentration. Numbers to the lower right of each location represent the bromide concentrations (ppm) in the suction lysimeters while numbers underlined in the top left represent the bromide concentrations in the piezometers.**

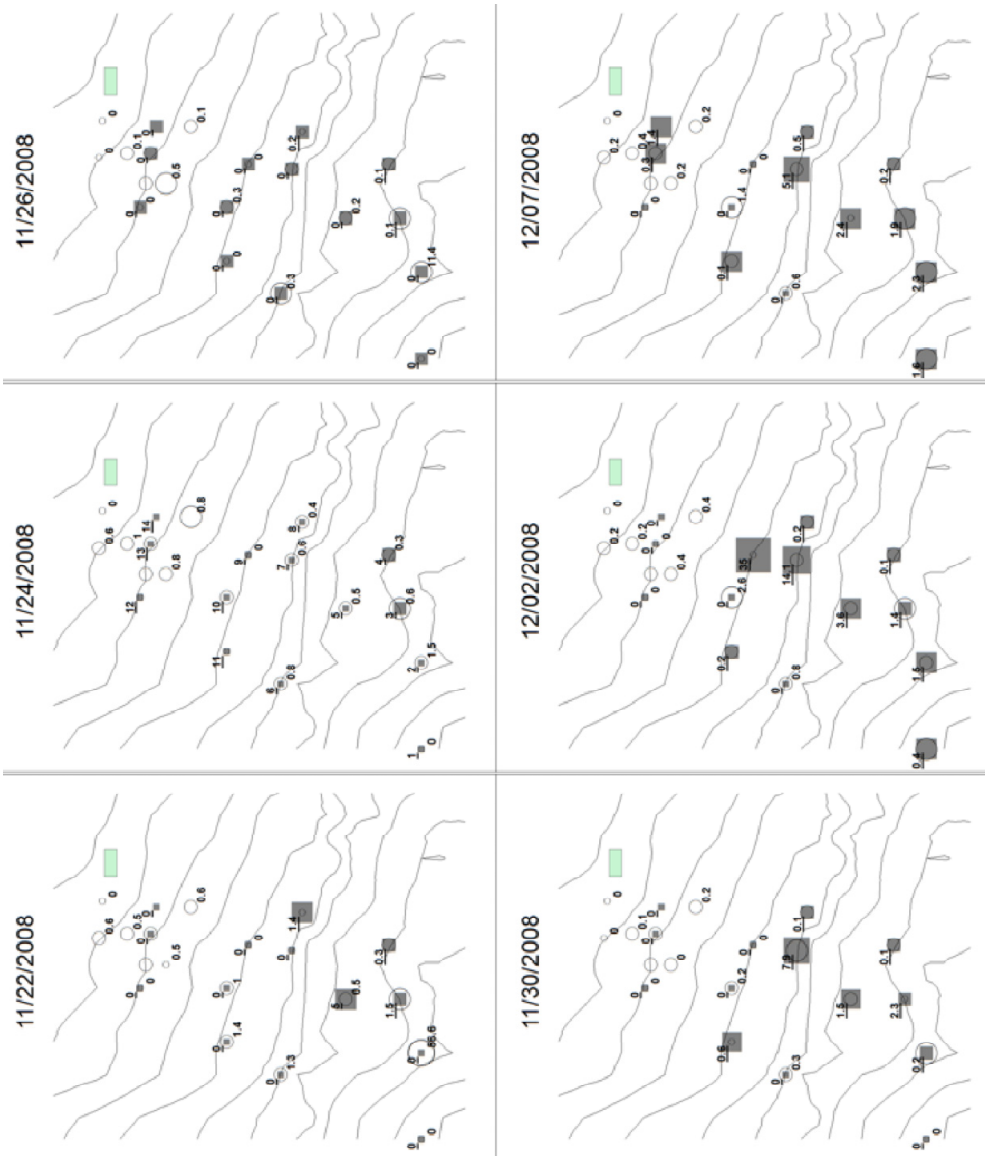

Figure A10. Analysis for the tracer movement on the hillslope from 12/07/08 to 02/09/09. Gray squares represent EC in the piezometers (µS/cm). Open circles represent EC in the suction lysimeters the size of the symbol is proportional to the measured electrical conductivity and bromide concentration. Numbers to the lower right of each location represent the bromide concentrations (ppm) in the suction lysimeters while numbers underlined in the top left represent the bromide concentrations in the piezometers.

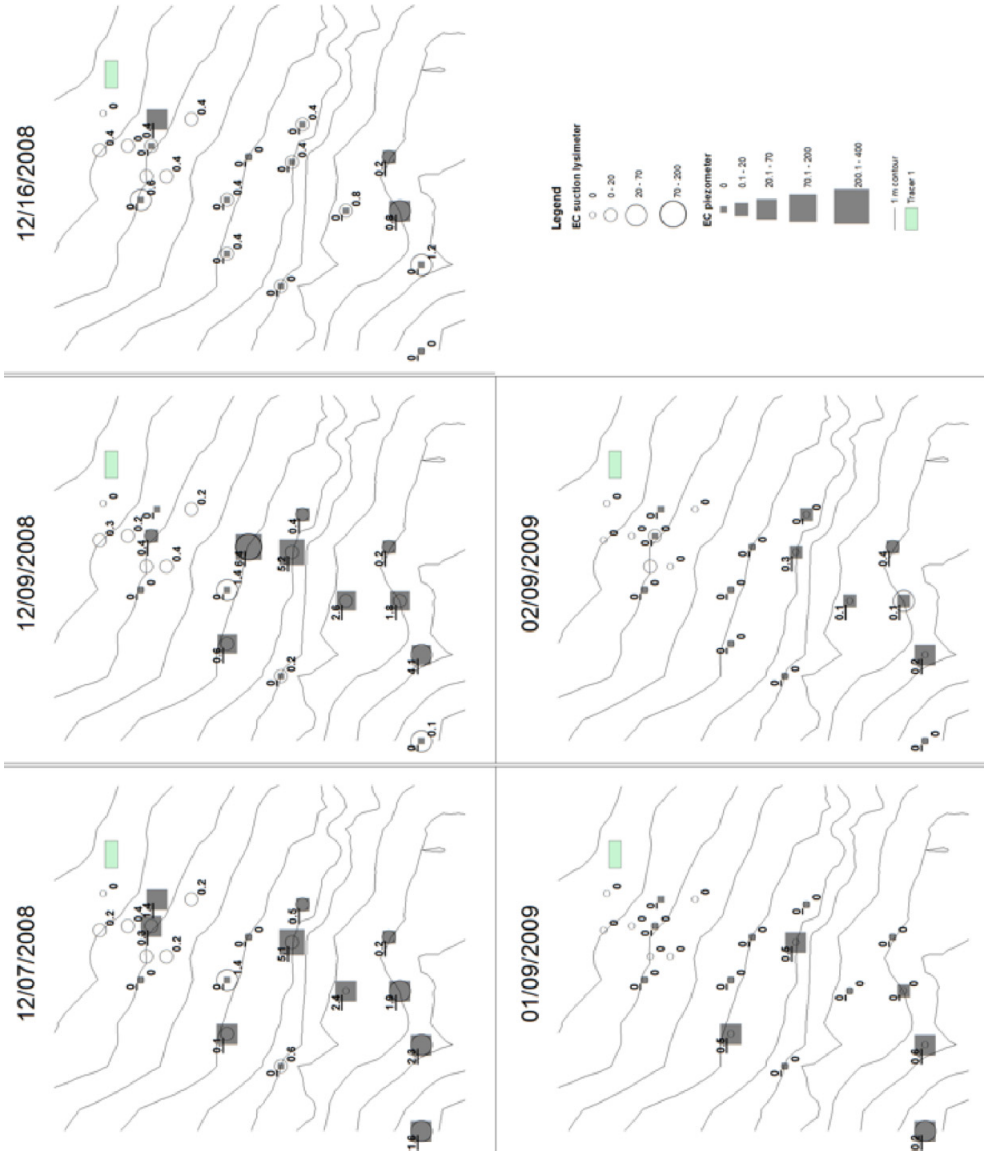

Figure A11. Relationship between time to measured peak EC (top) and Bromide concentration (bottom) as a function of distance from deployment.

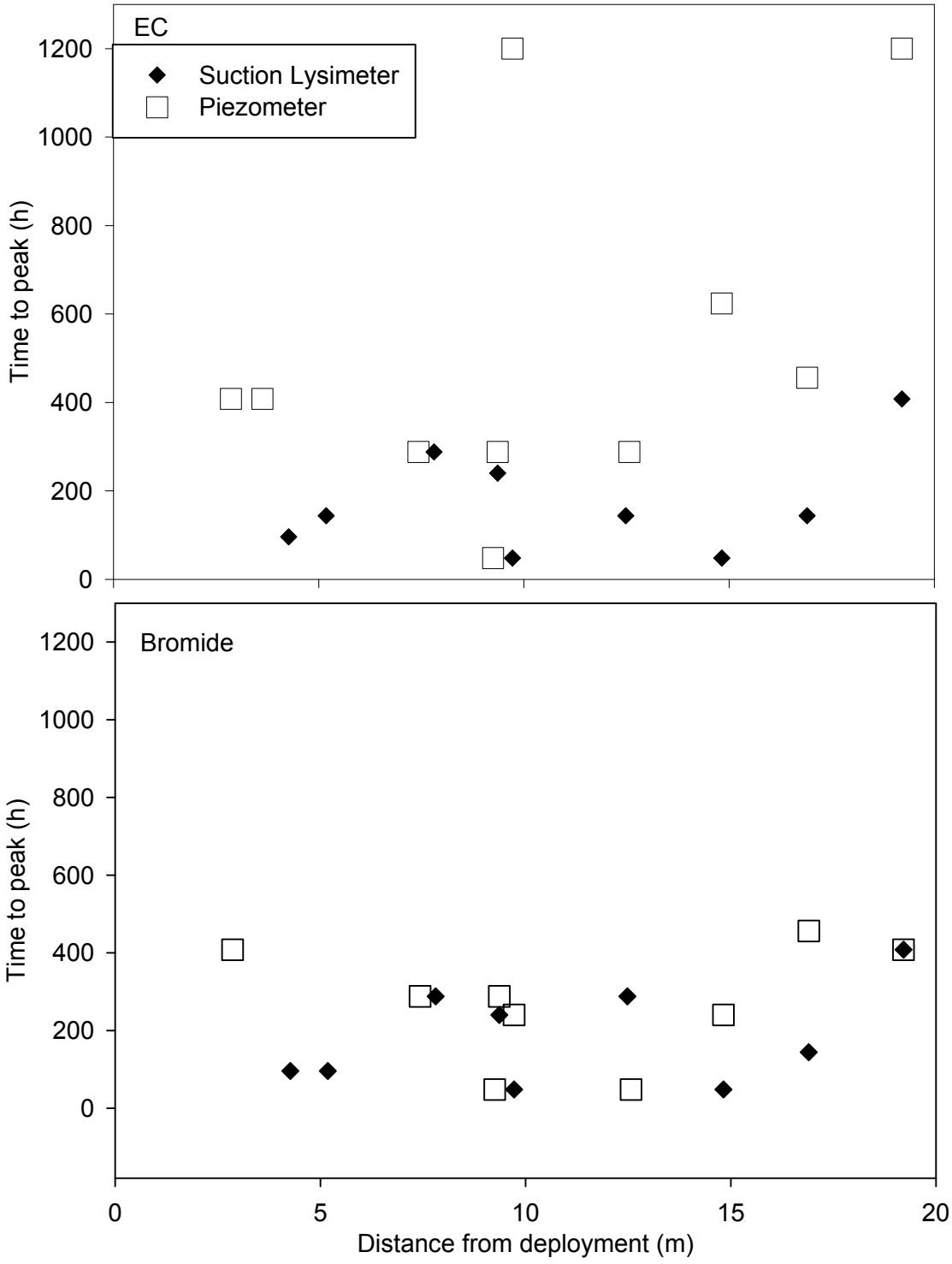

Figure A12. Peak tracer concentrations as a function of distance from tracer deployment.

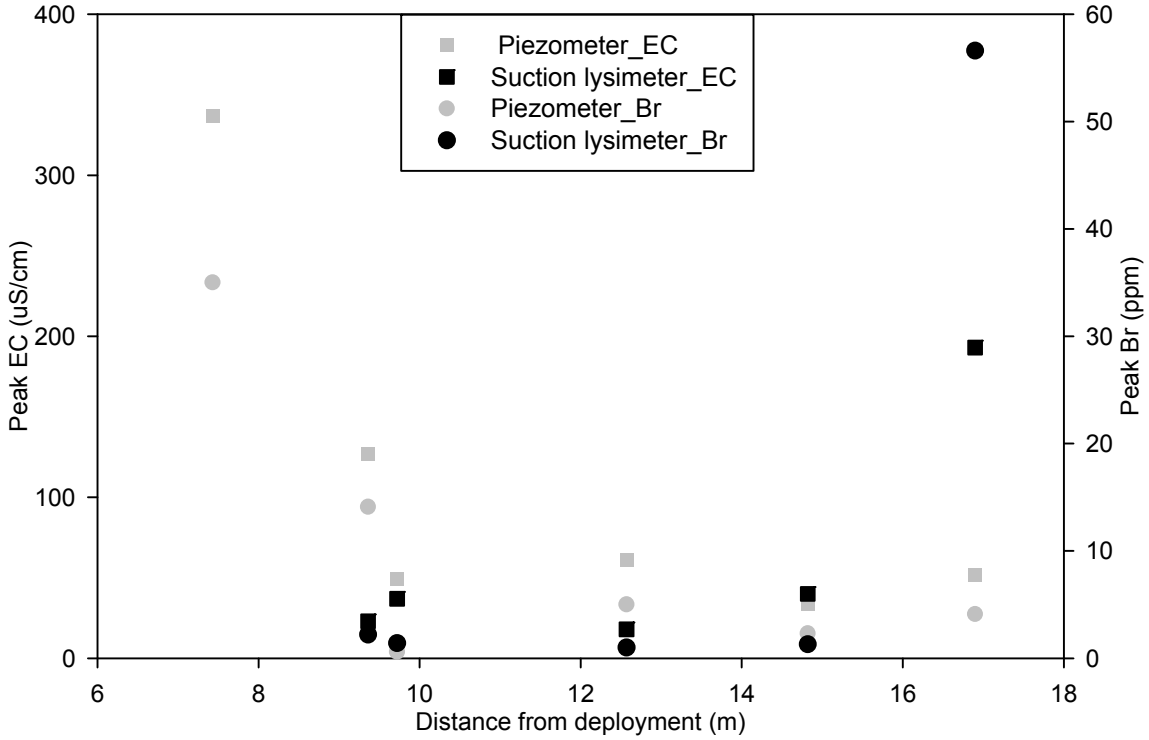

Results

This research failed to recover the tracers within the stream. Therefore the mass balance could not be determined. This led to inconclusive results.

Observations of the tracer transport through the hillslope show:

- Bromide was observed in the suction lysimeters quickly after deployment and was only observed in high concentrations in piezometers. The piezometers responded later than the suction lysimeters. Piezometers and suction lysimeters showed tracer breakthrough before 12/09/2008, suggesting that the tracer moved through the hillslope quickly (Figure A7).
- EC concentrations peaked at mid-slope locations first, and then downslope in lower concentrations. Suction lysimeter concentrations responded quickly after deployment in near stream locations, similar to

that of the bromide, suggesting that the surface tracer moved through the hillslope quickly as well.

- EC concentrations peaked quickly in suction lysimeters close to the tracer deployment (Figure A11, A12). The majority of piezometers had short times to peak. Piezometers further from deployment took longer to peak (Figure A11, bottom).
- Bromide concentrations in both piezometers and suction lysimeters showed no clear pattern in the time to measured peak concentration.
- Suction lysimeters responded in synchrony for bromide and EC and had similar relations between time to peak concentration and distance from deployment (Figure A11).
- Suction lysimeters showed higher concentrations in near-stream locations, while piezometers had higher concentrations in upslope areas. Both showed relatively lower values in mid-slope areas (Figure A12).
- Bromide concentrations could not account for the EC values showing that both tracers were present.
- Both tracers moved in two distinct spatial paths and in two different pulses. The first path appears to be A2, B3, C3, and D3, while the second path is close to C2, C1, B1, and A1. The first pulse occurred immediately after deployment and the second from 11/30 to 12/09 (Figure A9 and A10).Total precipitation during these periods was 16.7 mm and 85.6 mm, respectively.

Discussion

Implications from the results

The tracer results show that there is distinct spatial variation in lateral tracer movement and thus lateral subsurface flow. Without high resolution bedrock topographic data, the correlation between the spatially distinct flow paths of the tracer and bedrock topography cannot be determined. Tracer pulses

suggest that precipitation inputs and quick infiltration control the temporal movement of the tracer.

Short time to peak concentrations in suction lysimeters and longer times for piezometers for the NaCl tracer applied on the surface soil-bedrock interface suggests that vertical percolation is quick and that the spatial distribution of tracer concentrations are controlled by lateral tracer movement. Higher concentrations sampled from suction lysimeters also suggests that the surface tracer moves quickly through the shallow soil depths until it reaches the lower hydraulic conductivities that occur in deeper soils. Higher concentrations found in suction lysimeters in elevated soil horizons in near-stream areas (the riparian zone) could be a result of the tracer moving back into higher soil horizons where elevated water tables are found (see chapter 4).

The variable time to peak concentrations for bromide may reflect the tortuous paths taken at the soil-bedrock interface because of the spatially varying bedrock microtopography. The positive trend of bromide time to peak concentrations with distance from deployment suggests that the tracer moved quickly through the hillslope to the riparian zone. The higher concentrations in the riparian zone suggest that the tracer accumulated in near-stream areas, or that there is exfiltration of water and tracer from the bedrock in these areas. The tracer pulses through the hillslope and quick response of both tracers implies that infiltration and percolation through the shallow soils has little influence on the residence time.

Lessons from this tracer study

Without a mass balance for the tracers or the micrtopography of the bedrock this research lacks the ability to determine the cause of the spatial variation of the tracer flow paths. Tracer losses to the bedrock are undetectable because the mass balance cannot be determined. This work can lend advice for future tracer tests. These include:

- Though trenches may alter the natural flow at the trench-face, trenches seem to be useful in regions with high discharge and therefore potential for dilution. Dilution may be mediated by increasing the amount of tracer applied.
- Tracer recovery and determining the mass balance is very important for understanding how fast a tracer moves through the hillslope. To accomplish this accurate discharge data and clear tracer signals above background values are necessary, neither of which were accomplished in this research. In order to obtain a good mass balance, it is pertinent that the stage discharge relationship is very good and includes measurements at high discharge.
- Snow and snow accumulation increase the difficulty of sampling and large rain on snow events dilute the tracer too much to observe tracer concentrations in the stream. Controlling inputs (i.e. sprinkler experiments) may be the best choice for experiments (at least initially).
- More bromide should be applied in order to obtain clear responses in the hillslope and in the stream.